A New Calibration Flasher for the VERITAS Telescopes

By

Étienne Bourbeau, 260430834

Department of Physics

McGill University, Montréal

December 15th 2016

A thesis submitted to McGill University
in partial fulfillment of the requirements of the degree
of Master of Science

à Papi

Acknowledgements

I would like to thank first and foremost my supervisor, Prof. David Hanna, for giving me the opportunity to work on an amazing experiment like VERITAS. I am grateful for his guidance and advices throughout this project, which have helped me clarify my line of thought in the midst of sometime confusing results, and thought me the core skills required of a good experimental physicist.

The work accomplished on the VERITAS flashers would not have been possible without the training and guidance provided by Pascal Bourseguin in the physics machine shop, and the experience of Adam Gilbert. Many thanks to Paul Mercure for his support in computer-related issues.

I would also like to thank Prof. Ken Ragan, and my colleagues Simon Archambault, Ben Zitzer, Samuel Trépanier, John Tyler, Tony Lin, Gabriel Chernitsky, Sean Griffin, Andrew McCann and Qi Feng for the stimulating discussions about Life, the Universe, and Everything. Special thanks goes to Sujeewa Kumaratunga for her thoughtful career advices, and to my friends who often agree to follow my "ham-like" plans.

Finally, I would like to thank my mother, my father and my sister for their support and their love. Merci!

Abstract

The current generation of Imaging Atmospheric Cherenkov Telescopes (IACTs) rely on photomultiplier tubes (PMTs) to record the Cherenkov light pulses produced by the particle showers initiated by gamma rays in the upper atmosphere. Photomultiplier tubes are detectors which convert very-low-light pulses into signal electrons. The number of electrons produced per photon detected is called the gain of the PMT, and constitutes a cornerstone element of the IACT imaging technique. An accurate and frequent monitoring of the gain of every telescope pixel is essential to limit the systematic errors made when calculating the energy of a gamma ray. On the Very Energetic Radiation Imaging Telescope Array System (VERITAS), this is done by sending light pulses of linearly increasing intensities at the camera, using a Light-emitting-diode (LED)-based flasher system. This thesis describes work made on a new flasher designed to replace the current instrument. This new flasher, equipped with twice the number of LEDs as the previous one, was tested extensively in a laboratory set-up, and on the four telescopes of VERITAS. The result of this characterization show that the new instrument produces light pulses that have the same temporal shape as the original flasher; it also adds more data points to the gain-measurement plots, and slightly increases the PMT response range it is possible to probe during calibration.

This thesis also describes several attempts that were made to implement an independent light monitor inside the new flashers. The use of a PMT and a silicon photomultiplier (SiPM) as potential light monitors was assessed in the laboratory. Several technical obstacles to the implementation of this monitor have been identified, and recommendations have been made to guide any future work on this topic.

Résumé

L'actuelle génération de télescopes à imagerie atmosphérique Cherenkov (TIAC) a recours à la technologie des tubes photomultiplicateurs (TPM) pour enregistrer les impulsions lumineuses produites par le rayonnement Cherenkov accompagnant les cascades électromagnétiques générées lorsque des rayons gamma interagissent avec l'atmosphère terrestre. Un tube photomultiplicateur est un détecteur capable de convertir de très faibles impulsions lumineuses en un signal électronique amplifié; ce genre de photodétecteur est caractérisé par un gain, correspondant au nombre d'électrons produits par photon détecté. L'évaluation et l'ajustement du gain d'un TPM est une variable essentielle à la technique d'imagerie utilisée par les TIAC. Sur le Very Energetic Radiation Imaging Telescope Array System (VERITAS), le gain des TPM est calibré à l'aide d'une lampe à diodes électroluminescentes (DEL) installée sur chacun des télescopes de l'observatoire. Les travaux présentés dans ce mémoire concernent le développement et la caractérisation d'une nouvelle lampe à DEL sensée remplacer l'équipement existant. Les résultats obtenus, lors de tests en laboratoire et d'essais de terrain sur les télescopes, démontrent que le nouvel outil de calibration est en mesure de produire des impulsions lumineuses similaires à celles produites par l'ancienne lampe. De plus, l'ajout de 8 DEL supplémentaires au nouvel instrument permettra de mesurer le gain des TPMs avec une meilleure précision, et d'accroître la plage dynamique de réponse des TPM qu'il est possible de caractériser.

Finalement, une portion significative de ce mémoire rapporte le résultat de tests effectués pour inclure, à l'intérieur de la nouvelle lampe de calibration, un photodétecteur capable de mesurer de manière indépendante l'intensité des impulsions lumineuses envoyées vers la caméra de chaque télescope. Deux types de photodétecteurs, un TPM et un circuit photomultiplicateur sur silicium (CPMSi), ont été considérés comme de potentiels moniteurs d'intensité lumineuse. Les résultats de ces tests ont permis d'identifier plusieurs obstacles à l'élaboration d'un tel moniteur, de même que des pistes de solutions pour de futurs travaux de développement sur ce dispositif.

Contents

List of Figures

1 Introduction

This thesis describes the design and performances of new LED-based calibration flashers which have been installed on the Very Energetic Radiation Imaging Telescope Array System (VERITAS). The flashers send pulses of light to the cameras of the telescopes in order to measure and calibrate the gain of the photomultiplier tubes that are used inside the cameras' pixels. The objective of these new flashers is to add experimental data points covering both amplifier modes of the cameras, and increase the range of light intensities available by doubling the number of LEDs installed on the devices; this will allow the instruments to probe deeper into the response range of the PMTs when the latters are switched into a special, low-gain mode, which will be described in this work. In addition to the development of more powerful flashers, the work presented in this thesis presents results from the testing of a light monitor concept, which would allow for an independent tracking of the brightness of the pulses sent by a flasher.

1.1 Thesis Layout

Chapter 2 gives an overview of the field of Very-High-Energy (VHE) gamma-ray astronomy, in the context of imaging atmospheric telescopes like VERITAS. A description of the imaging technique used in this type of experiment is presented, along with an overview of the science topics most investigated by this branch of astrophysics.

Chapter 3 focuses on the VERITAS camera hardware, and the calibration techniques that have been developped to monitor the performance of the instrument. The concepts of relative and absolute gains are explained, and a description of the current flasher hardware is given.

Chapter 4 details the schematics of the new, 15-LED flasher, which was built and tested over the course of this master's project. The working principles of Flash Analog-to-Digital Converters (FADCs) are presented in this section, and placed in the context of the analysis code developed to assess the performances of the new flashers.

Chapter 5 presents the results of the laboratory and on-site tests performed, to ensure that the light pulses produced by the new flasher would closely resemble that of the current-generation instruments.

Finally, Chapter 6 describes the concept of the on-board light monitor, and presents the results of the laboratory characterization of two types of light sensors envisioned to serve that purpose: the R3998-02 Hamatsu PMT and the Array-SB4 SensL silicon photomultiplier.

2 VHE Astrophysics in the context of VERITAS

2.1 Astro-particle physics: an historical perspective

Compared to the centuries-old discipline of conventional astronomy, the observational detection and characterization of astrophysical high-energy particles is a relatively new endeavour. The first investigation of such particles began in the 1910's, when several experiments revealed that the ionization rates of atmospheric particles increased with altitude[1]. [1] These results hinted for the first time at the existence of *cosmic rays*, an extra-terrestrial source of energy which could, like ground-level radioactive materials, ionize matter. Initially motivated by investigations on the source of these rays, the field eventually grew to include various types of high-energy particles (gamma rays and neutrinos) and evolved into a more comprehensive, multi-messenger study of the many explosive and energetic processes occuring in our universe.

Gamma rays in particular were from the start a promising avenue to understand these phenomena. Given their charge neutrality, gamma-ray photons can travel great distances without being perturbed by the various magnetic fields present in space, allowing us to trace back the location of their astrophysical source in the sky. With the advent of space satellites, the first discovery of gamma-ray emission from the galactic plane was made by OSO-III [2] in 1967, while the COS-B satellite [3] became in 1972 the first mission to map the gamma-ray sources in our universe. Following the pioneering work of these probes, the launch of the Compton Gamma-ray Observatory (1991-2000) [4], equipped with four instruments dedicated to specific types of gamma-ray emission studies, significantly increased the number of identified high-energy sources. The latest of these space-based experiments, the Fermi Gamma-ray Space Telescope [5] [6] launched in 2008, has done a tremendous job of cataloging over 3000 point sources in the sky [7].

In parallel to space-based observatories, efforts were made to develop ground telescopes capable of detecting very-high-energy (VHE, describing energies between 100 GeV and 10

[1] Namely, Theodore Wulf (1910) measured the ionization rate on top of the Eiffel tower, while Victor Hess did the same at higher altitude, using a hot-air balloon to move himself.

TeV) gamma rays: photons that are so energetic that they are able to leave, at ground-level, a trace of their interaction with the upper atmosphere. After several years of hardware upgrades and improvement of the analysis technique, the Whipple 10m telescope [8] finally became, in 1989, the first ground-based telescope capable of detecting the Crab Nebula in the VHE domain [9]. Nowadays, the Earth is home to four major gamma-ray observatories, together covering the 30 GeV-100 TeV energy range of the electromagnetic spectrum: Three imaging atmospheric Cherenkov telescopes, or IACTs (HESS [10], MAGIC [11] and VERITAS [12]), which use the imaging technique described in the next section, and one array of water-Cherenkov detectors, the HAWC [13] experiment.

2.2 The Imaging Atmospheric Cherenkov Technique

2.2.1 The physics of atmospheric showers

When gamma rays penetrate the atmosphere, they inevitably end up interacting with the surrounding medium and, given the very high energy of the photons involved, that interaction will be exclusively governed by the process of electron-positron (e^+e^-) pair creation. The particle products of this initial interaction will release part of their kinetic energy in the form of secondary gamma rays, via bremsstrahlung radiation, and those secondary gamma rays will themselves produce e^+e^- pairs. Rapidly, an electromagnetic shower of highly relativistic electrons and positrons will form, traveling several kilometers through the atmosphere at a speed surpassing the speed of light in the medium (in this case, air). The number of particles within the shower will grow exponentially, up to the point where the energy of individual particles will drop below the pair-production threshold (1.022 MeV).

Particle showers also form when cosmic rays interact with atoms of the upper atmosphere. However, because of their hadronic nature[2], the physical interactions involved in the shower process differ from that of gamma rays: rather than producing e^+e^- pairs, proton-proton

[2]cosmic rays consist mostly of charged protons (90%) and, to a lesser extent, helium (9%) and other heavier nuclei.

and proton-neutron collisions between cosmic rays and atmospheric nuclei yield an approximately equal mixture of charged and neutral pions: π^+, π^- and π^0. These pions subsequently decay into different products: neutral pions produce gamma rays (which will then initiate a secondary e^+e^- shower), while charged pions decay into muons. Due to strong interaction effects, the secondary products of the particle shower have a larger transverse momentum than in the case of gamma-initiated showers; this reflects on ground level by a more lateraly dispersed shower trace (see figure 2.1).

Those differences between hadron and gamma-ray shower morphologies will have direct repercussions on their images in IACTs, which will be useful later to improve the signal-to-noise ratio of the data recorded.

2.2.2 Cherenkov Radiation

To the delight of gamma-ray astrophysicists, particle showers in the atmosphere are always accompanied by a light emission process called Cherenkov radiation. First observed by Pavel Cherenkov in 1934, and later explained by Ilya Frank and Igor Tamm in 1937, this radiation process occurs as charged particles polarize the surrounding medium faster than it can relax: As the electromagnetic disturbance moves through the dielectric, a preferential direction of polarization will form, which will result in the creation of a coherent "photonic shockwave" that will travel at a specific angle, named the *Cherenkov angle*, given by equation 1. That angle depends on the particle's speed v_p, which is in this case greater than the speed of light in the medium, c/n, and on the the refractive index of the atmosphere n, which varies as a function of altitude.

$$cos(\theta_C) = \frac{c}{nv_p} \tag{1}$$

Like any radiation process, Cherenkov light is emitted at various wavelengths according to a particular spectrum, which can be derived by considering the electromagnetic power emitted by a charged particle traveling uniformly through a medium at a speed $v_p = \beta c$. [15]. A starting point to determine the shape of this spectrum is Maxwell's fundamental equations of

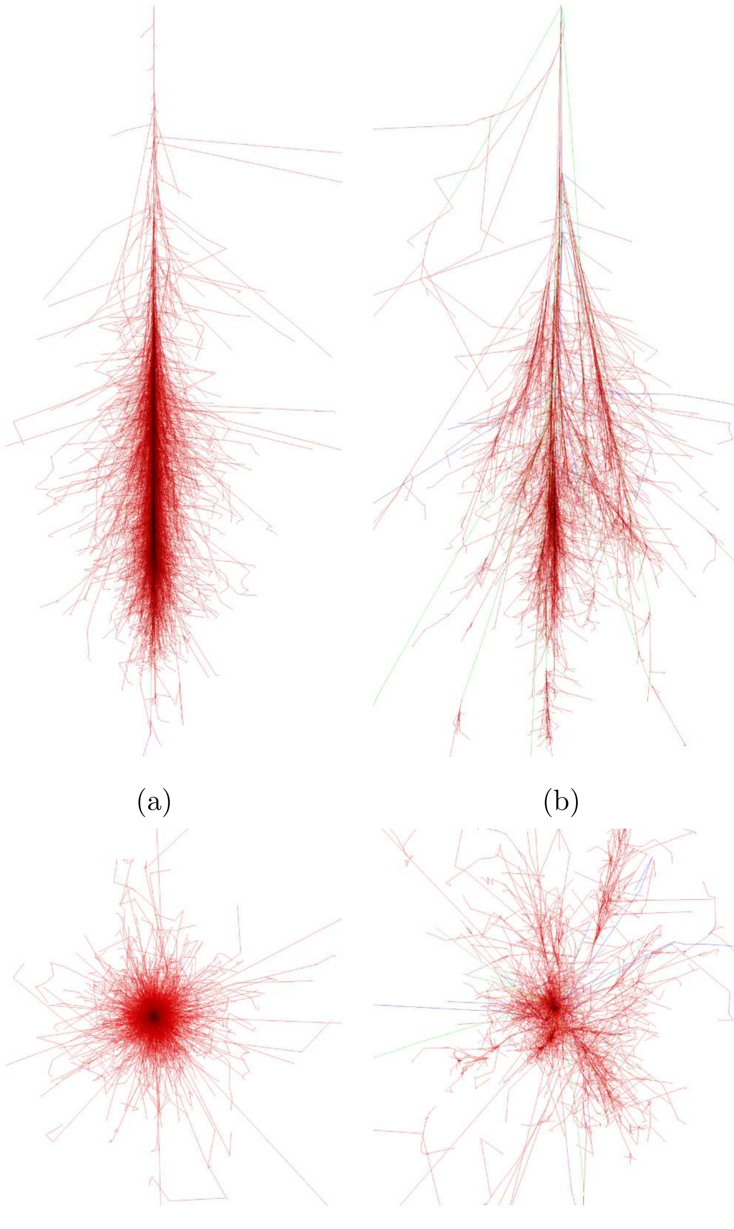

(a) (b)

(c) (d)

Figure 2.1: Result of a Monte Carlo simulation of a 100 GeV gamma-ray-initiated (a,c), and a 100 GeV proton-initiated (b,d) particle shower, showing the morphology of their development in the atmosphere. The top plots show the side view of the showers, while the bottom plots show the view along the shower axis. Particles within hadronic showers (whose track in the sky is coloured in red) are less concentrated around the shower axis, producing a more dispersed pattern on the ground than in the case of gamma-ray showers. Source: [14]

electromagnetism in the Fourier domain, expressed in terms of the magnetic vector potential $\vec{A_\omega}$ and electric scalar potential ϕ_ω.

$$\vec{H_\omega} = \vec{\nabla} \times \vec{A_\omega} \tag{2}$$

$$\vec{E_\omega} = -\vec{\nabla}\phi - i\omega\vec{A_\omega} \tag{3}$$

$$\nabla^2\vec{A_\omega} + \frac{\omega^2 n^2}{c^2}\phi_\omega = -\mu\vec{j_\omega} \tag{4}$$

$$\vec{\nabla} \cdot \vec{A_\omega} + \frac{i\omega n^2}{c^2}\phi_\omega = 0 \tag{5}$$

In this representation, we obtain definitions of $\vec{E_\omega}$ and $\vec{H_\omega}$ that may be solely dependent on the vector potential $\vec{A_\omega}$, provided we use a convenient gauge like eq.5[3]. Using equation 4, and provided with a reasonably simple definition of the free current density j_ω [4] , one can find the functional shape of both $\vec{E_\omega}$ and $\vec{H_\omega}$; this allows us to derive the electromagnetic power emitted by the particle, which is given by the time-averaged value of the particle's Poynting vector $\vec{S} = \vec{E} \times \vec{H}$. Expressed in the Fourier domain, this relation yields, after many simplification steps:

$$E = \frac{q^2}{c^2}\int_0^l dx \int \omega(1 - \frac{1}{\beta^2 n^2})d\omega \tag{6}$$

In its differential form, the above equation becomes an expression for the energy emitted per unit length, per unit wavelength, by the Cherenkov process:

$$\frac{dE}{d\omega dx} = \frac{q^2}{c^2}\omega(1 - \frac{1}{\beta^2 n(\omega)^2}) \tag{7}$$

This formula is known as the Frank-Tamm formula, and it shows that the intensity of the Cherenkov light is an increasing function of frequency ω: more light is produced at shorter

[3] $\vec{A_\omega}$ is a mathematical construct that can take many forms, provided that the divergence of its curl is equal to zero. A *gauge* refers to an equation that provides a definition of such form; eq.5 is an example of a gauge.

[4] One can describe the Cherenkov current density as a point-like electric charge moving at velocity v_p in the z-direction: $j_z = q \cdot v_p\delta(x)\delta(y)\delta(z - v_p t)$.

wavelengths, up to a certain point where the dispersive nature of the refractive index, $n(\omega)$, will prevent higher energy photons from traveling slower than the particle.

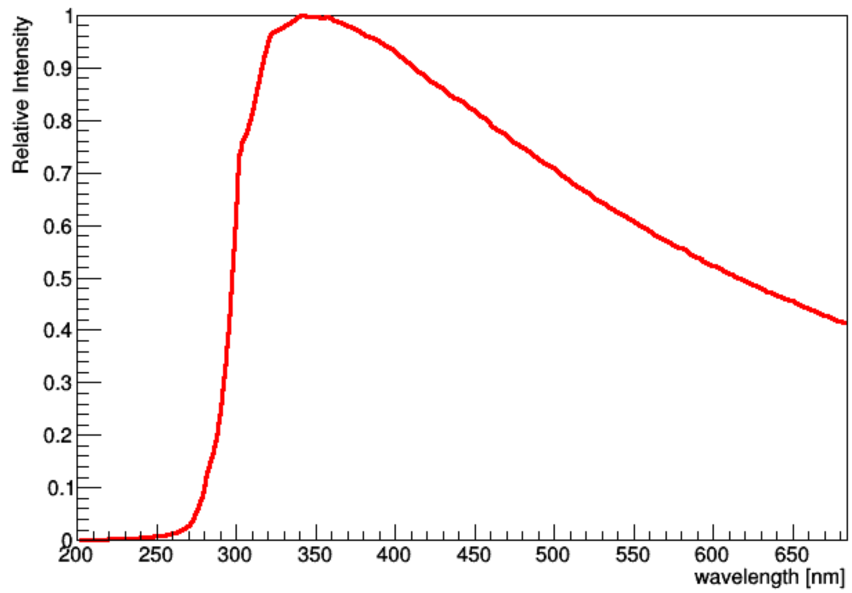

Figure 2.2: Example of the realistic Cherenkov spectrum of a 500 GeV gamma-ray shower as seen at ground level. While it is an increasing function of energy, the intensity of the Cherenkov light will also be affected by changes in the refractive index as a function of altitude and atmospheric absorption, leading to a peak of emission in the UV/blue portion of the EM spectrum. Source: [16]

Taken in the context of atmospheric particle showers, the Cherenkov light spectrum will also be affected by changes in the refractive index as a function of altitude, and atmospheric absorption. The resulting spectrum, calculated by Monte Carlo simulations and plotted in figure 2.2, will peak in the blue/UV range of energies, a characteristic that motivates the choice of UV LEDs in the calibration instrument described in section 3.4.

At ground level, the detectable signal of Cherenkov radiation will be a light pulse lasting approximately 10 ns. That pulse will be detectable inside the "Cherenkov pool", the area on the ground that receives Cherenkov emission from the shower; typical light pools are usually 200-300 metres in diameter, and will form ring-like structures as shown in figure 2.4a. If

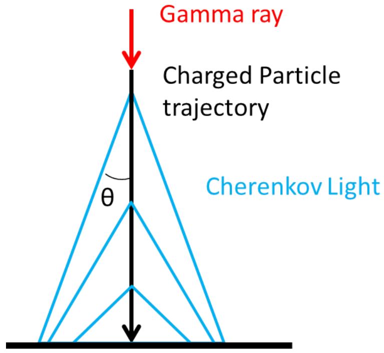

(a)

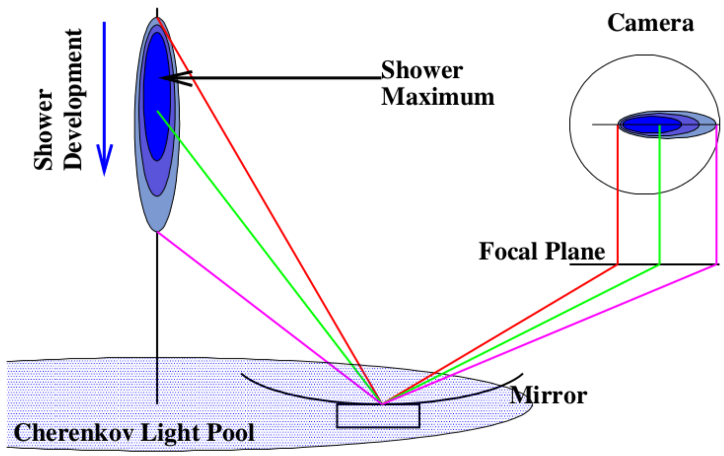

(b)

Figure 2.3: a) As a charged particle moves toward the ground, the refractive index of the air will increase, leading to a larger Cherenkov angle at low altitude. This will produce a ring-pattern of light on the ground. b) The ring-structured light pool from a charged particle can be collected by telescopes on the ground: the incoming light is reflected by mirrors onto a camera installed at the focal plane, which will create an elliptical-shaped image. The length of this image will reflect the longitudinal development of the shower, while the width of the image will mirror its lateral development. Source: [14]

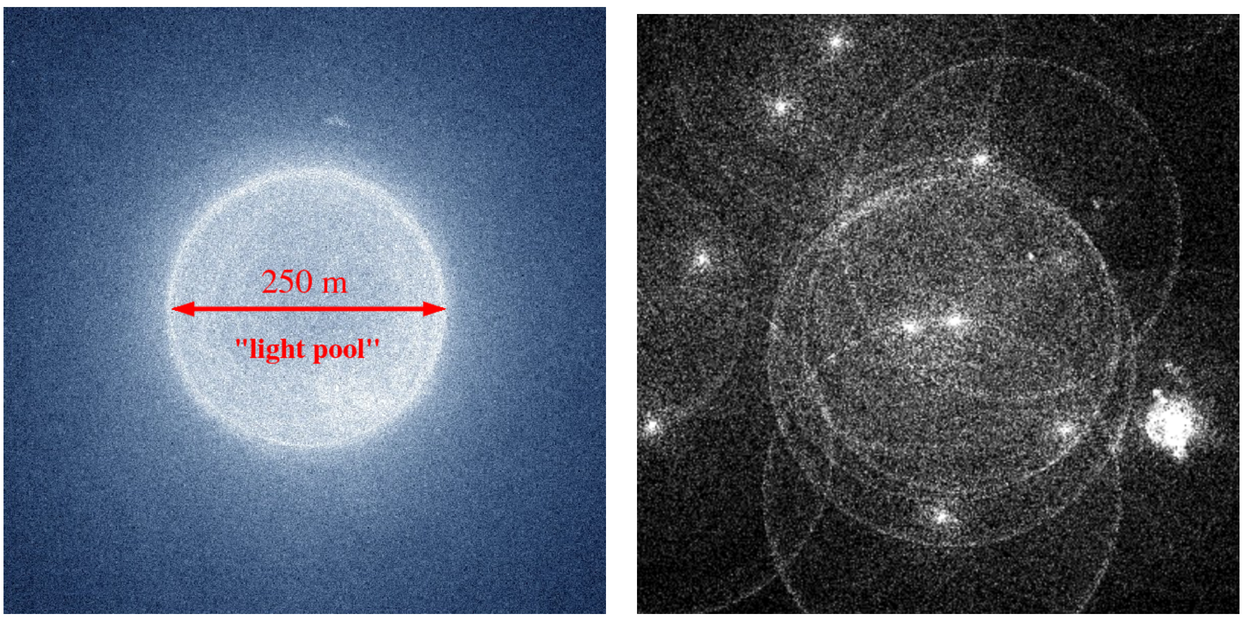

(a)

(b)

Figure 2.4: Simulation of the ground distribution of Cherenkov photons generated by a 100 GeV gamma ray (a), and a 300 GeV proton (b) shower. The superposition of Cherenkov rings (such as the ones illustrated in figure 2.3a) from all particles within a gamma-ray shower will generate a light pool similar to the one simulated in 2.4a. On the other hand, the more chaotic tracks left by the hadronic showers on the ground (figure 2.1d) will produce a Cherenkov light pool that will be disorganized. Simulation images retrieved from [16] and [17].

an array of telescopes is positioned within the Cherenkov light pool, allowing for a stereoscopic observation of the shower's morphology, it is possible to reconstruct the height H and lateral distance l of the shower core, and thus estimate the energy of the gamma ray that first initiated the shower. These are the principles behind Imaging Atmospheric Cherenkov Telescopes (IACTs), of which VERITAS is an example of.

2.2.3 The VERITAS Experiment

Located in southern Arizona, the Very Energetic Radiation Imaging Telescope Array System (VERITAS) is an ensemble of four Davies-Cotton telescopes, each 12 metres in diameter [12]. Each instrument is a complex assembly of several subsystems, which can for the most part be associated with one of three locations in the telescope's vicinity: the reflector, the camera box, and the data acquisition trailer. Figure 2.5 illustrates the current state of the array, while figure 2.6 identifies the three sections on one of the telescopes.

Figure 2.5: The VERITAS Experiment, in its current configuration (2016). Photo courtesy of L. Ciuik, Adler Planetarium.

The long path toward detection of a gamma-ray photon begins when Cherenkov light from its associated particle shower is reflected by the 355 identical mirror segments that are fixed on the optical support structure (OSS). The light will then be directed onto the camera plane, where a hexagonal array of 499 *photomultiplier tubes* (PMTs, also referred to as pixels) will convert it into an amplified electric signal. The pulse signal from every PMT channel will be conveyed via a coaxial cable to the data acquisition trailer, where it will once again be amplified before being digitized by a 500 Msps (million samples per second), *flash analog-to-digital converter* (FADC), which are described in more details in section 4.5.1. Overall, the data acquisition system of VERITAS allows the array to record Cherenkov shower events at an approximate rate of 300 Hz, with a minimal deadtime fraction of approximately 9%.

When describing the performance of a telescope, several criteria are often quoted as a measure of how a given experiment is effective at observing the sky:

The *field-of-view (FOV)* of a telescope is an indication of how large a portion of the sky it is able to observe at any moment. In the case of VERITAS, which is a set of pointing instruments, the field of view is relatively small (3.5 degrees) compared to all-sky experiments such as HAWC, or Fermi-LAT. This renders the array more suited for the observation of point sources or small-scale structures, as opposed to very extended or diffuse emission regions; it also means that an IACT like VERITAS is unlikely to detect transient events.

The *effective (or light collection) area* can be thought of as the spatial scale of the experiment: it indicates the extent of the surface upon which gamma-ray photons will produce a detectable Cherenkov signal on the ground [16] [14]. In the case of VERITAS, this parameter reaches a peak 100 000 m^2, which is gigantic in comparison to Fermi-LAT (1 m^2) [5], the largest gamma-ray space telescope currently in operation.

The *angular resolution* of a telescope defines a minimal spatial extent below which a source cannot be resolved and is considered "point-like". Unlike other types of telescopes, the angular resolution of an IACT is not limited by diffraction or atmospheric conditions, but by fluctuations in the shower geometry. Using its current data analysis tools, VERITAS can locate the origin of a single photon within a 68% containement radius of less than $0.1°$ above 1 TeV. This precision is better than the angular resolution of the Fermi-LAT instrument ($0.15°$ above 10 GeV), but is no match for X-ray telescopes such as Chandra [18] (0.5

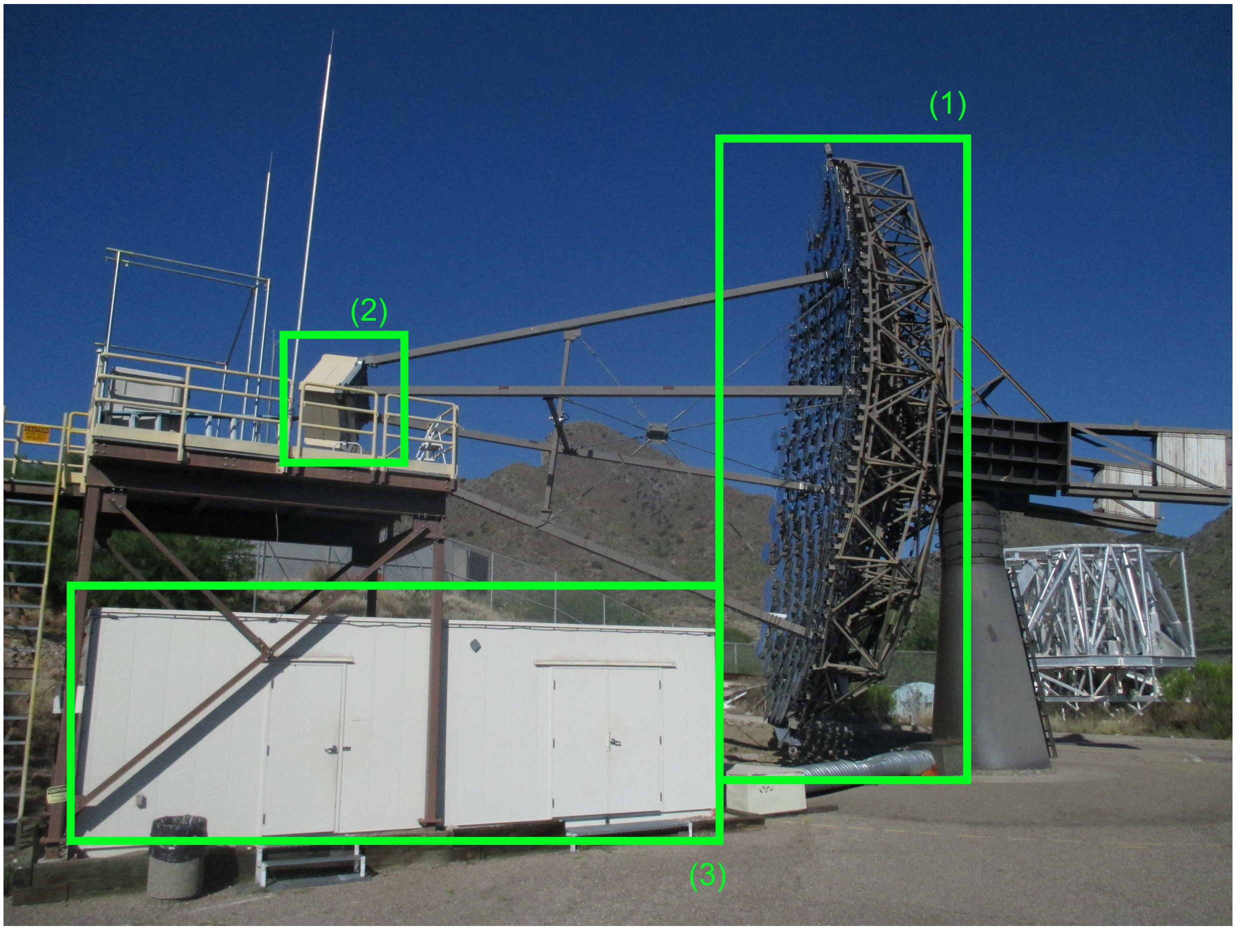

Figure 2.6: The main parts of a VERITAS atmospheric Cherenkov telescope. The primary reflector (1) comprises 355 identical mirror facets mounted on an optical support structure (OSS), which is itself attached to an azimuth-elevation mount. The camera box (2) is held at the reflector's focal point with quad-arms extending from the OSS. Finally, the telescope trailer (3) hosts the FADC electronics that digitize the Cherenkov pulses received by the camera's PMTs.

arcseconds half-power diameter containement, in the 0.1-10 keV range).

The *sensitivity* of a telescope describes the efficiency at which it is possible to distinguish a true light signal from background noise. A highly sensitive experiment will be able to detect very faint light sources in a very short lapse of exposure time, thus maximizing the science that can be made with every bit of raw data. The definition of sensitivity may differ from one experiment to the other; a common definition in gamma-ray astronomy is the exposure time required to statistically detect a known source of constant luminosity at the 5-sigma (99.999943%) confidence level. For VERITAS, sensitivity measurements are based on flux measurements from the Crab Nebula: a weak source emitting 1% of the Crab's nominal flux can be detected after 25 hours of observations.

All of the above performance criteria (with the exception of the FOV) vary with the energy of the gamma-ray shower, and observational variables like telescope elevation and weather. As we will see in section 2.2.5, the treatment of those performances will be segmented into a set of tables, for a wide range of energies and observing conditions.

2.2.4 Triggering off atmospheric air showers

Since the telescopes operate in the optical wavelength spectrum, many sources of noise, whether constant or transient, can be detected by cameras of the array. In order to improve the array's sensitivity to gamma-ray-initiated Cherenkov air showers, a three-level analog trigger architecture has been implemented on VERITAS, with each level contributing to isolate specific sources of spurious optical light and reducing the rate of data inflow to levels that are manageable for the electronics.

The first trigger level (L1) consists of constant fraction discriminators (CFD) that are connected to individual channels of the FADCs: it sets a voltage threshold above which a signal must be in order for a pixel to be triggered. The value of this criterion is programmable, and it has to be optimized in such a way as to maximize the detection of low-energy showers, without burdening the readout electronics with an excessive number of spurious triggers from

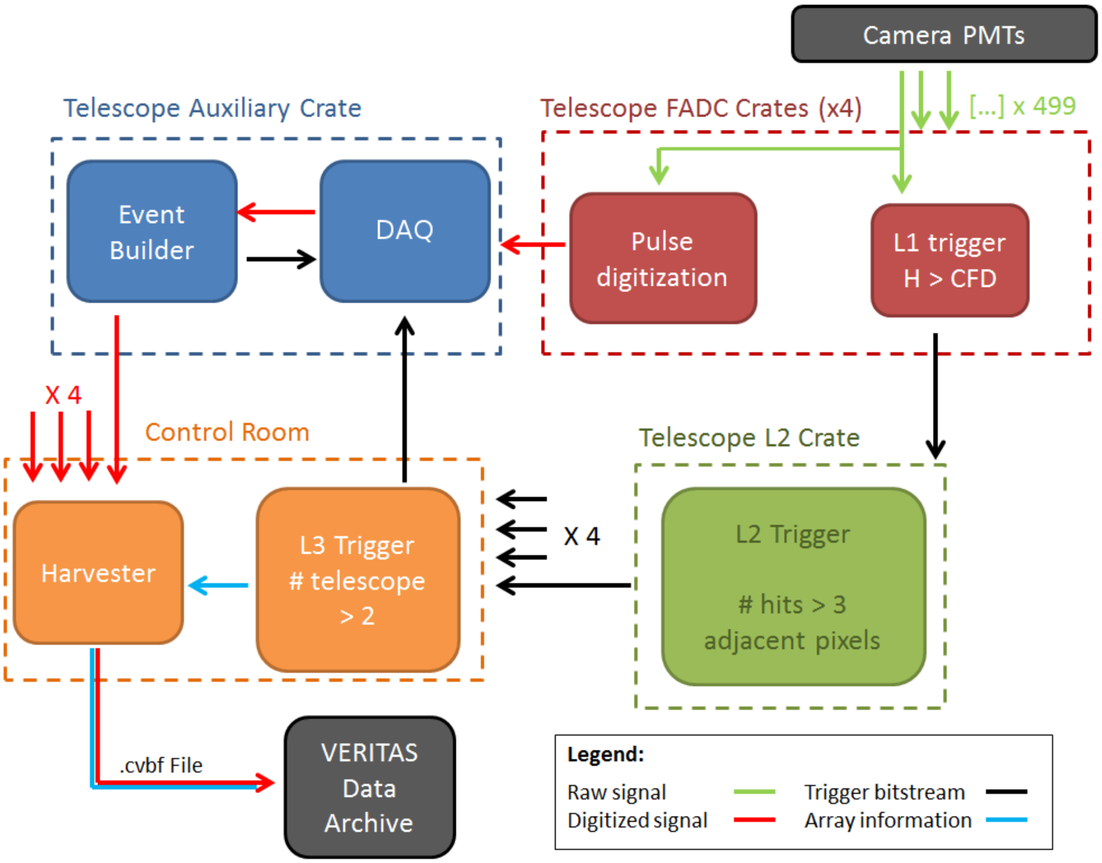

Figure 2.7: Schematics of the VERITAS Data Acquisition chain. Once an event has satisfied the three triggering conditions, the L3 server instructs each of the telescope's DAQs to retrieve from their memory the signal trace recorded for each pixel by the FADC. That information is sent to the telescope's Event Builder, which combines the data from individual channels, bundles it, and sends it back to the Harvester software. The Harvester then writes that information into the VERITAS standard data format (.cvbf), and sends it to the observatory's archive.

the night sky background (NSB) fluctuations [14].

The second level (or L2), is a field-programmable gate array (FPGA)[5]based trigger that looks for coincidence patterns between adjacent pixels. Upon reception of the L1 trigger from a pixel, an L2-signal is sent if at least 3 neigbouring pixels have triggered within a certain coincidence time window [19]. This type of pattern trigger is used to block signals from spontaneous NSB-triggered pixels.

The third and final trigger level (L3) is an array trigger which looks for coincidences between telescopes. If two or more telescopes have triggered their L2 circuit, then the L3 will initiate the process that will result in data acquisition. The necessity of a multiple-telescope trigger emerges from the need to eliminate atmospheric muon signals from the data stream: muons produced by cosmic-ray showers travel deeper in the atmosphere than other particles, and will also emit Cherenkov radiation, albeit circumscribed within a smaller area on the ground. Because of this, muon signals are often only visible in one telescope of the array, allowing for the supression of that source of noise from the regular data stream.[6]

2.2.5 Data acquisition and offline analysis

Once a particular occurence of an air-shower has successfully passed all three levels of the trigger system, it becomes known as an *event* that occured during a particular *run* of observation. A run is a standardized period of time, usually 30 minutes, during which every event triggering the telescopes is saved into a single data file. The major steps of the data processing chain, which is responsible for writing events to the raw data files, are illustrated in figure 2.7. It begins with the dispatch of a command from the L3 server to each of the telescope's Data AcQuisition server (DAQ). This command instructs the DAQs to retrieve from their memory the signal trace recorded for each pixel by the FADC, starting at a par-

[5]FPGAs are multipurpose, user-programmable processing units arranged in logic blocks, which can be used to perform various real-time arithmetic or logic operations.

[6]Note that due to the distinctive Cherenkov light ring patterns they leave on a telescope's camera, muons can constitute a free calibration tool to level the absolute gain of the telescope array. See section 3.5.3.

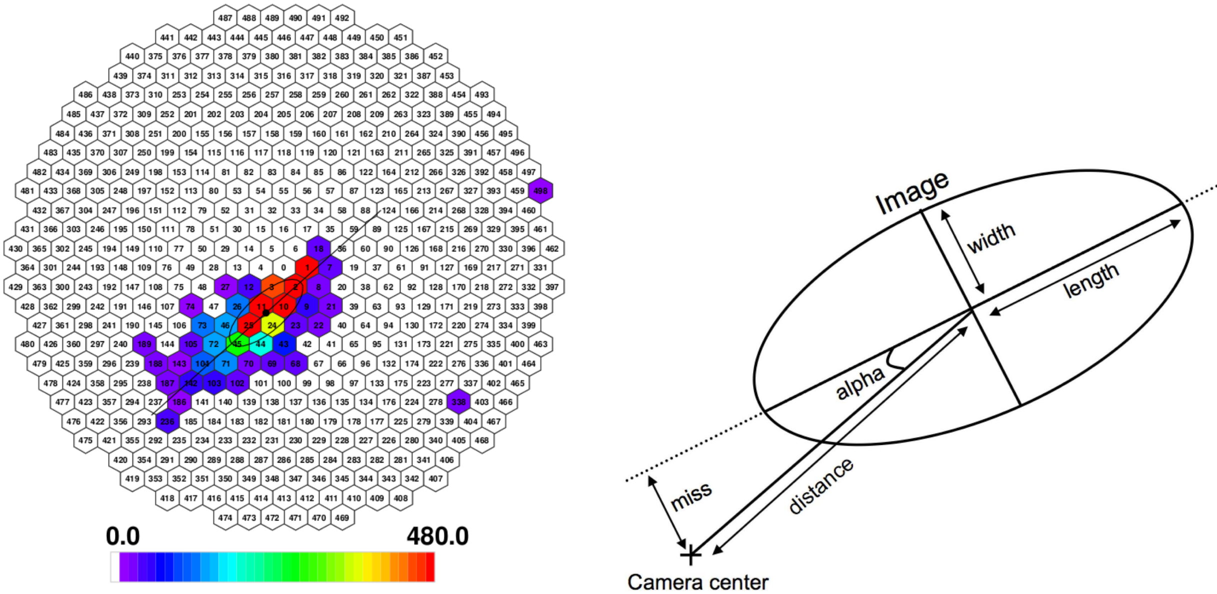

(a) (b)

Figure 2.8: a) Typical image recorded during a shower event, cleaned from NSB noise (Source: [20]). b) By extracting a set of five basic parameters out of image (a), it is possible to reconstruct the origin and energy of the shower at the origin of this event. These parameters are named the Hillas parameters, and are labelled in this image (taken from [21]).

ticular *look-back time* and lasting for a time window of 32ns onward. Once the DAQ finds the relevant traces, it sends that information to the telescope's *Event Builder*. This program then combines the data from individual channels, and bundles them into a single-telescope event which will then be sent back to the control room server, and handled by the *Harvester* software. Upon reception of data from all four telescopes of the array, the Harvester combines everything into a single event file, including in the process information about the array configuration and triggering time to the data stream. This final event is written to the current run file in a customized binary format, the compressed VERITAS databank format (.cvbf). Upon termination of a run, the Harvester sends the completed data file to the VERITAS archive, where it becomes available for analysis.

Following observations made by an IACT, how does one proceed to extract meaningful information from the raw data obtained from the camera? To begin with, the first and crucial piece of information extracted from the data is the *integrated charge* of the electronic *trace* (figure 2.9) recorded by each PMT during an event. This parameter is obtained by summing the voltage readings of a given FADC channel over the duration of the Cherenkov pulse, and subtracting from the signal a DC, *pedestal signal* which is a DC offset incorporating night-sky-background (NSB) fluctuations about it. The integrated charge, which constitutes a measure of a shower's brightness in IACTs, will serve as a proxy measurement for the energy of a gamma ray, and as such must be measured as accurately as possible to avoid systematic errors that will propagate through the rest of the analysis. Chapter 3 offers a more thorough discussion about the methods employed to correctly estimate the integrated charge on the VERITAS cameras, and the calibration tools deployed on the telescopes to maintain the accuracy on this measurement.

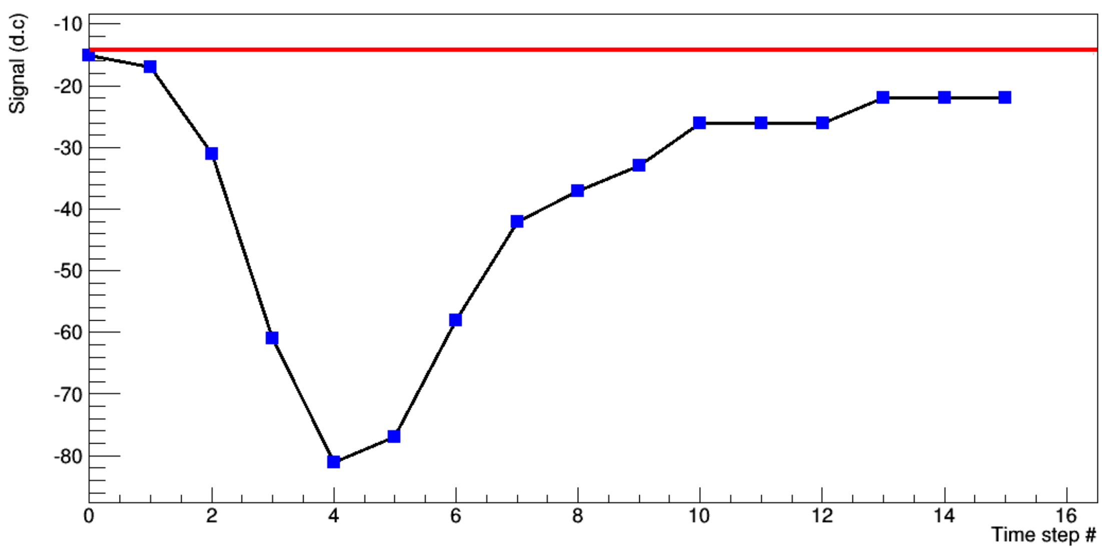

Figure 2.9: Example of a typical signal recorded by a VERITAS pixel (in this case, channel 2, telescope 2). The blue dots represent the measured signal, while the black line is drawn to guide the eye (it does not represent a fit of the data). Raw traces include a non-zero *pedestal value* (the red line, equal to approximately -15 d.c.), whose mean value over a run is subtracted prior to integration.

After this first computation step, we are left with an image similar to the one pictured on figure 2.8a, where the integrated charge value (or intensity) of each PMT is mapped onto the camera plane. Images of a gamma-ray showers consist of more or less elliptical patterns, which can be characterized based on a set of five parameters initially described by Hillas [22], and illustrated in figure 2.8b. Some of those parameters, like the distance of the ellipse's centroid to the center of the camera's field of view, will be correlated with the arrival direction of the original gamma-ray in the sky; meanwhile, other parameters such as the ellipse's width, length and integrated charge will correlate with the energy of the gamma ray responsible for the event. Finally, the recognition of characteristic ellipse shapes and sizes will also be extremely useful in building discrimination parameters to remove cosmic-ray background from the data.

In addition to the data obtained from individual telescopes, one can use the stereoscopic power of the telescope array to reconstruct the geometry of the gamma-ray shower. By projecting the image of all four telescopes onto a single camera plane (figure 2.10a), it is possible to observe that the ellipses from different telescopes all converge toward a given point on the camera's field of view: this allows one to estimate the sky coordinates of the gamma-ray photon. By projecting the same ellipses onto the ground plane (figure 2.10b), it is once again possible to see that the former also converge toward a particular location, indicative of the lateral distance between the array and the center of the Cherenkov light pool, also known as the *impact parameter*.

The many correlations existing between IACT images and a gamma ray's energy and arrival direction is best exploited through the use of Monte Carlo (MC) simulations, which are used to generate *lookup tables* that will associate a particular set of image parameters with a given photon energy and shower geometry. To generate these tables, a large number of gamma-ray showers of various energies and origins are generated by the MC algorithm, and fed through the *Instrument Response Function* (IRF) of VERITAS. An IRF is a complex set of functions which attempt to mimic the sensitivity of the entire hardware chain, from the optical properties of the telescope mirror, to the electronic performances of the camera's PMT, and the subsequent signal processing chain of the FADCs. The values of those IRF files are the results of extensive calibration measurements initially made on every individual hardware equipment of the telescopes, and on array-wide calibration techniques used regu-

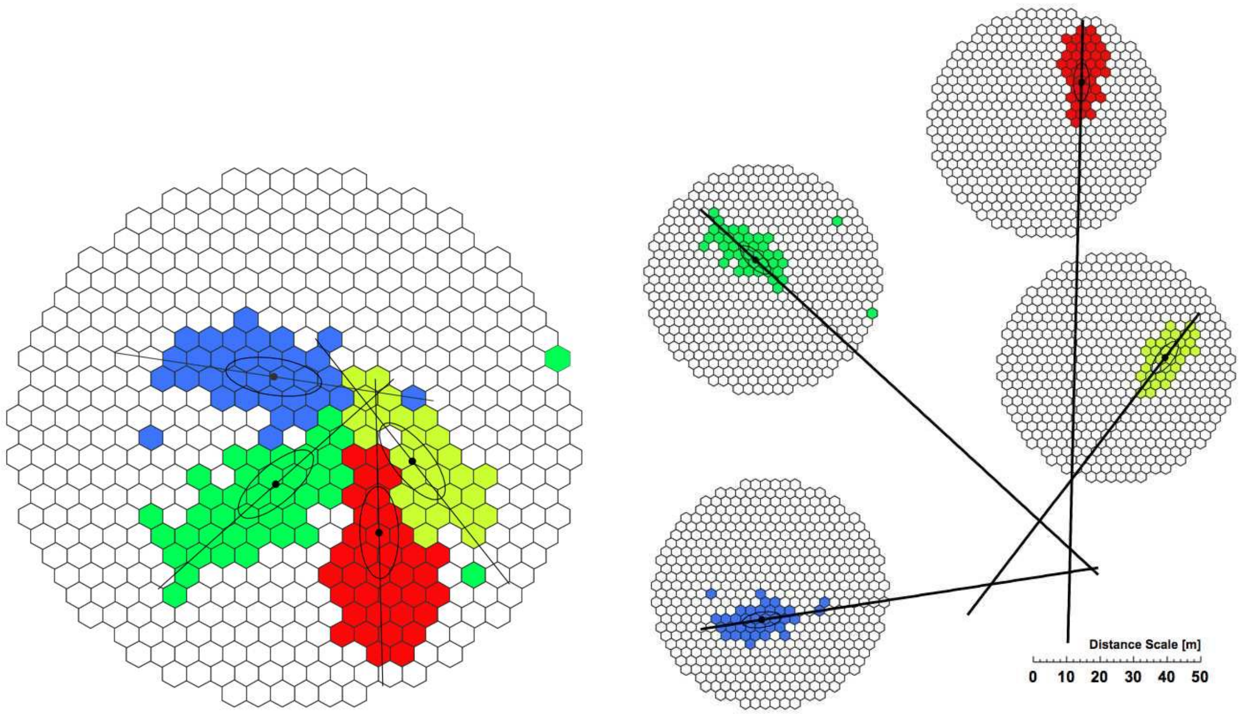

(a) Camera plane (b) Ground Plane

Figure 2.10: Example of a gamma-ray shower event reconstruction. a) By projecting the Cherenkov ellipses onto a single camera plane, it is possible to retrieve the position in the sky the shower came from. b) By projecting the same ellipses on the ground, the impact parameter of the shower can be reconstructed. Source: [20].

larly to assess the evolution of the telescopes' sensitivity over time. This detailed description of the array's performances allows us to predict the angular and energy resolution of the experiment as a function of various environmental and observing conditions, such as zenith angle, seasonal atmospheric effects, and background noise level.

Armed with the image information from each telescope and the MC lookup tables, we are equipped to proceed to the last step of the raw analysis process: background noise suppression, which is synonymous with the *gamma-hadron separation* process. As it was seen in section 2.2.4, several hardware-based trigger mechanisms have been installed on VERITAS to eliminate some of the background noise. Unfortunately, this system is powerless to remove from the data events caused by cosmic-ray showers, which are much more numerous than gamma-ray showers, and also produce Cherenkov radiation on the ground. Fortunately, the morphology differences between hadron and gamma-ray showers described in section 2.2.1 are also visible in the Cherenkov light images they leave in IACT cameras: photon-initiated showers will produce clean, elliptic shapes, while hadron-initiated showers will produce messier and rounder shapes (see figures 2.4a and 2.4b). By applying cuts on the width and length of the IACT images, it is possible to reject up to 99% of cosmic-ray events, allowing for a better signal-to-noise ratio [20].

2.3 Astrophysical science with IACTs

Finally it is time to do astrophysics with the VERITAS data as we now have, at this point in the analysis chain, a list of probable gamma-ray photons of given energy and location on the sky. From the sheer magnitude of the energies covered by IACTs, it can be easily understood that the astrophysical sources observed in gamma-ray astronomy are extreme in nature. The fact that certain physical processes are able to emit photons of such high energy is by itself strong evidence that at the core of these sources lies physical environments that are highly different from the ones we find ourselves in, and cannot be reproduced in even the most energetic particle colliders. Since the first detection of a TeV gamma-ray source in 1989 [9], many different astronomical objects have been discovered and studied at very high

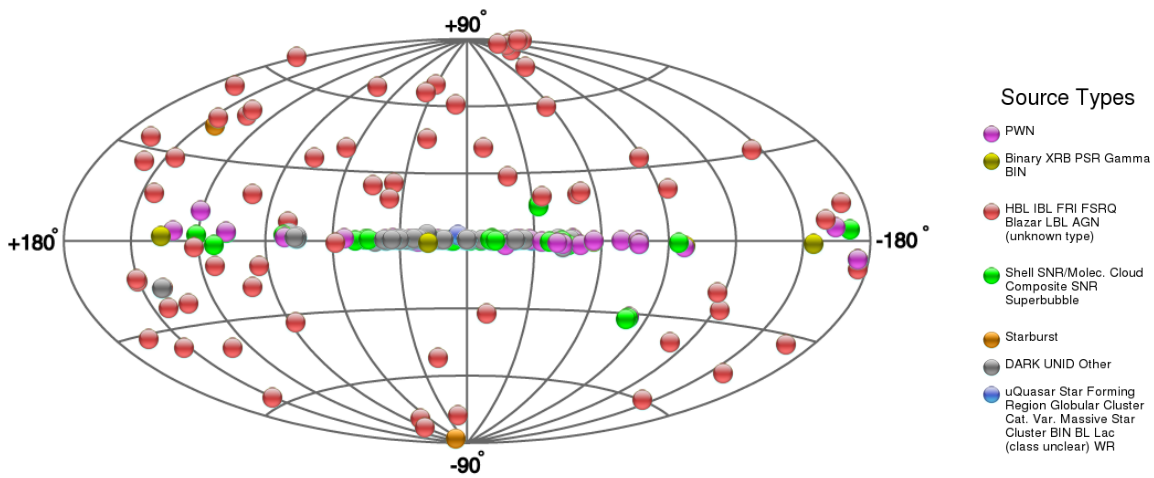

Figure 2.11: Map of the TevCat VHE sky catalogue, as of October 2016. The map is drawn in galactic coordinates, centered around the Galactic Center Sgr A*.

energies. Some of the most common categories of gamma-ray sources will be presented here, the list being far from exhaustive.

2.3.1 Galactic Sources

In our "immediate" vicinity, the Milky Way is host to a number of high-energy processes, most of them associated with highly compact stellar objects such as *neutron stars*, or the remnants of their birth process, namely *supernovae remnants* and *pulsar wind nebulae*. The discovery of pulsed gamma-ray emission from the Crab pulsar above 100 GeV is an example of a discovery made by VERITAS in its study of galactic objects [23]. Our galaxy is also home to several *X-ray binaries*, some of which are capable of producing TeV emission [24]. Finally, the *Galactic Center, Sgr A**, is a source of gamma rays that is the subject of extensive research, as the nature of its gamma-ray emissions is not yet understood [25] [26].

2.3.2 Active Galactic Nuclei

Constituting the "bread and butter" of gamma-ray astronomy outside the Galactic plane, *Active Galactic Nuclei* (AGN) are believed to be regions of very strong accretion activity around the supermassive black holes of certain galaxies. Obervations of AGNs have been carried at all electromagnetic wavelengths; in the case of VHE astronomy, the gamma-ray flux observable from a certain class of AGN called *blazar* is produced inside a *relativistic jet* structure, perpendicular to the plane of the active galaxy, and pointed by chance toward the observer. Of the 141 identified TeV sources currently known (see figure 2.11), 64 of them are blazars, making them the most populous class of VHE gamma-ray sources [27].

2.3.3 Multi-messenger Transient sources

Ground-based Cherenkov telescopes like VERITAS have set up over the year a number of joint monitoring programs for various types of transient astrophysical events. One of the most important concerns *gamma-ray bursts* (GRB): extragalactic flashes of gamma rays, believed to be highly beamed, which were first detected in the 1970's [28]. Rapid follow-up observations in the gamma-ray domain are also desired when looking for an electromagnetic counterpart to astrophysical transients detected via gravitational waves or neutrinos. Fast-response alert systems similar to the GRB program have been set up with neutrino detectors such as IceCube [29], and gravitational wave detectors like Advanced LIGO [30]; it constitutes a novel step toward the new discipline of *multi-messenger astronomy*.

2.3.4 Search for new physics

Finally, the observation (or non-observation thereof) of gamma-ray fluxes in parts of the sky devoid of known gamma-ray emitters can also be useful to constrain various hypotheses about the physics beyond the Standard Model. For instance, IACTs can take part in the search for dark matter (DM), by constraining the parameter space in an energy range that is not reachable by particle physics experiment [31] [32]. Finally, the high timing resolution of IACT detectors is sensitive enough to impose constraints on Lorentz invariance violation, by observing and accurately timing the arrival of photons from transient gamma-ray events like flaring blazars [33].

3 The VERITAS camera calibration system

3.1 The Camera Pixels

In order to detect very faint and fast light pulses such as the ones produced by gamma-ray showers in the atmosphere, all established atmospheric Cherenkov observatories have thus far relied on *photomultiplier tubes* to make up the light sensing pixels of their cameras. Invented in 1934, photomultiplier tubes (or PMTs) are low-light detectors that combine the power of the photoelectric effect with that of electron-multiplying dynodes to convert the signal of single photons into an amplified electronic signal. The physical principles behind the workings of a PMT are illustrated in figure 3.1.

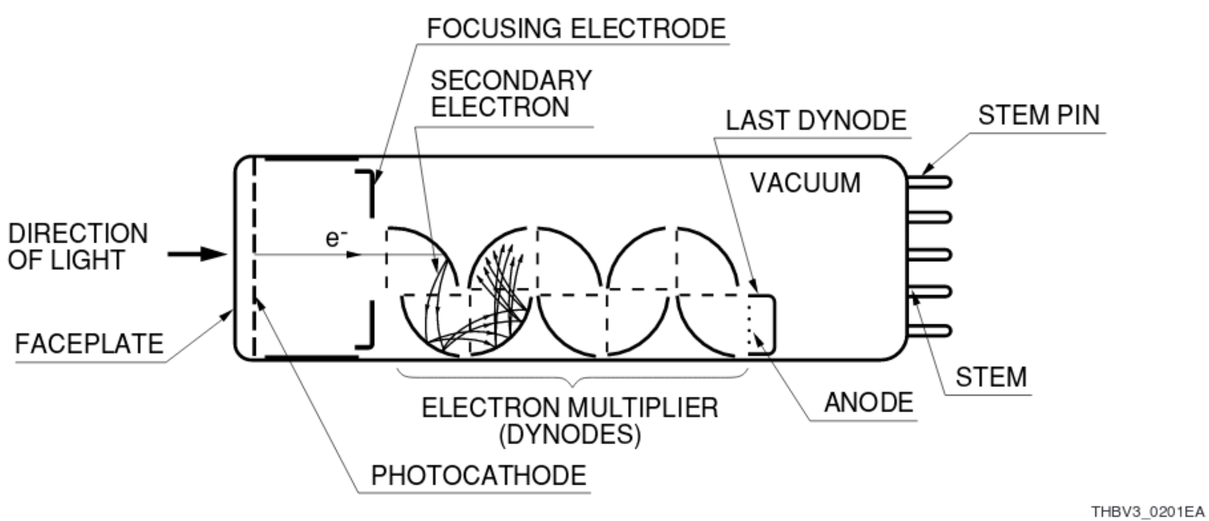

Figure 3.1: Schematic of a Photmultiplier Tube (PMT). A photon reaching the detector is converted into a photoelectron by hitting a semi-transparent photocathode; the photoelectron is then multiplied by a chain of dynodes individually held at a relatively high voltage potential (100-200 V). The result is an electronic signal at the anode that is amplified many folds. Image taken from [34].

When light reaches the sensor, some of the photons impact a semi-transparent photocathode, which usually consists of a thin layer of low potential metal (or mixtures such as bialkali: Na-K-Sb) deposited on the inside of an evacuated glass tube. Under the principle of the photoelectric effect, a photon will collide with outer-shell electrons of the photocathode, and impart to one of them kinetic energy K_{pe}. The energy imparted to one electron (which will subsequently be referred to as the photoelectron), is given by equation 8

$$K_{pe} = E_{photon} - \phi_{pc} \tag{8}$$

In the above equation, ϕ_{pc} refers to the potential energy barrier of the photocathode material, called the *work function*, which we require to be low for maximum efficiency. If the energy of the incident photon is sufficiently high, a photoelectron will be ejected from the photocathode, and will be pulled toward the first of a series of *dynodes* by electrostatic attraction. Dynodes typically emit several electrons for each incident electron striking them. These dynodes are configured in a linear chain, and a relatively high voltage (100-200 V) is applied between each of them to accelerate and direct the emitted electrons to the next member of the chain. This will result in an electron cascade that will amplify the initial photon signal by a certain *gain*, which is a function of the form $G_{PMT} \propto (\Delta V^k)^n$, where ΔV is the voltage potential difference between each dynode, n is the total number of dynodes in the PMT and k is an empirical constant which has a value between 0.6 and 0.8 [34].

On a VERITAS camera, illustrated in figure 3.2a, each PMT is integrated into a slightly more complex subsystem called the *pixel*. This subsystem, illustrated in figure 3.2b, includes a protective enclosure for the vacuum-sealed glass tube and high-voltage electrical connections, a Winston-type [35] light collector at the front to maximize the effective light collection area and cut out photons that are not coming from the mirrors, a small pre-amplifier circuit which will be described in section 3.2, a 75 Ω-impedance coaxial output cable, and a current monitor [36]. The latter is used in the monitoring of nightly observing conditions: because over-illumination of a pixel will lead to the deterioration of its photocathode, no observations are performed with the latter once the current flowing through it surpasses a threshold of $15\mu A$. It befalls from this safety condition that pixels illuminated by light from bright stars are turned off during a run, and sky observations are essentially prohibited while the Moon is full, reducing the observatory's yearly exposure by approximately a week for every moon cycle.

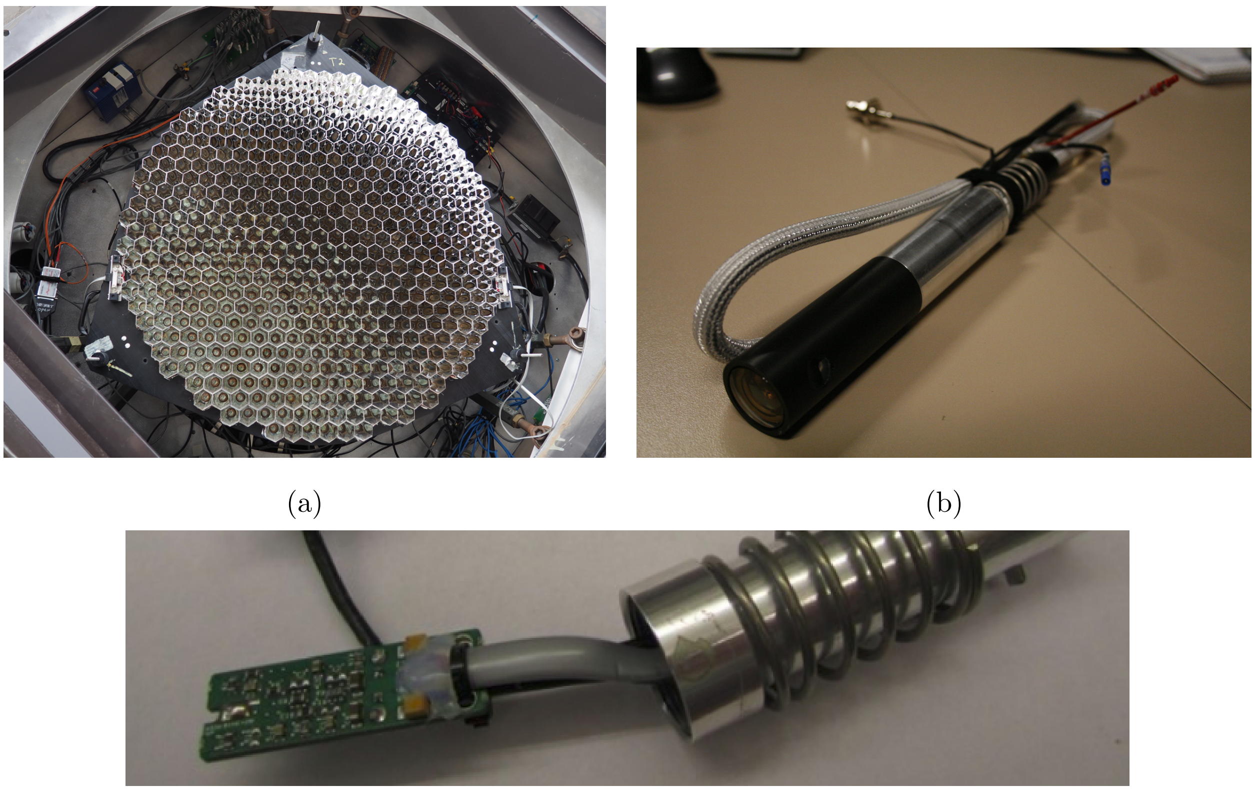

(a) (b)

(c)

Figure 3.2: a) The camera of one of the VERITAS telescope, consisting of 499 pixels arranged in a "close-packed-hex" configuration to maximize the covered area. Truncated Winston cones are installed on top of individual pixels. b) image of a Hamamatsu R1050-100-20 MOD photomultiplier tube in its pixel assemly, without the Winston cone. c) close-up of the pre-amplifier board, which is located near the base of each PMT tube.

The number of signal electrons produced per photoelectron created at the photocathode is called the *gain* of the combined PMT/electronics amplification chain. It is constant for a given high-voltage bias, meaning that the measured signal at the output of an FADC channel will be linearly proportional to the number of photons detected by the PMT associated to that channel: two photons triggering the photocathode will produce twice as many electrons at the output.

Unfortunately, the linearity of a PMT signal is only guaranteed within a certain range of incident light intensities. Once a certain number of photons enter the device, various non-linear effects begin to reduce the value of the PMT's gain, until a state of saturation is reached. It is therefore important to avoid saturating the PMT, as its signal output ceases to be proportional to the incident light level.

3.2 Cherenkov light amplification chain

Figure 3.3 illustrates the many signal processing steps that occur after photons are detected by a PMT, and converted into an electronic pulse by the PMT's dynode chain. The first electronic amplification stage consists of a pre-amplifier that is installed directly into the PMT's support socket (see figure 3.2c); the pre-amplifier is powered through a custom-built current monitor board, which also measures the PMT anode current and transmits it to the camera monitoring software. The pre-amplifier multiplies the PMT pulses by a factor of two. [37]

The next amplification stage is a *high-low gain switch*, and was designed in order to increase the dynamic range of the FADC's 8-bit voltage readout. Because of hardware limitations that will be discussed in section 4.5.1, the voltage digitizer electronics will produce saturated outputs if a very bright pulse is detected by a PMT. To fix this problem, the signal coming out of the pre-amplifiers is split into three copies: one goes into a comparator, while the other two are sent to a *normal* or *high-gain*, and a *low-gain* amplifier circuit. Like their name suggests, each circuit applies a different amplification factor to the signal: the high-

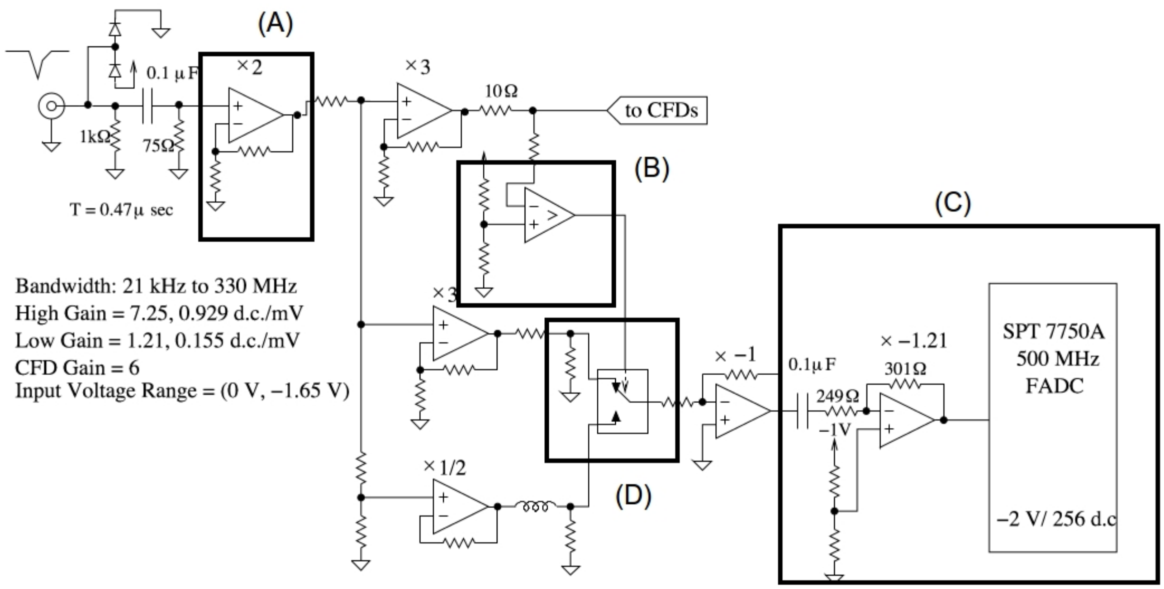

Figure 3.3: Schematic of the Cherenkov amplification circuit. Pulses coming out of a PMT are first amplified by a pre-amplifier (A) located inside the pixel casing. The pulse is then split into three copies: one goes to a comparator (B), while the other two go respectively to a high-gain (x3) and a low-gain (x1/2) amplifier. The comparator controls the high-low gain switch (D), which selects the amplified pulse that will be sent to the FADC (C). Source: [37]

gain circuit multiplies the PMT output by 3.0, while the low-gain circuit multiplies it by 0.5. Based on the amplitude of the pulse measured by the comparator, a *high-low-gain switch* will determine which of the amplified signal will be sent to the FADC. If the comparator's signal pulse stays below its threshold, the switch sends the high-gain pulse into the digitizer. If the threshold condition is met however (which is the case for very bright pulses), the switch will send through the low-gain pulse; along the way, a high-low bit is switched in the data-stream, indicating to the offline analysis software that the pulse for this particular channel was read in low-gain mode.

3.3 Statistics of a PMT-amplifier system

In a first-order approximation, a PMT can be thought of as a black box which converts an initial photoelectron into a fixed number of signal electrons via equation 9.

$$N_{electrons} = G \cdot N_{pe} \tag{9}$$

Suppose we illuminate this PMT with a pulse of light that contains precisely $N_{photons}$. Neglecting the electronic noise from the amplifier circuit, and assuming that the PMT's gain is unique and constant, the only source of statistical fluctuations in the light measurement will come from quantum mechanical processes at the photocathode, which convert incoming photons into photoelectrons with a probability given by a Poisson distribution of parameter μ_{pe}:

$$P(N_{pe}) = \frac{\mu_{pe}^{-N_{pe}} e^{-\mu_{pe}}}{N_{pe}!} \tag{10}$$

The average number of photoelectrons produced by the PMT upon detection of a pulse will be $\mu_{pe} = N_{photons} \cdot \eta \cdot (1 - R)$, where η is the quantum efficiency of the photocathode, and R the reflection coefficient of the PMT glass. For a large number of detected pulses of intensity N, one can expect that the mean number μ_N of signal electrons obtained at the end of the signal amplification chain will be given by:

$$\mu_N = G\mu_{pe} \tag{11}$$

Where G is the constant gain of the "black box" PMT-amplifier system. The standard deviation of the electron distribution will also mirror the initial photoelectron distribution, with the addition of the G constant from the amplifier.

$$\sigma_N = G\sigma_{pe} \tag{12}$$

Furthermore, variance and mean are equal quantities in a Poisson distribution, which means that we can replace σ_{pe}^2 by $\mu_{pe} = \mu_N/G$ and write down a relationship between the first and second moments of the electron signal distribution:

$$\sigma_N^2 = G\mu_N \tag{13}$$

From equation 13, the value of the PMT-amplifier gain can be estimated using flashes of light with various intensity levels N: the slope of the σ_N^2 vs. μ_N plot will correspond to the absolute *photostatistics gain* G.

The validity of equation 13 is limited by two assumptions: that statistical fluctuations from the flasher light output and electronic noise are negligible, and that the gain of the photomultiplier is deterministic (ie. one detected photon will always yield G electrons). In reality, the amplification process occurs in steps, at each one of the PMT's dynodes; statistical fluctuations are associated with each one of these steps, thus affecting the final number of electrons in the output signal.

The nature of these stochastic processes have been (and are still today) the subject of many experimental studies and simulation models [38] [39] [40] [41]. For the purpose of this work, it suffices to say that it has been proven that the processes at each dynode are independent of each other, and can usually be appropriately modeled by either Poisson or Polya [42] distributions. If we add on top of that the electronic noise from the amplifiers and fluctuations in the light source, a more thorough estimation of a VERITAS pixel's average gain can therefore be given by equation 14:

$$\langle G \rangle = \frac{\sigma_N^2 - \sigma_{ped}^2 - B_f^2 \mu_N^2}{\mu_N (1 + \beta^2)} \tag{14}$$

Where σ_{ped}^2 is the variance of the pedestal measurement, $B_f = \frac{\sigma_f}{\mu_f}$ is called the *resolution* of the flasher, and $\beta = \frac{\sigma_{spe}}{\mu_{spe}}$ is a constant corresponding to the ratio of the width to the mean value of the single photo-electron spectrum peak [43]. Section 3.5.1 will explain how the various elements of equation 14 are treated in the VERITAS calibration procedure.

3.4 First-generation flasher system

Originally designed in 2009[7], the current instrument used to calibrate the response of a camera consists of a flasher that simulates Cherenkov light pulses using a set of seven light-emitting diodes (LEDs). The electronic circuit that drives the flasher is illustrated in figure 3.4; it consists of an assembly of simple-logic integrated circuits, which use pulses from an external trigger to increment a binary counter (U5) that cycles from the 000 to the 111 state (that is, from 0 to 7). The output of the counter is fed to a demultiplexer (U6), which sequentially turns the 7-LED driver circuits at a logical LOW state using interconnected AND gates (U7-U8). The output of the AND gates is fed to an array of NOR gates (U9-U12), which drives current to the LED circuits (an assembly of LEDs, resistor and Schottky diodes), in the case of a LOW logic state.

The entire circuit is encased inside a commercial maglite casing, to protect it from weather hazards. At the ouput of the flashers, the light from all seven LEDs is randomized with the use of a 50-mm opal diffuser from Edmund Optics, to ensure that the beam sent to the camera is uniform in intensity.

The external trigger system used to operate the flasher differs from the conventional, 3-level trigger used during normal observations, as the calibration light is emitted directly

[7]Prior to this epoch, gain calibration measurements were produced using a pulsed laser system that only produced single-intensity pulses at a rate of 1 Hz. Details on this system can be found in [44].

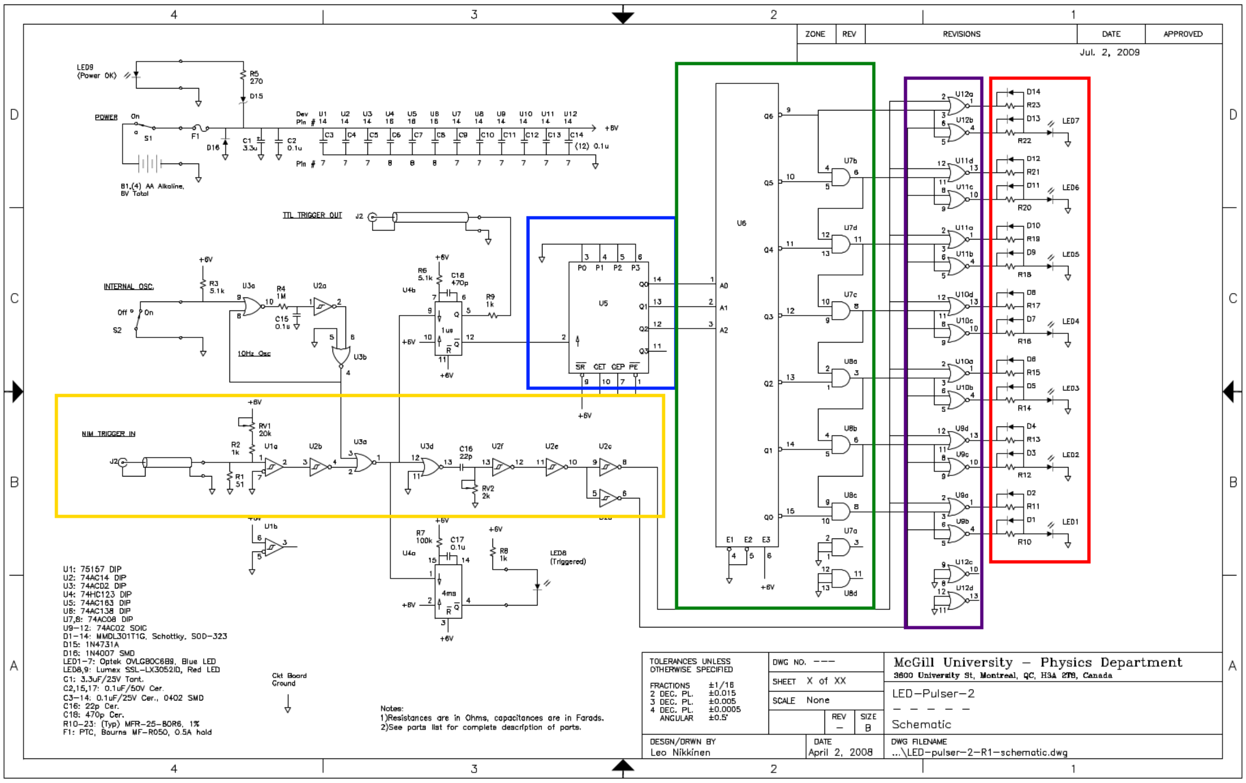

Figure 3.4: Electronic circuit of the current generation of LED flashers. Important sections have been labelled with different colours: the external trigger signal processing (yellow), the binary counter (blue), the demultiplexer and its interconnected AND gates (green), the NOR gates (purple), and the LED driver circuit (red).

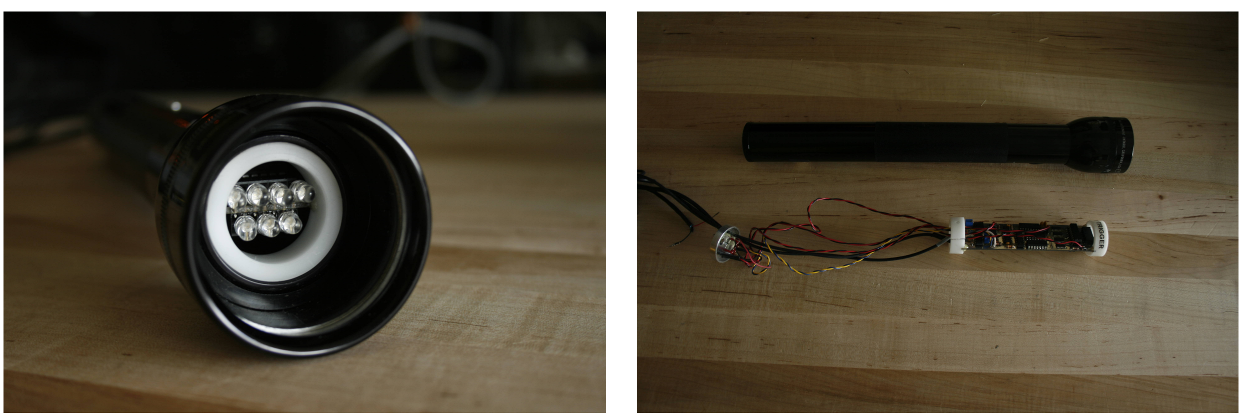

Figure 3.5: The current 7-LED flasher system for the VERITAS cameras (with the opal diffuser removed).

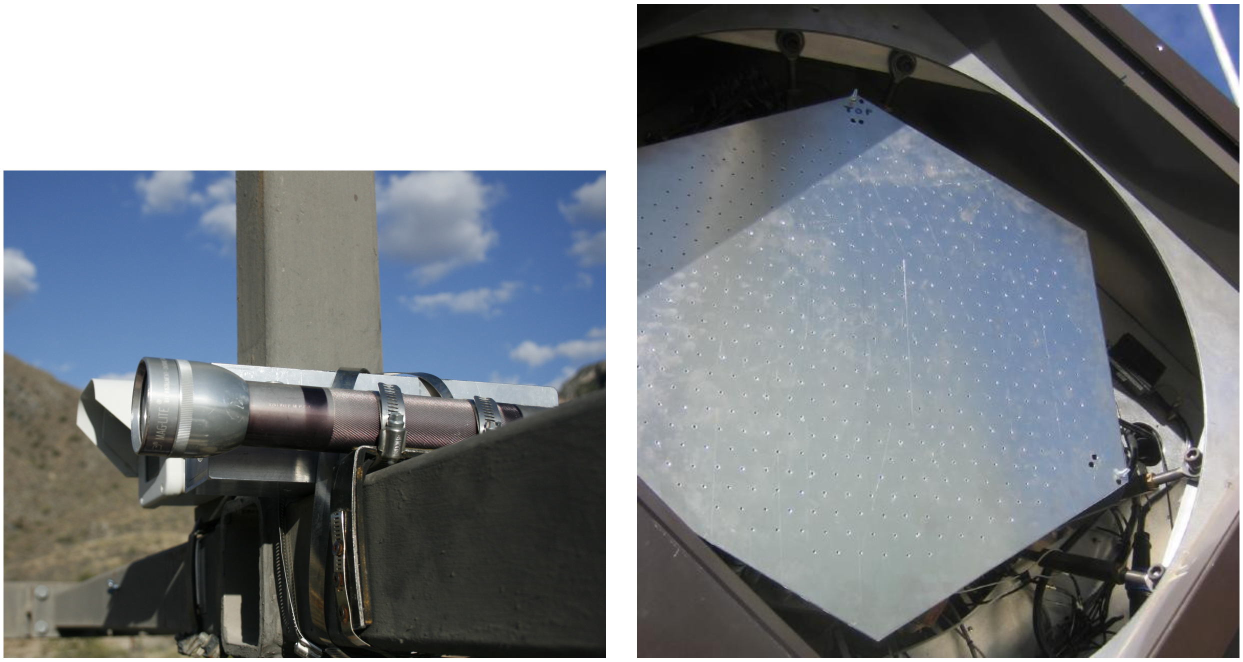

Figure 3.6: *Left:* Location of the LED flasher, on the cross-arm of the telescope. *Right:* Photograph of the holey plate used during the single-pe calibration runs: each plate has 3-mm holes that allow only one or two photons in each pixel.

in front of each telescope's camera, and does not originate from the sky: instead, a function generator produces a NIM trigger signal that is first converted to a light pulse by an LED, carried from the L3 control room to each telescope via a system of LEDs coupled to optical fibers[8], and reconverted to a NIM pulse with the help of silicon photomultipliers [45].

Designed to work at a nominal triggering rate of 300 Hz, the addition of the flasher to this array greatly reduced the amount of time spent on calibration measurements, thereby saving precious observation time for the pursuit of the VERITAS science goals. [44]

Once mounted on the telescope cross-arm (figure 3.6), the LED flasher produces pulses similar to those of an atmospheric Cherenkov event, uniformly accross the camera plane. The intensity of these pulses will increase linearly with the number of LEDs activated (producing

[8]The use of fiber optics instead of coaxial cables was initially proposed to minimize the risk of damages to the experiment's electronics in the event of a lightning strike.

a sequence of 0,1,2,3...7 lit LEDs), which will be useful to several calibration techniques described in the following section.

3.5 Overview of calibration procedures

3.5.1 Relative and absolute gain measurement

Every night, the observing crew uses the flashers to perform a 2-minute run during which the instruments produce approximately 36000 Cherenkov-like light pulses aimed at the cameras. The electronic response of each of the camera's channels is read by the FADCs, and the resulting data file is flagged as the calibration run of the night's observations.

The motivation for this calibration procedure is to correct the offline analysis for gain variations between pixels, and perform once or twice a year a proper flatfielding of the camera during observations. Because of differential aging between the camera channels, the PMT gain will vary between pixels, for a given voltage bias applied. In order to level the response of the camera across its entire field of view, that bias is finely tuned for each channel, based on how its response to the flasher pulses compares to a *monitor* charge value [44]. That monitor is constructed out of the statistics of the entire camera: channels are divided in 54 groups of 9, and the monitor is the average of the median pulse intensities of each subgroup [46]. By plotting the mean charge of a pixel against its corresponding monitor value, and measuring the slope of this graph (see figure 3.7a), it is possible to obtain the relative gain of that pixel compared with the rest of the camera. For a proper flat-fielding, we require the value of that gain to be close to one: this can be done by adjusting the voltage bias applied to the pixel, thus narrowing the statistical distribution of the pixel gains, as can be seen in fig 3.8.

During offline analysis, the calibration information recorded in the nightly flasher run is also used at the early stages of the VERITAS analysis packages to estimate the absolute photostatistics gain of each pixels, using a simplified version of equation 14. First, the mean charge corresponding to the pedestal, μ_{ped}, is removed from the integrated trace charge μ_N. Then, for every LED light level N, the variance of that channel's charge distribution, σ_N, is

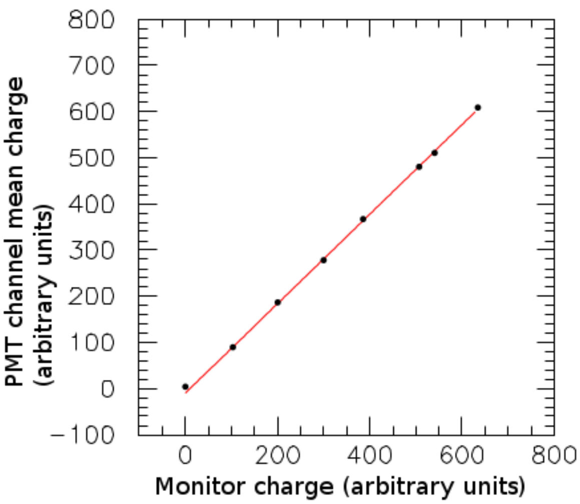

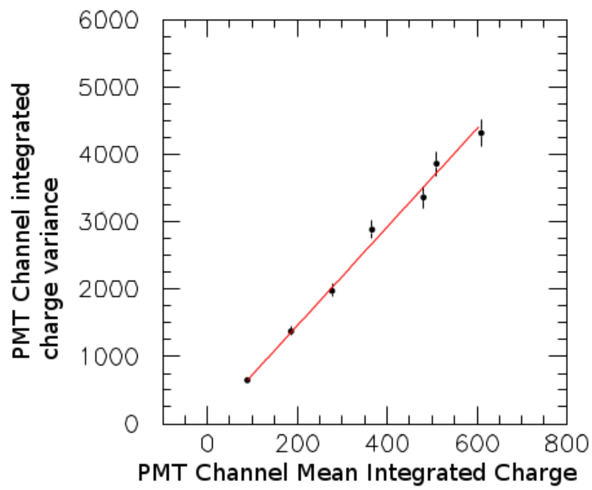

(a) (b)

Figure 3.7: a) Example of a relative gain measurement. The mean integrated charge of the pulses detected in a VERITAS PMT channel is compared to the value of a monitor, constructed out of the statistics of the entire camera. The slope of this plot will give a value of the relative gain of this particular channel, with respect to the monitor. b) Example of an absolute gain measurement. Here, the variance and pedestal-subtracted mean of a channel's integrated charge distributions are plotted together. The slope of this plot will give a value for the absolute gain of the channel, as calculated with eq.13. Source: [44]

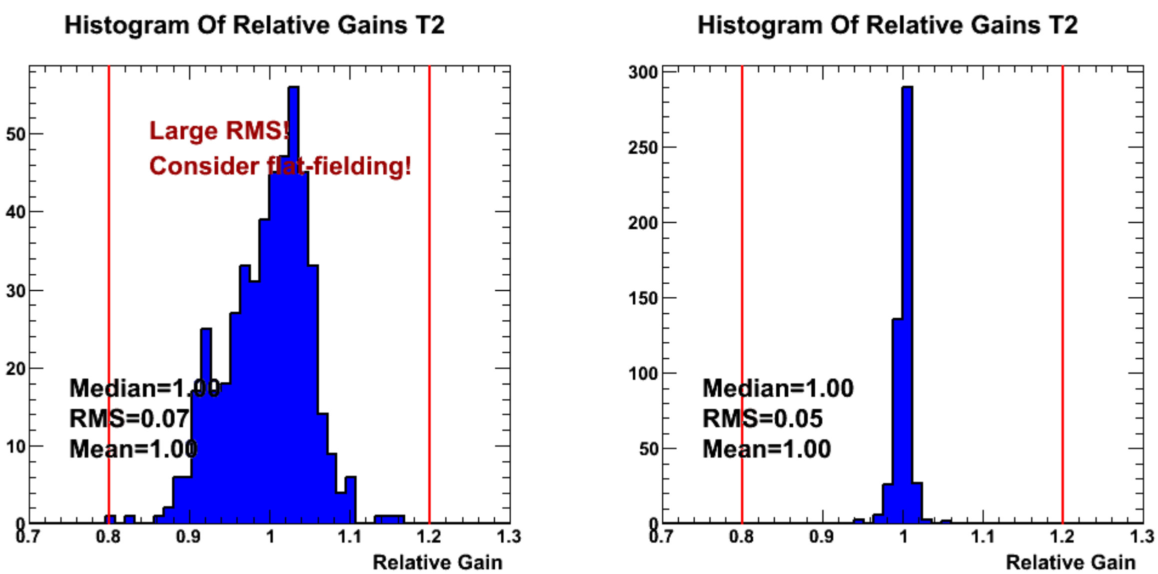

Figure 3.8: Example of a situation for which a flat-fielding procedure is necessary. Left: The relative gain distribution (ie the slope of the mean channel charge vs. the mean monitor charge) is very broad, meaning that the responses of the camera pixels in telescope 2 is not uniform. Right: A flat-fielding procedure was accomplished the following days, and the gain distribution became more narrow as a result. Both figures were generated from the VERITAS Data Quality Monitor (DQM) software.

plotted against its pedestal-free mean charge value ($\mu_N - \mu_{ped}$).

$$\sigma_N^2 = \langle G \rangle \frac{\mu_N - \mu_{ped}}{(1+\beta^2)} \tag{15}$$

In this version of the gain calculation, terms like $\sigma^2_{pedestal}$ and B_f are assumed to be negligible, while β is experimentally measured in a special *single-PE calibration* run, which is described in the next section. Given the value of β for a particular channel, one can fit the σ_N^2 vs. $(\mu_N - \mu_{ped})$ plot to obtain the value of its absolute gain. Figure 3.7b illustrates such plot for one of the channels of a VERITAS camera, using data from a flasher calibration run.

3.5.2 Single PE and high-low gain calibrations

Section 3.3 described how the average gain of a pixel is a function of stochastic processes at the PMT dynodes. It introduced an empirical parameter, β, that is associated with the statistical distribution of single photoelectron events. This parameter can be measured on the VERITAS cameras by placing plates with 3-mm apertures in front of the pixels, such as to only let through a handful of photons per LED pulse and block most of the NSB. By integrating the PMT signal of a channel, and sorting the value of this integrated charge into a histogram, one can fit the resulting distribution with several Gaussian functions, which will correspond to the integrated charge distribution of a 0,1,2...n photon(s) event. Thus, β can be calculated out of the first and second moment of the Gaussian fitted for the 1-pe electron distribution. Note that since the mean and variance of a 2,3...n-pe event are related to the moments of the 1-pe Gaussian distribution through Poisson statistics, a charge distribution like the one in figure 3.9 can be fitted with only five free parameters: mean and variance of the 0-pe (ie pedestal) events, mean and variance of the 1-pe events, and the mean number of photoelectrons detected.

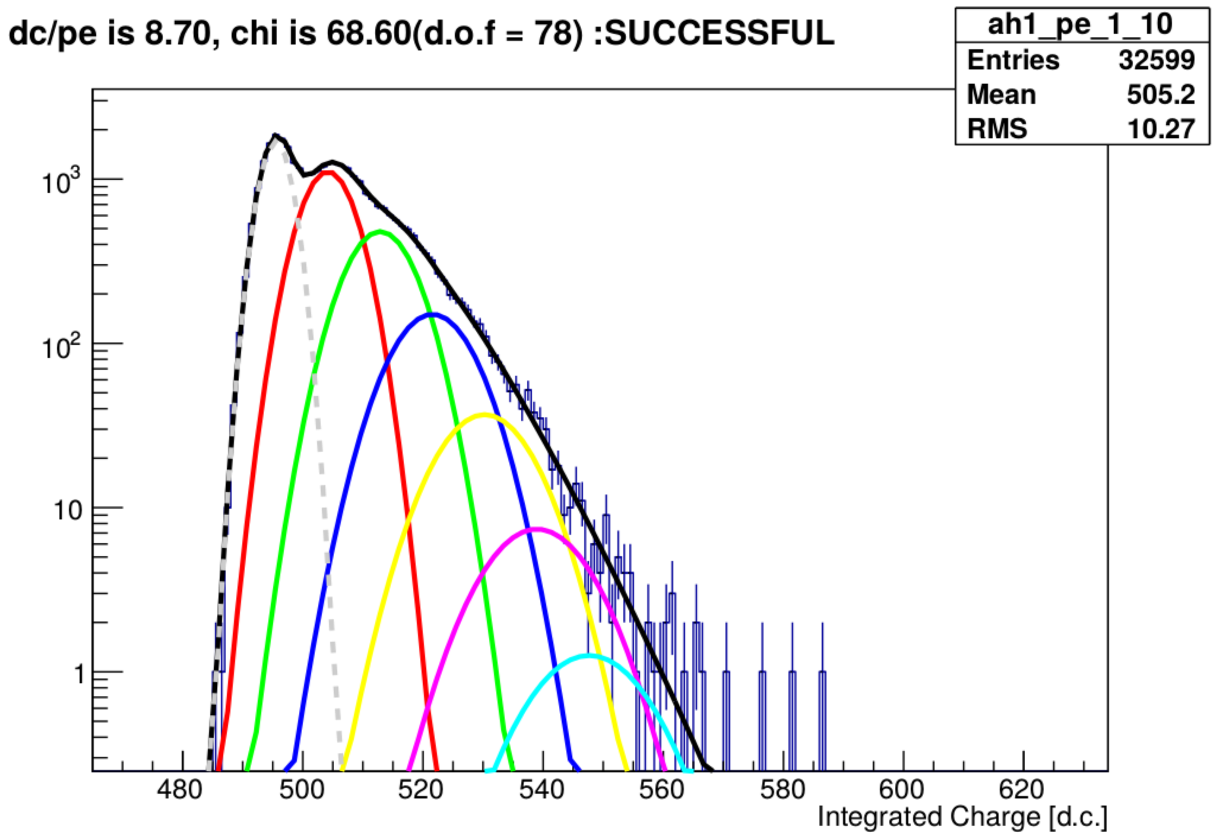

Figure 3.9: Example of a single-PE calibration result for channel 10 of telescope T1. The width and mean of the 1 p.e (red) histogram is used to correct the photostatistics measurements by the β factor. Because these charge distributions follow Poisson statistics, they can be fitted using only five free parameters.

Another monthly calibration measurement made on the camera is the *high-low gain calibration*. In section 3.2, we have seen that there is a factor of approximately 6 between the intensity of the pulses read through the low-gain and high-gain modes of the FADC. Under experimental conditions however, that ratio varies slightly between the telescope FADC boards, and must be monitored. During this calibration procedure, half the camera is switched to a low-voltage bias state, allowing most of the flasher pulses to be read in high-gain mode; from this ensemble of pixels, a monitor like the one used in relative gain calibration is built. Meanwhile, the other half of the camera is kept at regular bias, and hence most of these pixels will switch into a low-gain state when illuminated. By comparing the photostatistics response of the normally biased half of the camera to the monitor charge values, an experimental ratio of the high-low gain ratio is obtained[9].

3.5.3 Reflectivity and muon calibration

Other calibration procedures periodically take place, which do not relate to the characterization of the PMT responses, but are useful to isolate camera-related degradation of the IRF from other instrumental effects. One of them is the whole-dish reflectivity measurement (see figure 3.10a), where a CCD camera mounted on the OSS compares the image of a nearby star with its reflection on a white target positioned at the focal plane of the telescope. The difference between the luminosity of the star directly viewed in the sky and its image on the plane gives a measure of the global reflection coefficient of the mirror assembly.

Finally, a cross-calibration of the telescopes can be made by measuring the light intensity of the rings formed when muons moving parallel to the optical axis of a telescope are detected by the latter. The size of the ring formed depends on the Cherenkov angle, while the azimuthal intensity distribution of the signal depends on the impact parameter of the muon: if the particle passes directly through the center of the telescope, the ring formed in the camera will have an azimuthally uniform intensity. Figure 3.10b shows an example of a muon event that can be used in this type of calibration. Because the morphology of muon rings can be derived from the theory of single-particle Cherenkov radiation, the relative throughput of all four telescopes of the array can be calibrated based on the expected number of Cherenkov photons for a given muon image.

[9] Note that two flasher runs are necessary, to evaluate the response of both halves of the camera. The FADC integration window is also longer for this type of calibration, to reduce the uncertainties due to pulse clipping in the measurements.

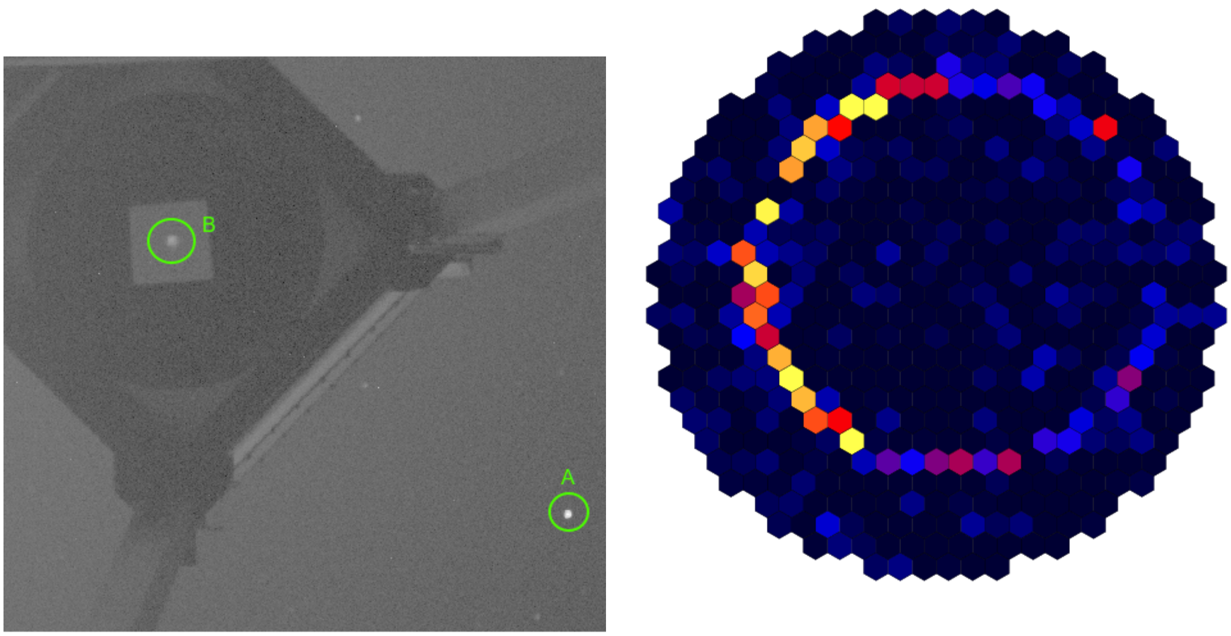

(a) (b)

Figure 3.10: a) Example of a Whole-dish reflectivity measurement, where the intensity of a star in the sky (A), is compared to the intensity of its image on the focal plane (B). b) Typical image of the Cherenkov ring produced by a muon on one of the telescope. The azimuthally anisotropic intensity of the ring is due to the fact that the muon passed near the telescope with a non-zero impact parameter. Source: [47].

4 The new generation flasher

4.1 Motivations for an upgraded flasher system

From 2010 to 2012, the VERITAS telescopes have been the subject of a major hardware upgrade, in which the pixels of the cameras have been replaced by PMTs with a higher quantum efficiency [48]. Because of the increased sensitivity of the new PMTs, the flashers can now only produce 2-3 pulses that will be sufficiently low in intensity to avoid triggering the high-low gain switch of a pixel. Above these levels, an increasing number of PMTs will switch to low-gain mode, as can be seen in figure 4.1. As a result, the calculation of the photostatistics gain in the high-gain mode, which corresponds to the slope of eq.15, is being interpolated out of only two or three data points. This lack of degrees of freedom (d.o.f) means it is not possible to verify the linearity of the PMT response, by comparing the linear fit to a more complex expression for the gain like eq.14. Given the total number of available LEDs, this d.o.f. problem also affects measurements in the low-gain mode, since only two or three LEDS are bright enough to trigger the switch.

Another problem encountered with the current LED flashers is their inability to probe the entire response range of the pixels in the low-gain mode. Because of an insufficient number of light levels, no calibrated light pulse is able to illuminate the PMTs such as to reach the region of the detector's response where non-linear effects and saturation come into play. This is problematic because in order to properly characterize the most energetic gamma rays (responsible for the brightess Cherenkov pulses), a proper modeling of the PMT light conversion process has to be made, since in these special cases the linearity assumption may not hold.

Given these two problems, the new flashers were designed with two specific requirements: add more light level data points in the absolute gain plots of both operating modes (high and low), and increase the absolute throughput of the flasher to better probe the end of the low-gain response range.

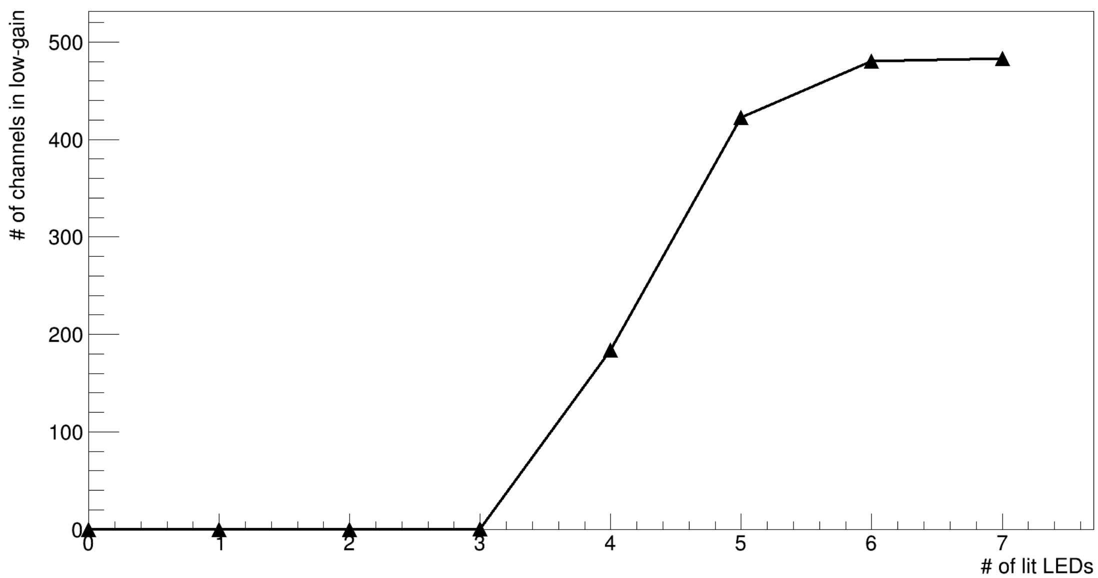

Figure 4.1: Number of channels that have switched to low-gain mode as a function of the number of LEDs that are lit during a given flasher event, on telescope 4 during calibration run 81957. Because of the limited number of LEDs on the current flasher, only 2-3 data points can be used in either mode to measure the gain. This is problematic if one wishes to study the linearity of the PMT response with more accuracy.

4.2 Circuit design

The schematics of the new flasher circuit are shown in appendix A, along with the technical specifications of its key components. Overall, the working principles of the new device are identical to the ones used for the old flashers (and have been described in section 3.4), with the difference that the number of LED circuits has been increased to 15. The circuits of the next-generation (V2) flashers also come with three trimmer potentiometers, labeled R5, R17 and R19 in figure 4.2: Each one of them controls a specific characteristic of the emitted light pulses. The first potentiometer (R5) sets the trigger level upon which the flasher will emit a pulse: it is a pull-up resistor that raises the DC voltage offset of the input trigger pulse above zero; when the signal is subsequently inverted, the resulting, positive pulse will be high enough to represent a positive-state logic level.

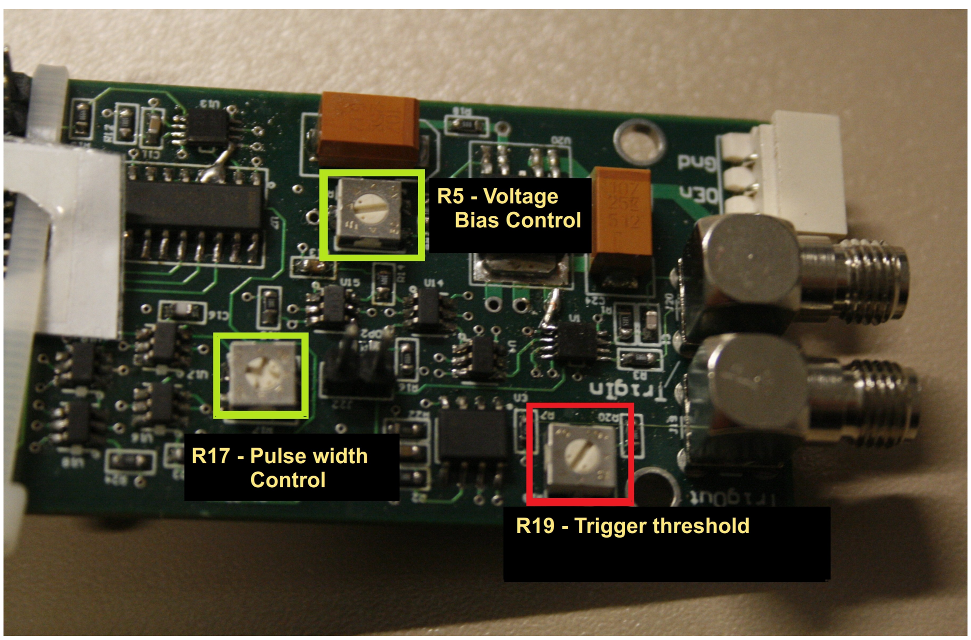

Figure 4.2: Close-up picture of the three adjustable potentiometers on the new flasher electronics. R5 sets the trigger level upon which the flasher will emit a pulse, R19 controls the voltage level of the circuit's supply voltage and R17 defines the width of the pulses sent to the LEDs.

The second potentiometer (R19) controls the voltage level of the circuit's supply voltage.

A slight increase in the overall bias voltage of the circuit will slighty increase the voltage of the pulses generated throughout the logic circuit, including the ones used to feed current into the LEDs, thus increasing the intensity of the light emitted.

The third, and most important control one has on the flasher output is the R17 potentiometer, which defines the width of the current pulses sent to the LEDs. The details of this circuit element are shown in figure 4.3. First the trigger signal is sent into one of two Schmitt-type triggers[10] (input 1 in figure 4.3). Second, the output of the first trigger (6) is connected to an RC circuit of time constant $\tau = RC$; the value of this constant can change, since the potentiometer R17 modifies the resistor value. Third, a wire connects the RC circuit's resistor voltage, V_r, to the input of the second Schmitt trigger (3). Figure 4.4 (top) illustrates the shape of the signal at this input: its duration will be independent of the duration of the trigger pulse (in blue), and will only vary with a change in the value of the circuit's time constant. Finally, when fed through the second Schmitt trigger, the signal will become a rectified, digital pulse whose width will be determined by the internal HIGH-logic threshold of the comparator. The bottom plot of figure 4.4 presents the shape and width of the final output pulse (4), for different values of potentiometer resistance.

4.3 Casing design and production

An important order of business regarding the new flasher system was the need for a new housing for the equipment. To accomodate for the greater number of LEDs on the circuit, and the eventual inclusion of a light monitor in the same instrument (a topic covered in detail in chapter 6), a new custom-built casing had to be designed and assembled. It needed to have sufficient free space inside to include several small PCBs, and be made with a material capable of enduring the rough environmental setting of southern Arizona.

A 3D computer-assisted design (CAD) software was used in order to facilitate the conception of the parts, and provide ready-made technical drawings that could be used by

[10] A Schmitt trigger is a comparator that uses the feedback from its output to modify its threshold; it is used to convert an analog signal into a digital pulse.

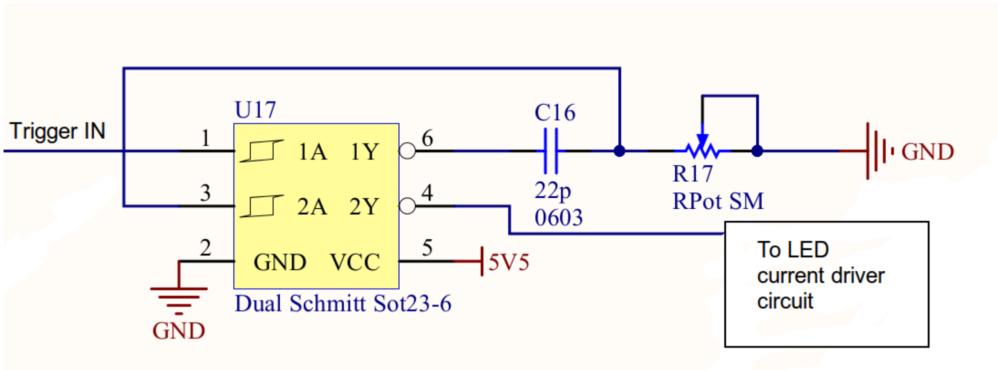

Figure 4.3: Electronic schematics of the pulse width modulator. The flasher trigger signal enters a Schmitt trigger through input 1. The Schmitt trigger redresses the pulse before sending it to an RC circuit of time constant τ (output 6). This circuit is used as a feedback for the second Schmitt trigger (input 3), by determining the width of the electrical pulse sent to the LEDs at output 4. Schematic courtesy of A. Gilbert.

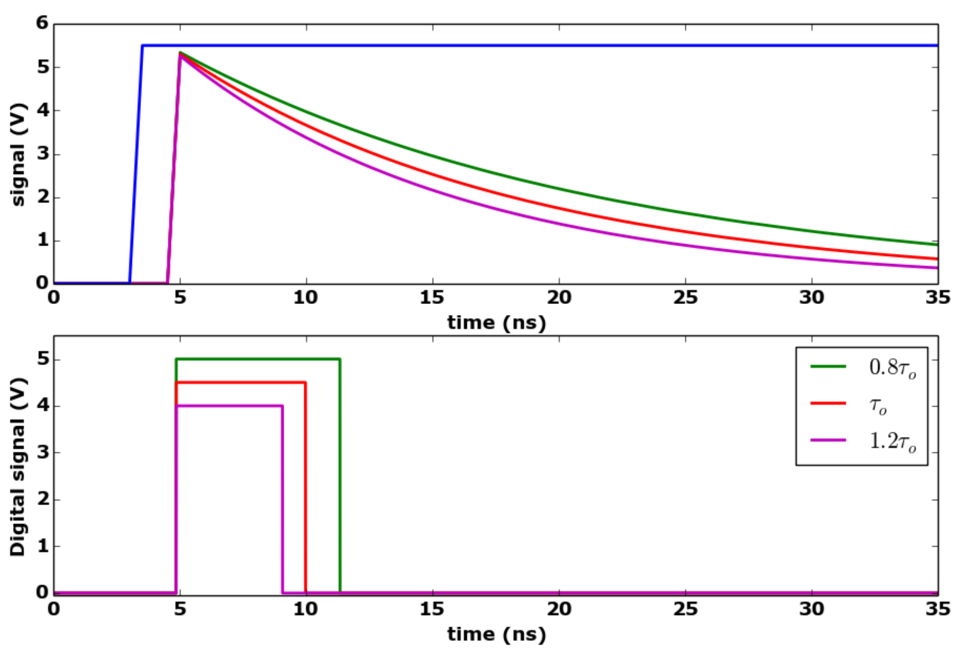

Figure 4.4: Simulation of the output signal generated by the pulse width modulator: upon reception of a trigger pulse (blue, input 1), the RC circuit at output 6 will respond in a manner that is dictated by the circuit's time constant. The greater the value of τ, the faster the drop in the resistor voltage, and the shorter will be the final digitized pulse (output 4), which is illustrated in the bottom plot. Note that the pulse heights of the bottom figure have been scaled to show the different pulse width more clearly.

professional machine shop technicians to produce the parts. Like with many prototyping projects, many iterations of the casing design were made, each of them aiming to limit the manufacturing steps needed to produce each parts. Consulting with qualified technicians and learning about the tools available to process the raw material (in this case, aluminum) allowed for a better insight of the time (and ensuing costs) needed to machine a particular element.

Figure 4.5 allows for a comparison of the initial design to the final product, which consists of a simple assembly of three elements: a mount for the opal diffuser, a connector backpannel, and a rectangular base plate onto which everything (including the electronics) is secured in place by screws. The entire flasher assembly inserts itself into a square tube of aluminum, thereby minimizing the number of sealed joints required to protect the interior components from the rain.

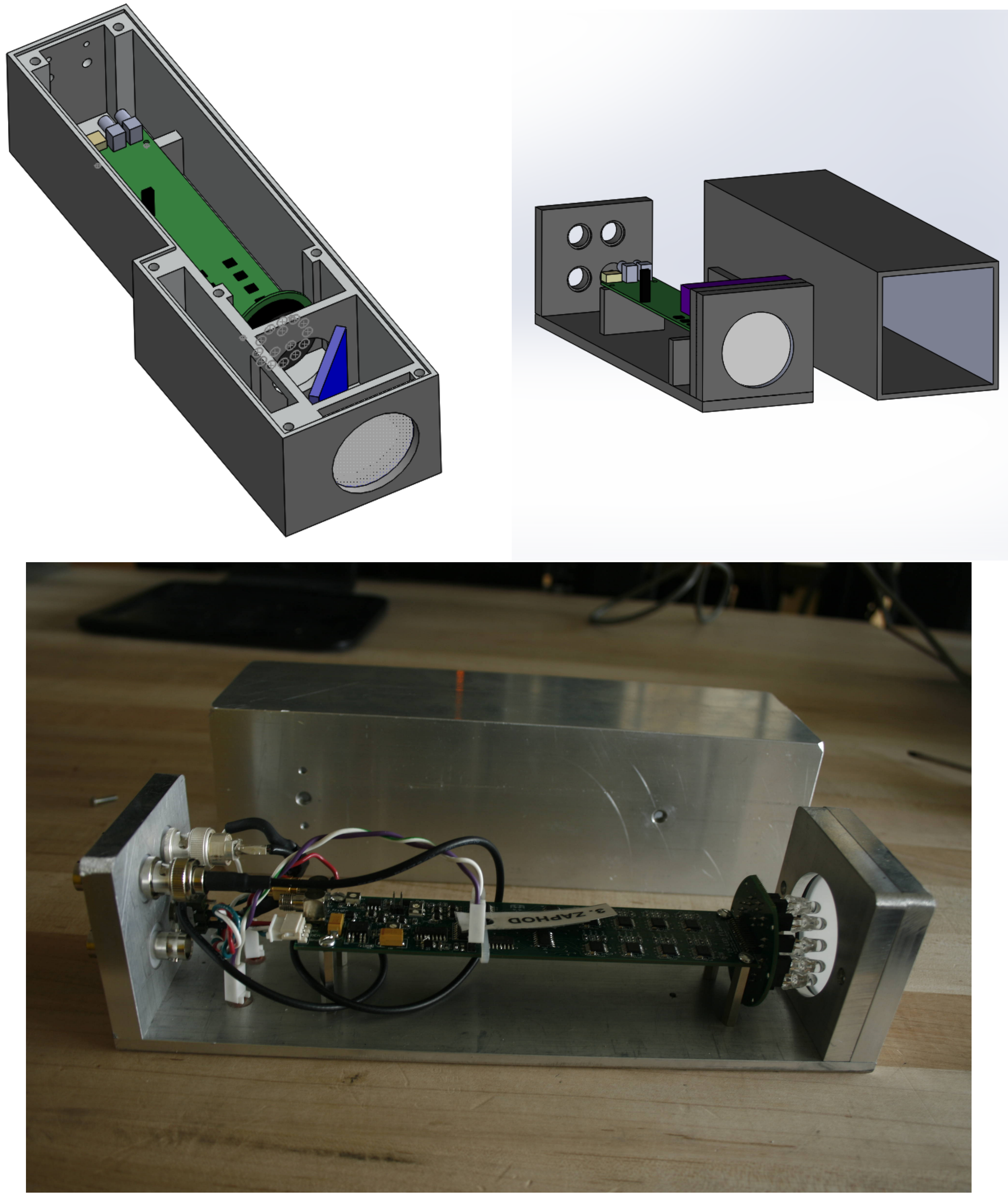

Figure 4.5: Comparison of the flasher casing initial design (top left), the final 3D model (top right) and the manufactured product (bottom).

4.4 Experimental Set-up

The laboratory set-up used to test the old and new flasher prototypes is illustrated in figure 4.6. Light from the flasher's NICHIA NSPU510CS Ultraviolet LEDs is sent to a block of organic, wavelength-shifting scintillator conveniently available, on the side of which a Hamamatsu R580 photomultiplier tube is optically coupled using silicone grease.

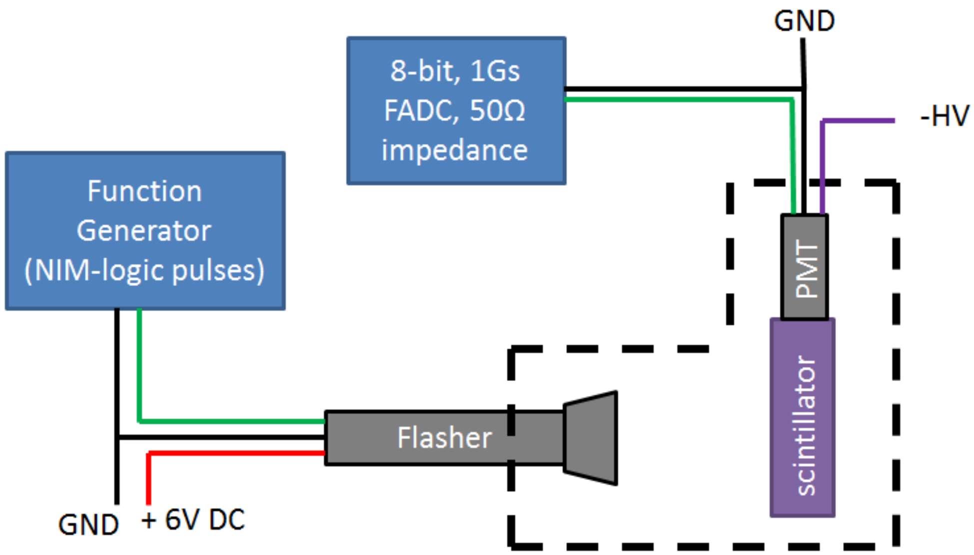

Figure 4.6: The experimental laboratory set-up used to test the performance of the flasher. Ultraviolet light from the flasher is sent to a block of organic, wavelength-shifting scintillator, on the side of which a photomultiplier tube is optically coupled using silicone grease. The electrical output of the PMT and external trigger signal are connected to an 8-bit FADC to digitize and acquire the pulses detected.

Wavelength shifters use fluorescence mechanisms to re-process the ultraviolet light of the LEDs: UV photons have enough energy to interact with the electrons of the large organic molecules making up the detector, and upon de-excitation, the molecules will emit photons at longer wavelengths. Since the fluorescence process is independent of the initial arrival direction of the exciting photon, the wavelength-shifted photons will be emitted isotropically, meaning that every side of the block will produce the same light flux. This will allow for a constant and uniform illumination of the PMT's photocathode, no matter the geometry of the incoming beam of light. Furthermore, one obtains a constant fraction of the flasher's light output, corresponding to the fraction of the total surface area covered by the photodetector; this way, one can sample all the light coming out of the flasher without saturating the photosensor.

The electrical output of the PMT is connected via a 50 Ω-impedance cable into a 1 Gsps (billion sample per second), 8-bit Acqiris DC270 FADC, along with an external trigger signal which sends a copy of the flasher trigger pulse into the readout-electronics. Since the FADC used is a multi-purpose instrument, its readout window and resolution parameters can be adjusted with more ease than the VERITAS FADC modules, for which specific settings have been encoded to optimize the telescopes' data acquisition. Therefore, during laboratory tests, the sensitivity of the FADC has been adapted to the specific needs of each performance test.

4.5 Data Analysis

Every test run made with a flasher is saved as an ASCII text file, and contains a certain number *nrun* of traces, each with length *nsamp*. Based on this raw data, and the header text file that comes with it, a series of C/C++ algorithms have been written to subtract the pedestal (which is the DC offset of a PMT trace), calculate the integrated charge, and from the statistics of each LED light level, compute the photostatistics gain of the photodetector using the knowledge from section 3.3.

4.5.1 Note on FADC units

FADCs digitize an analog pulse by sending copies of the latter through a network of logic comparators, illustrated in figure 4.7. At every clock signal of the FADC processor (which we will call a *time step*), every comparator will read the voltage of the signal pulse, and activate its HIGH-logic bit if the voltage read surpasses its reference value. The output of these comparators will be recorded into memory, thus yielding a digitized voltage measurement in

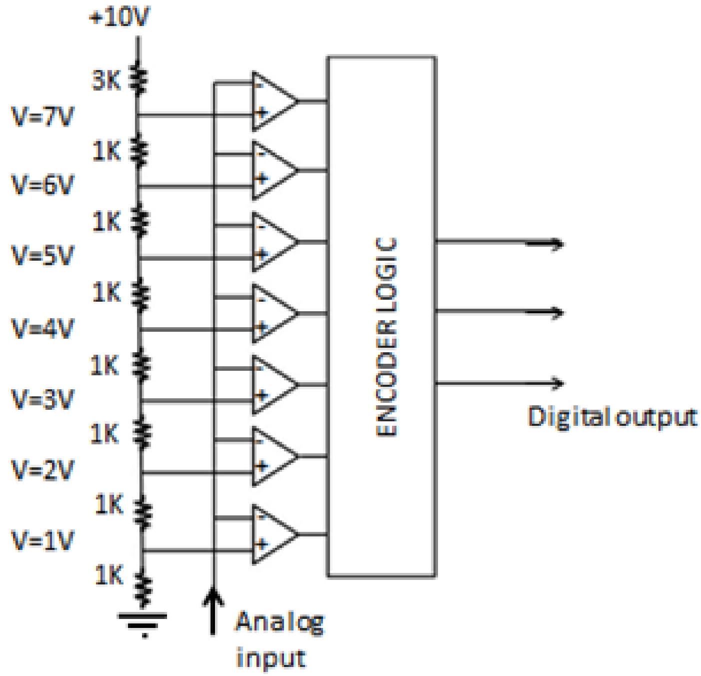

Figure 4.7: Diagram of an FADC circuit. At every clock signal of the processor, the PMT signal is copied and sent to an array of comparators, where its amplitude is compared to an array of thresholds. The output will be recorded in units of *digital counts (d.c.)*, representative of the number of FADC comparators that have triggered their HIGH logic.

units of *digital counts (d.c.)*, representative of the number of FADC comparators that have triggered their HIGH logic. Because of design limitations, the number of comparators that are included in the FADC is limited, meaning that the latter can only read a finite number of voltage values; hence, in the case of an 8-bit FADC like the one used in the lab, a total number of 255 voltage values can be read. While the 8-bit digitizer used in the laboratory produces results that are quoted in units of Volts, it is best to use units of d.c., because it is more representative of the measurements made by the instrument, and has the advantage of giving integer values.

The finite number of comparators is one of the limitations affecting the resolution of the FADC; along with the former, the latter also depends on the voltage range one wants to cover during the acquisition (a quantity we will refer to as the *fullscale* range). As an example, suppose we want to digitize a pulse signal that goes from 0 to 5V, with an FADC that has an 8-bit dynamic range: the resolution R of our digitized data will therefore be $R = (5 - 0)/255 = 0.196$ Volts per digital count (V/d.c.). The FADC used in the lab allows for seven different readout resolutions, each corresponding to a particular fullscale range configuration: from 50mV to 5V, in a 1,2,5 sequence [49].

Thus, much like a regular oscilloscope, the resolution and voltage scale of an FADC can be modified to optimize the readout window for the type of electronic signal detected. This wide range of parameters means however that the definition of a digital count is relative to the FADC configuration used for a particular test. To overcome this issue and compare, in absolute terms, acquisition runs done at different resolutions, a standard unit of digital count will be used to illustrate laboratory results in this thesis. That defintion is given by equation 16, and is based on the FADC's highest resolution.

$$y_{d.c} = \frac{y_V + V_{offset}}{R_{50mV}} \tag{16}$$

In the equation above, y_V is the signal of the FADC in Volts, V_{offset} is a DC pedestal that can be applied to the FADC to realign the readout window, and R_{50mv} is the maximum resolution of the digitizer. For the VERITAS flashers' data, the traces are already given in terms of FADC digital counts, standardized for a single fullscale range. The only correction that will need to be applied to the digital counts value will be the high-low gain ratio described in section 3.2.

4.5.2 Flasher data analysis procedure

Figure 4.8 illustrates the analysis steps taken to analyze both laboratory and on-site telescope data obtained with the LED flashers. For every flash of the instrument, a trace is recorded (A) by the FADC; that trace includes a non-zero pedestal, which is calculated by taking the mean value of the FADC traces recorder when no LEDs are flashing at the camera. After the mean pedestal value for the run has been calculated, it is subtracted from all data points in the trace; the latter is then "integrated" by summing the FADC samples over a particular time interval (indicated by the green region of figure 4.8 A). After all events of a flasher run have been processed, the charge values are then separated according to the light level they correspond to. This will generate a certain number of *integrated charge distribution* histograms, like the one illustrated in the next step of figure 4.8 (B).

Each charge distribution is fitted with a Gaussian function of parameters (A_o,μ_N,σ_N), where N corresponds to light pulses from 0,1,2...N LEDs. Those parameters (and their errors) become data points for the photostatistics analysis of the flasher run: one can plot each of them as a function of the flasher's LED light level (C1 and C2), and subsequently combine them in a σ_N^2 vs. $\mu_N - \mu_{ped}$ plot (D), where we can verify if a particular PMT is behaving as predicted by equation 15. In addition to the photostatistics analysis of a flasher run, the shape and intensity of the traces will be subject to special analyses in the following chapter, to ensure that the V2 flashers produce pulses that are similar to the ones produced by the original ones.

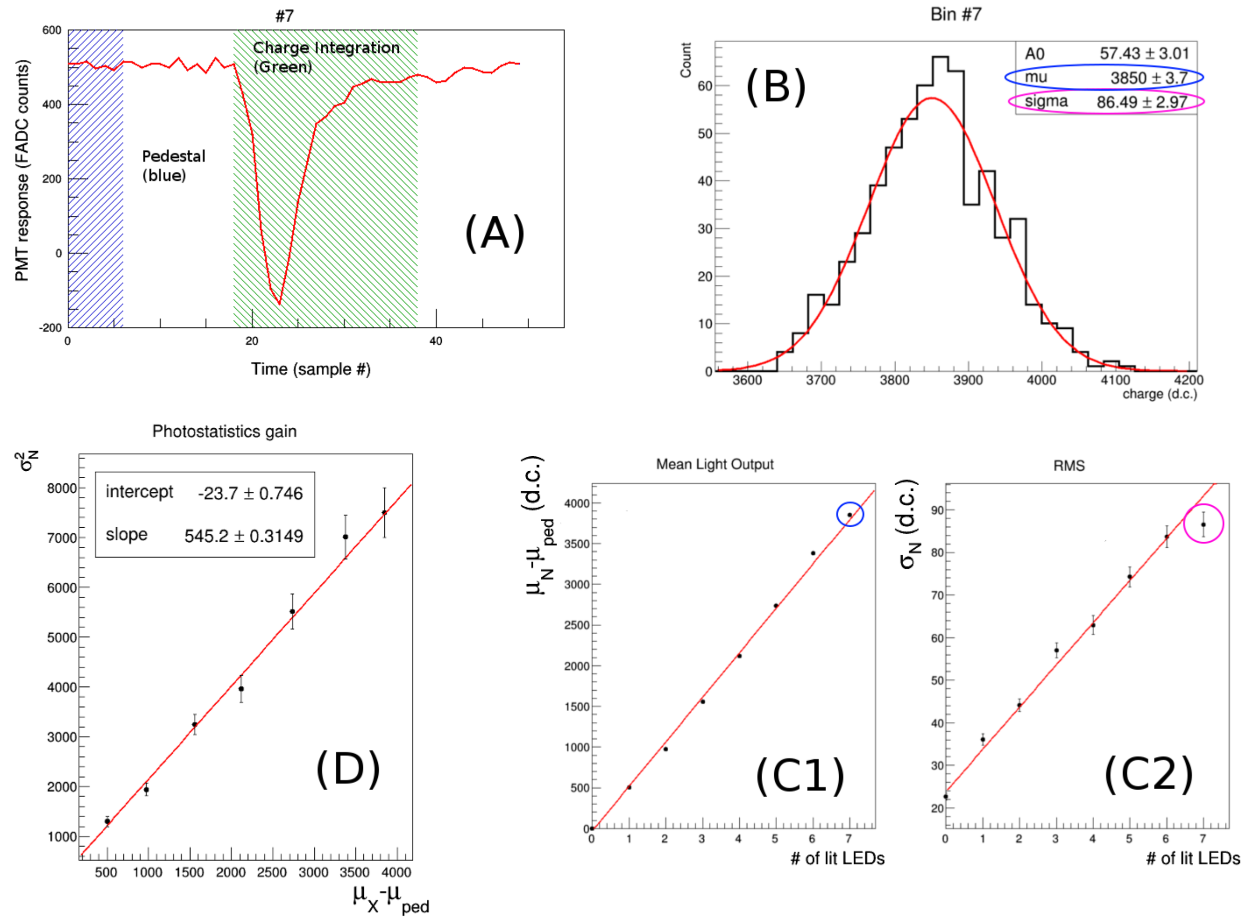

Figure 4.8: Analysis procedure followed when analyzing data from flasher runs. First, the mean pedestal of the FADC trace is calculated out of the first few time samples (blue region, figure A), or using the 0-LED light levels. The mean pedestal is then subtracted from the trace, which is subsequently summed over a particular range (corresponding to the green region of figure A). Next, the charge value obtained from the summation of every flasher event has its sign inverted, and is added to a histogram corresponding to the number of LEDs used during that event (B). The histogram is fit with a Gaussian function; the fitted parameter values are plotted as a function of the number of lit LEDs (C1,C2), and compared to one another in a σ_N^2 vs. $\mu_N - \mu_{ped}$. The slope of that last graph (D) yields the value of the photostatistics gain.

5 Results

Figures 5.1, 5.2 and 5.3 show the analysis results obtained using a first-generation (V1) spare flasher tested in the laboratory set-up described in section 4.4. The traces recorded on the FADC are first divided according to their corresponding light level (0, 1, 2...7 LEDs illuminated), and plotted as sequences (fig.5.1) to assess the shape of the light pulses. The green shaded regions on the plots indicate the region used for computing the event's integrated charge value. For every light level, the pedestal-subtracted charge value of each event is histogrammed (fig. 5.2). The distributions are subsequently fitted with Gaussians to extract their mean and standard deviation, which are then plotted in the photostatistics panel of figure 5.3.

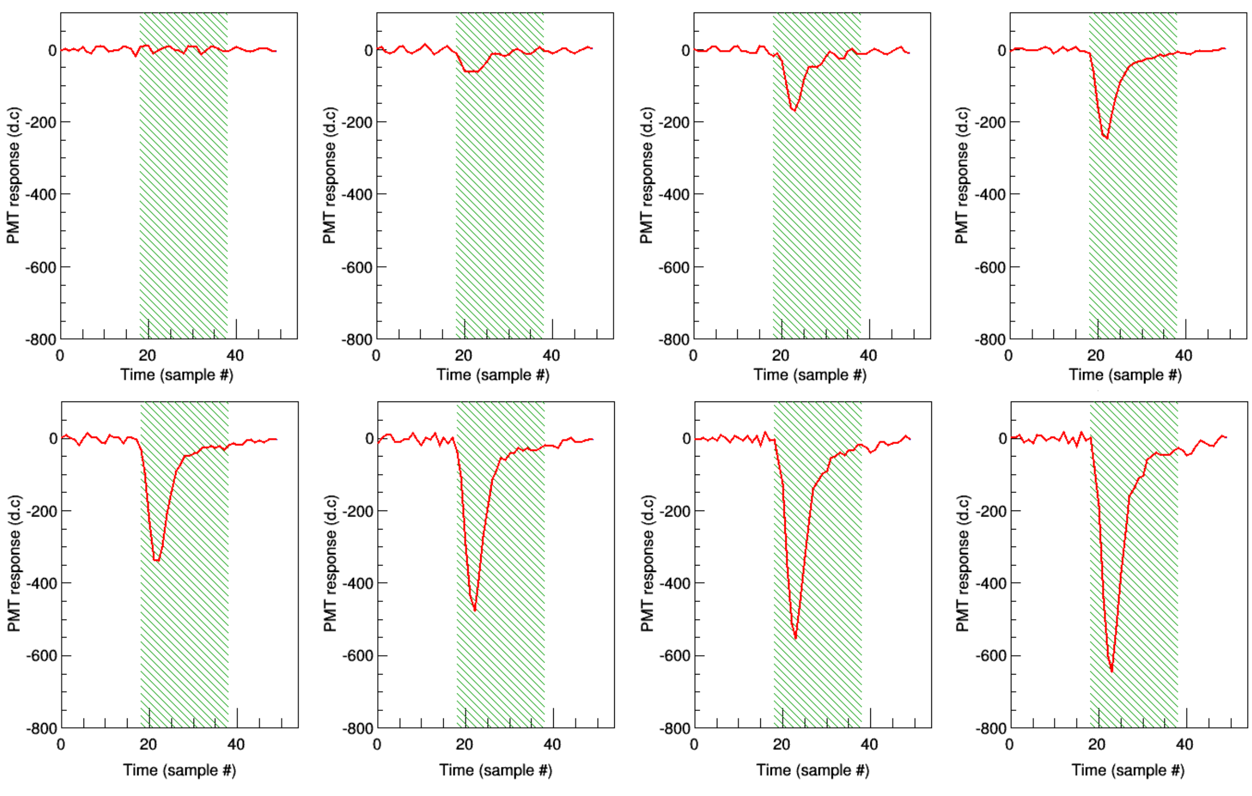

Figure 5.1: Example sequence of light pulses emitted by an old (V1) 7-LED flasher in the experimental set-up described in section 4.4. The Y-axis on these plots measures the intensity of the detected pulse in d.c., while the X-axis is given in units of time steps: one VERITAS time step is equivalent to 2 ns. The green region corresponds to the charge integration window.

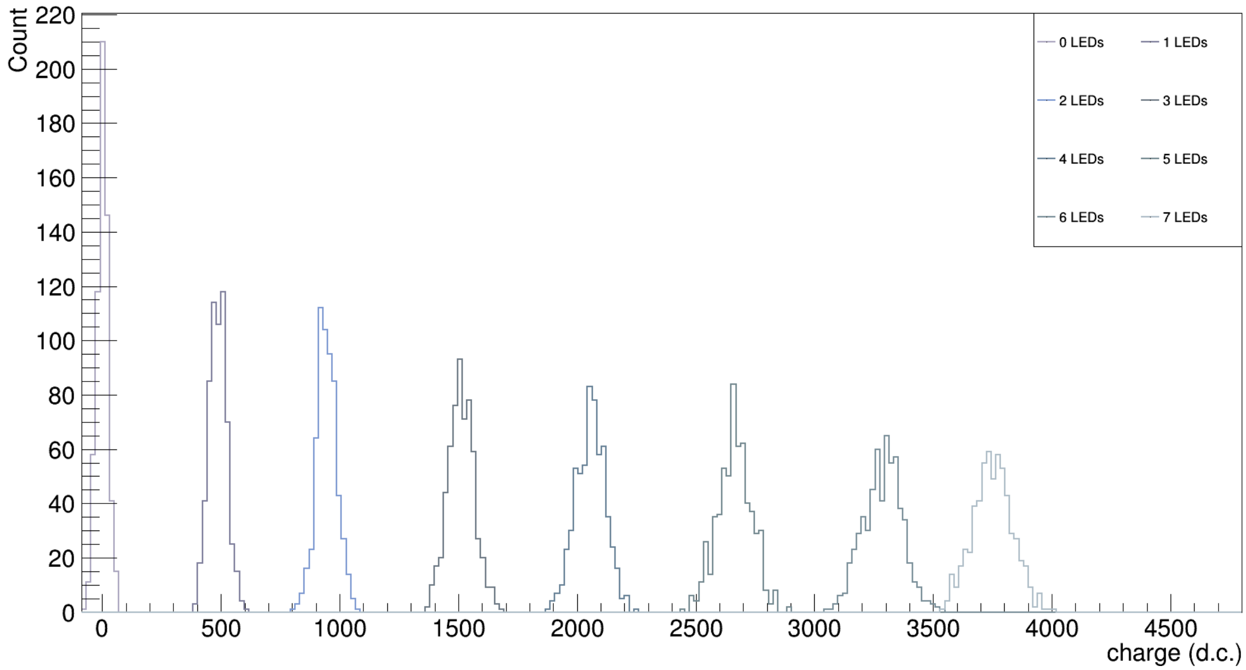

Figure 5.2: Superimposed histograms of the integrated charge measured from the light sequences shown in figure 5.1.

One of the objectives of these laboratory tests was to characterize the shape and intensity of the pulses produced by the 15-LED flasher, to ensure that the new instrument still emitted stable Cherenkov-like pulses. The other objective was to compare the photostatistics response of the V1 and V2 flashers, to make sure that the assumptions made about the behaviour of the V1 flasher could be applied to the V2 intrument as well. Meanwhile, the objective of the on-site testing of the V2 flasher was to ensure that the tuning adjustments made on the brightness of the light pulses allowed for an adequate coverage of the PMT response range in both high and low-gain mode. Section 5.1 presents the results of the laboratory characterization tests, while section 5.2 presents a comparison of the performances of both types of flashers, once installed on the VERITAS telescopes.

5.1 Laboratory characterization

The response of the new flasher was tested in the standard laboratory set-up, and compared with a control measurement from a V1 spare flasher in the same configuration. Figure 5.4 shows a typical sequence of light pulses emitted by the new flasher, figure 5.5 shows the

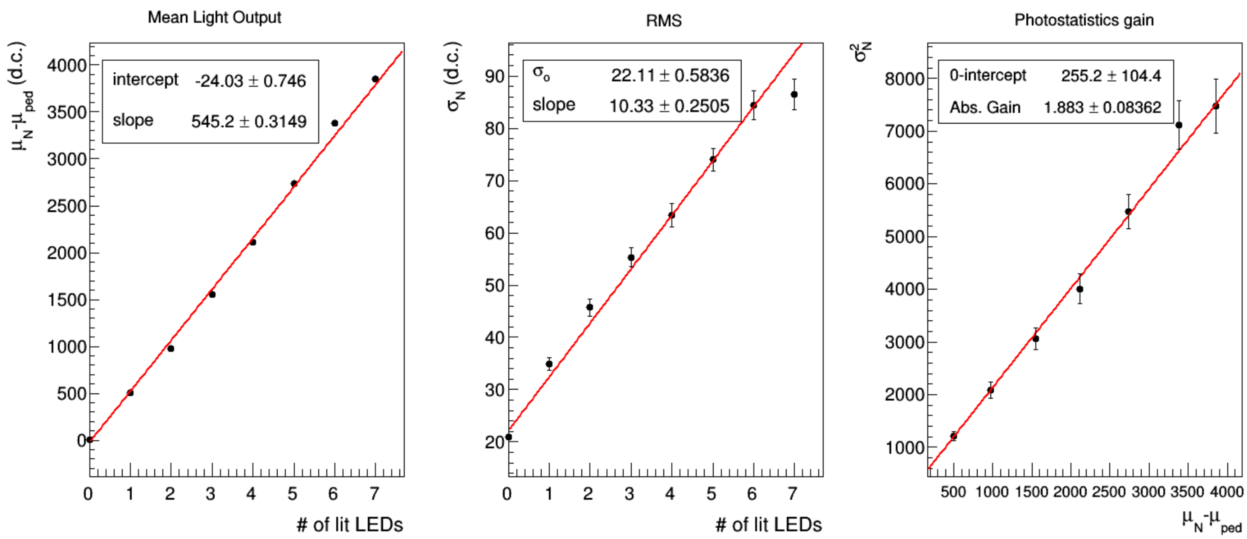

Figure 5.3: Photostatistics of the same V1 flasher test run, showing the behaviour of the first and second moment of the test runs' statistical distributions, as well as the photostatistics gain relation.

superimposed histograms of the integrated charge calculated for every light level, and figure 5.6 presents the photostatistics analysis of the laboratory run.

The initial tests have shown that the new flasher emitted pulses of stable intensities, such that the measured integrated charge distributions and associated photostatistics appeared to be normal. However, the new flasher produced light pulses which were much brighter than the ones produced by the previous instrument. Figure 5.7 illustrates this intensity increase, by placing on a same logarithmic plot the mean integrated charge of light levels from both flashers. In light of the requirements established earlier, these first results were unsatisfactory, mainly because no light levels covered the light intensity range corresponding to pulses 1, 2, and 3 of the V1 flasher: this would mean that no pulse would be able to cover the high-gain mode of the camera.

Alongside problems with the intensity of the pulses, a closer look at their shape has shown that they were much wider than their V1 counterparts (see figure 5.8), by about 10 ns. This problem meant that the pulses coming out of the flasher would not closely resemble

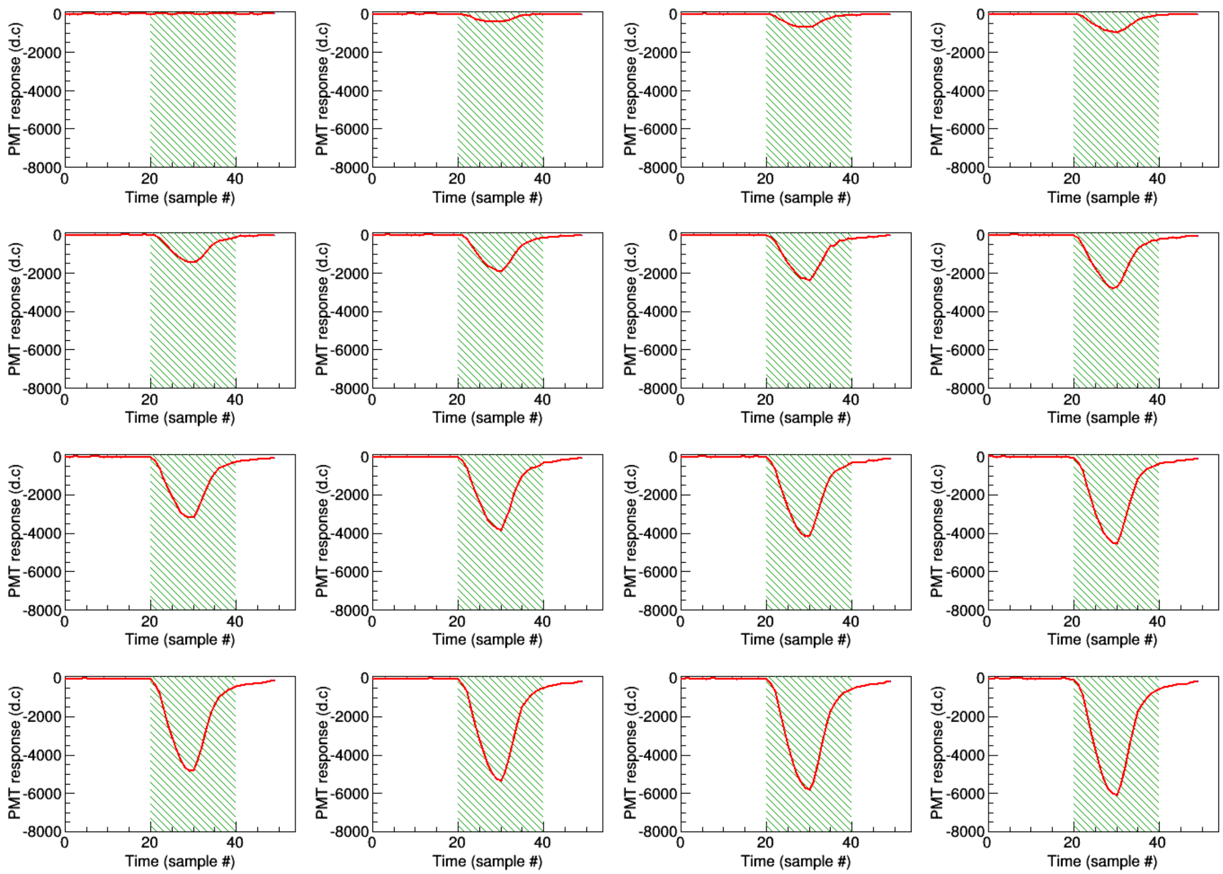

Figure 5.4: LED light pulse sequence from the new flasher, in its initial configuration. The Y-axis and X-axis labels are the same as those of figure 5.1.

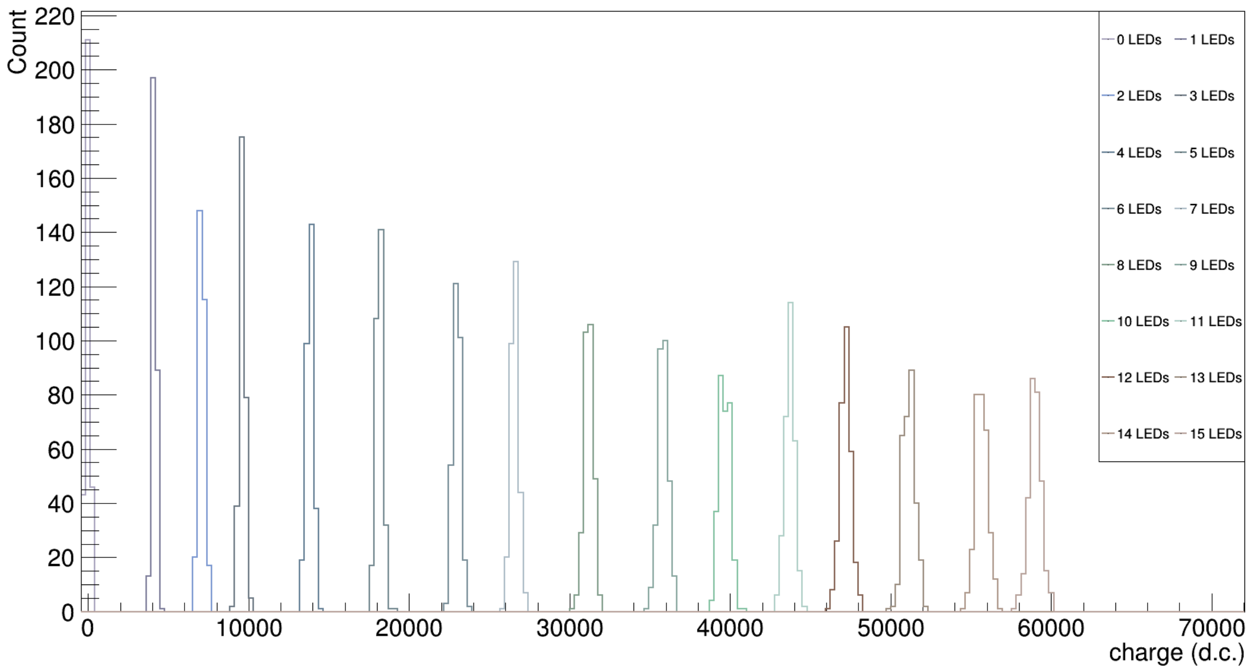

Figure 5.5: Superimposed charge histograms of the new flasher.

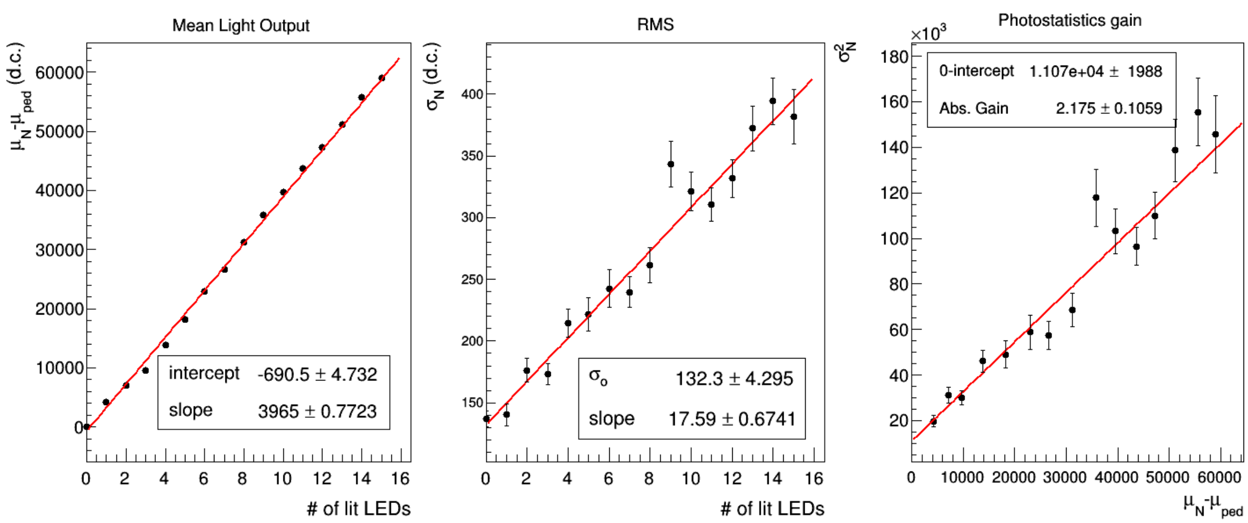

Figure 5.6: Photostatistics of the initial laboratory test of the new flasher. The first two moments of the integrated charge statistical distributions (the mean and RMS plots) behave according to Poissonian statistics, which shows that the light output of the new flasher is stable. Considering the significant figures of the gain slope fit on the right-hand plot, one finds that the absolute gain of the R580 is measured to be within the uncertainty of the measurement made with the old flasher in figure 5.3, proving once more that the instrument works well.

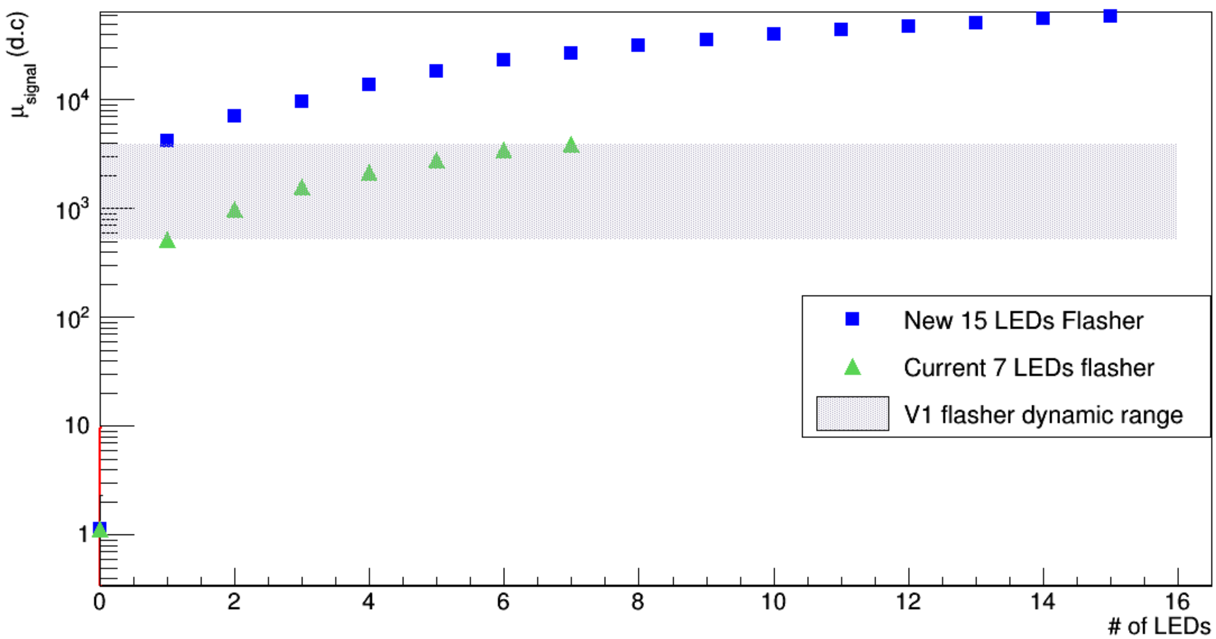

Figure 5.7: Comparison of the mean intensity of the light pulses detected from both V1 and V2 flashers. The shaded area corresponds to the light intensity range of the V1 flasher. The first three (non-zero) data points from of the latter roughly correspond to an illumination regime that would keep the VERITAS pixel in high-gain mode, while data points 4 to 7 would trigger the low-gain switch of the electronics.

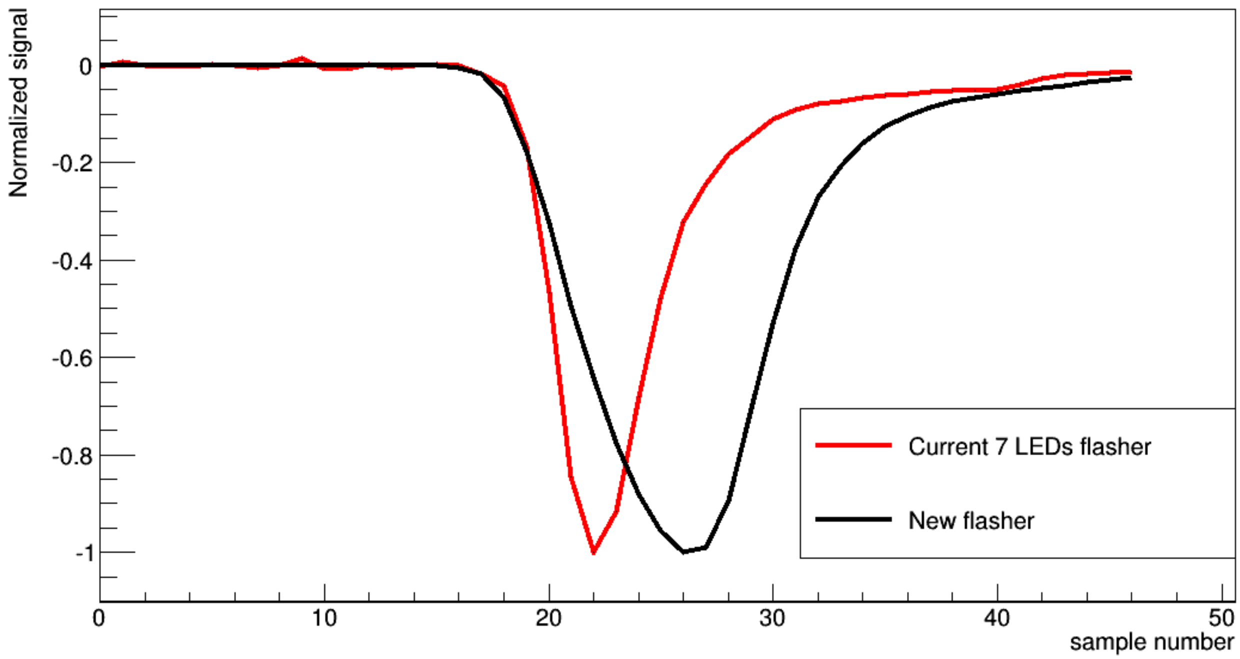

Figure 5.8: Normalized average pulses of the 7-LED light levels for both the old and new flashers. In its original configuration, the new flasher produced pulses that were too broad to fit into the VERITAS FADC readout window.

the shape of true Cherenkov pulses, which is problematic for the calibration measurements. It also meant that the FADC integration window of 32 ns was too small for the new pulses, which would have created further problems with the gain measurement.

To fix both those issues (lack of statistics in the high-gain mode and broad pulses), three modifications were made to the flasher's circuit board. First, the resistors regulating the current flow through the LEDs (the red section of the flasher electronics diagram illustated in figure 3.4) were changed for components with higher resistance values. Second, two different sets of resistor values were introduced, to produce a flasher that would have two intensity ramps: one for the high-gain mode, where the first four LEDs would produce pulses with a small number of photons, and another for the low-gain mode, where the last LEDs produced a higher number of photons per light level. Third, adjustments were made to the R17 potentiometer to narrow the time width of the pulses produced, thus reverting to a typical 10 ns value. Results from the laboratory test conducted with this modified flasher configuration are shown in figures 5.9, 5.10 and 5.11.

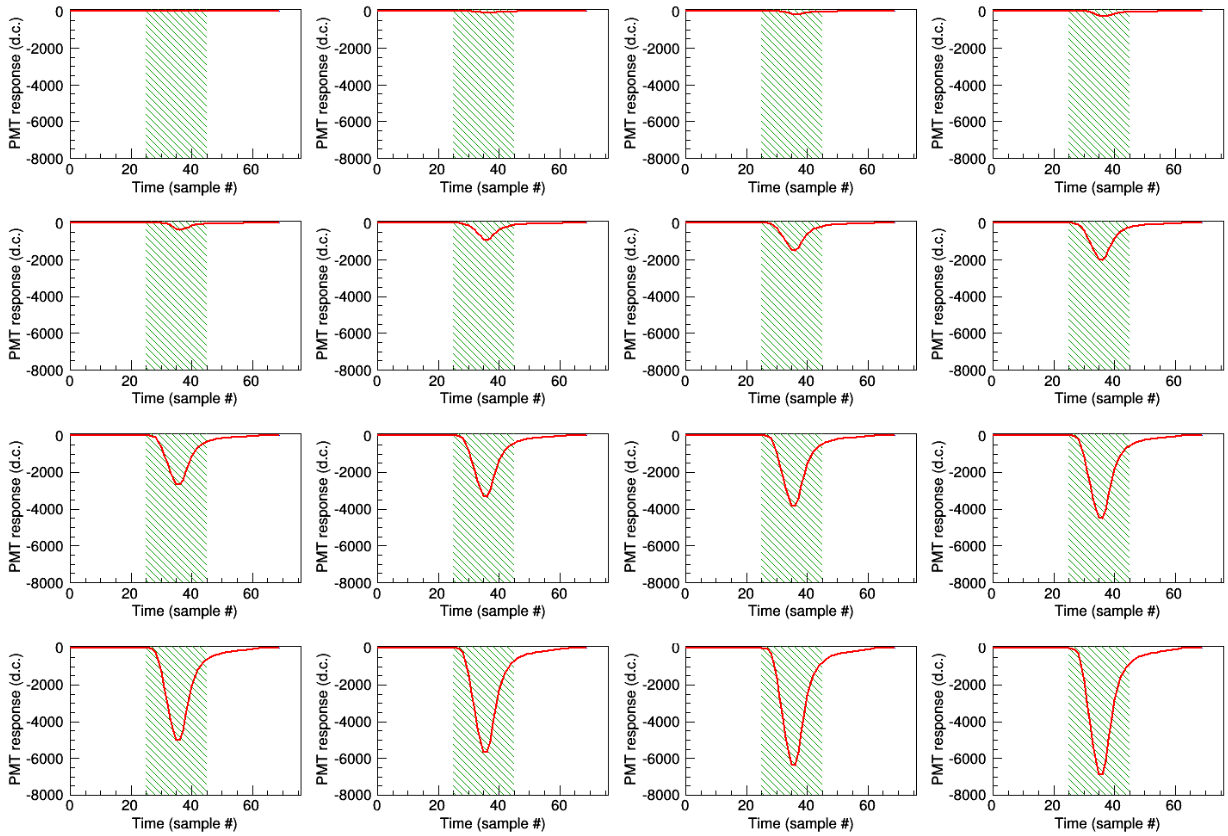

Figure 5.9: Shape and intensity of the average pulses produced by the "two-ramp" flasher. Two different sets of resistor values were soldered on the flasher circuit: one for the high-gain mode, where the first four LEDs produce pulses with a small number of photons, and another for the low-gain mode, where the last LEDs yield a higher number of photons per light level. Additional adjustments on the R17 potentiometer have also reduced the width of the pulses.

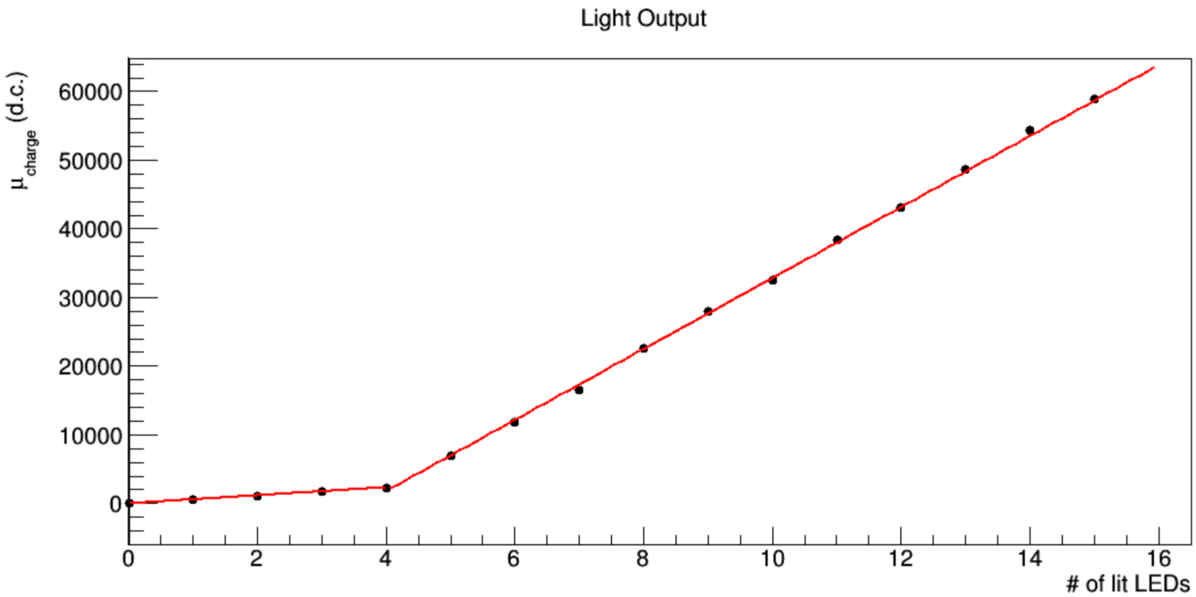

Figure 5.10: Mean intensity of the pulses produced by the "two-ramp" flasher configuration. The first four LEDs have resistors with higher values than the other eleven; this reduces the current intensity flowing through the LEDs, thus reducing the intensity of the light produced per lit LED.

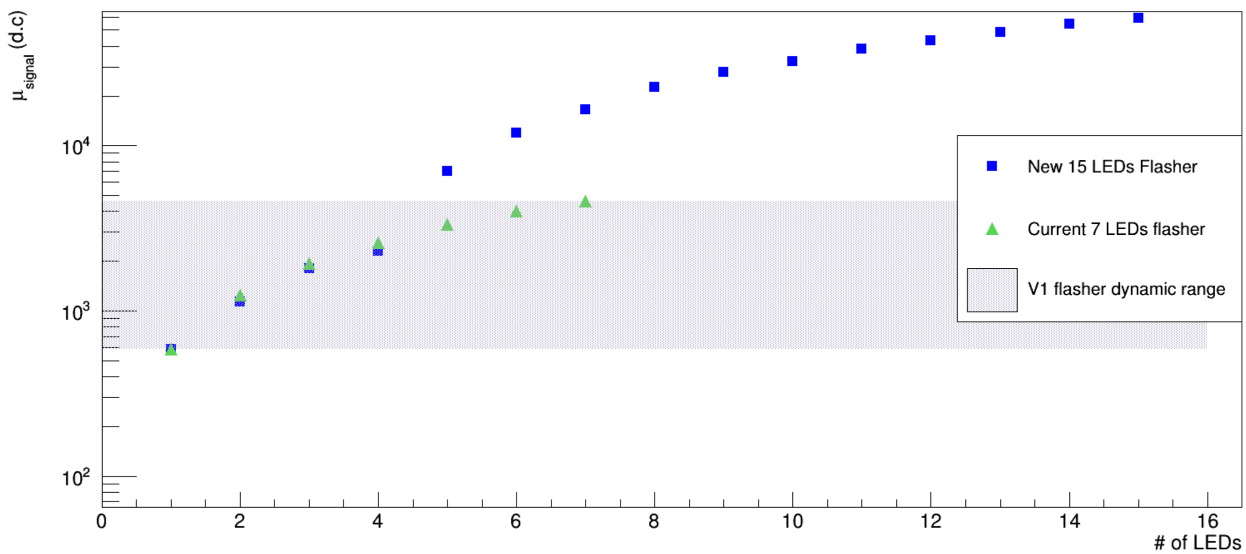

Figure 5.11: Comparison of the mean pulse intensity with that of a V1 flasher. This time, at least four LEDs were emitting light in the same intensity range as the old flasher, ensuring that the instrument will at least be able to mimic the performances of the old flasher in the high-gain mode while probing a larger portion of the low-gain response range.

Unfortunately, the dual-intensity ramp configuration became the source of a new problem which can be seen in figure 5.12. In this plot, the shape of a normalized 1-LED pulse is compared with the shape of a normalized 15-LED pulse. One can see that the latter is wider than the former: this is due to the fact that for a given R17 potentiometer settings, LEDs driven by a circuit with lower-value resistor will produce wider pulses than the LEDs driven by higher ones. Because of this, the dual-ramp configuration was deemed unsuitable for normal flasher operations, as it introduced a variable flasher pulse shape that is not taken into account in the modeling of the PMT's response.

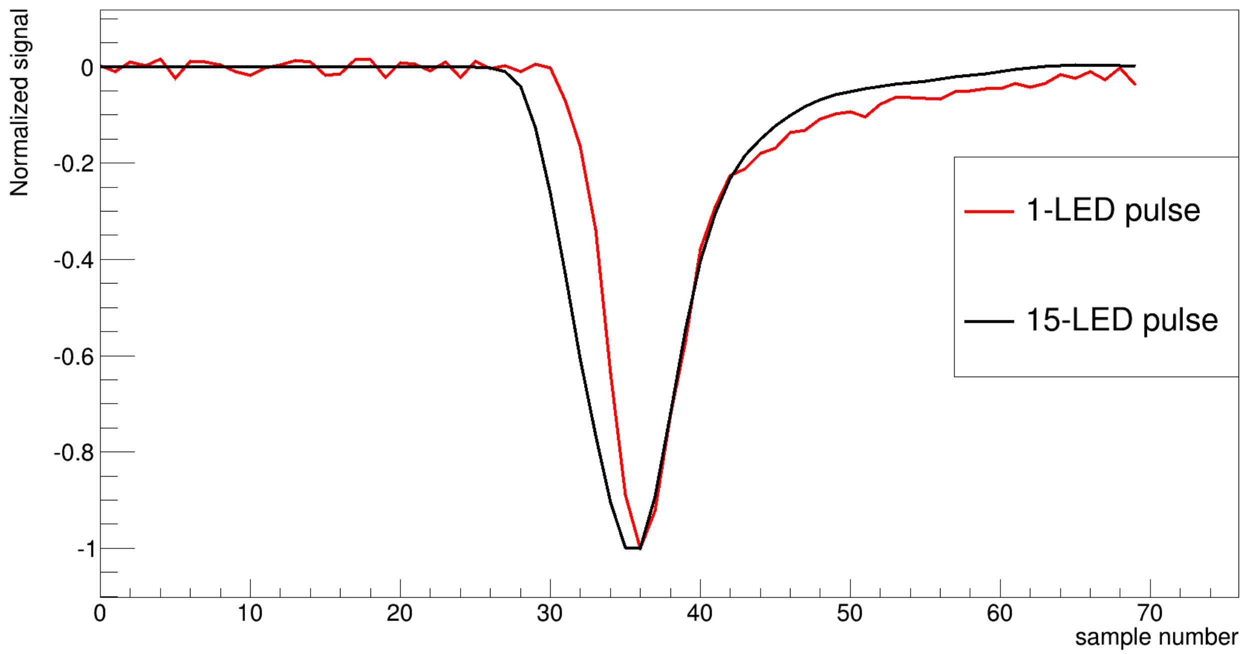

Figure 5.12: Normalized average pulses of the 1-LED and 15-LED light levels, showing the change in shape of the signal for different resistor values. This adds an unwanted complexity to the flasher's response.

Finally, the resistors were changed back to a single-ramp system, but this time, the pulse intensity was reduced to match the ramp of the V1 flashers. Figures 5.13, 5.14 and 5.15 show the result of the final laboratory test performed on the new flashers, prior to their installation on the telescopes of VERITAS. The results obtained in the lab have shown that they now produce pulses that have the correct temporal shape, and the correct intensity range to cover both the high and low-gain mode of the VERITAS cameras.

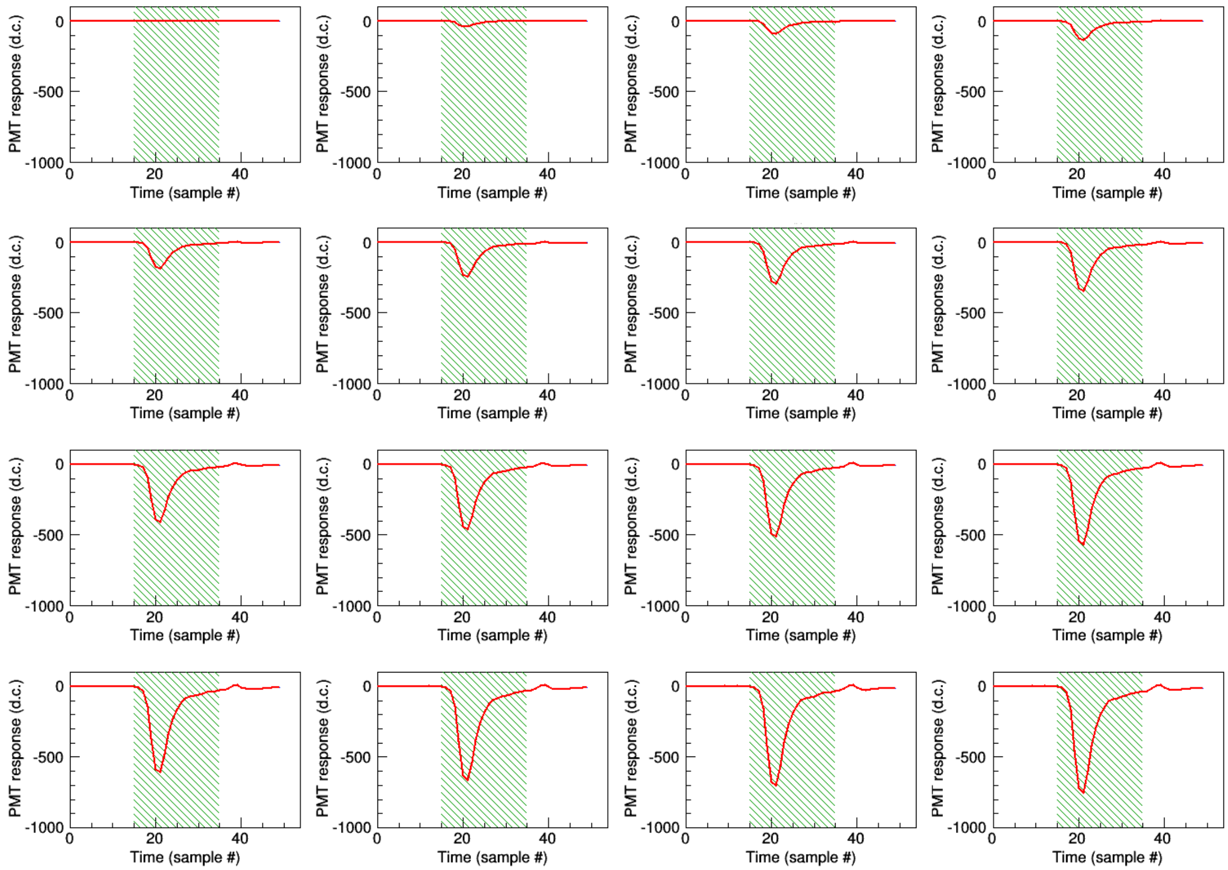

Figure 5.13: Average LED light pulse sequence from the final tests made on one of the final flasher instrument.

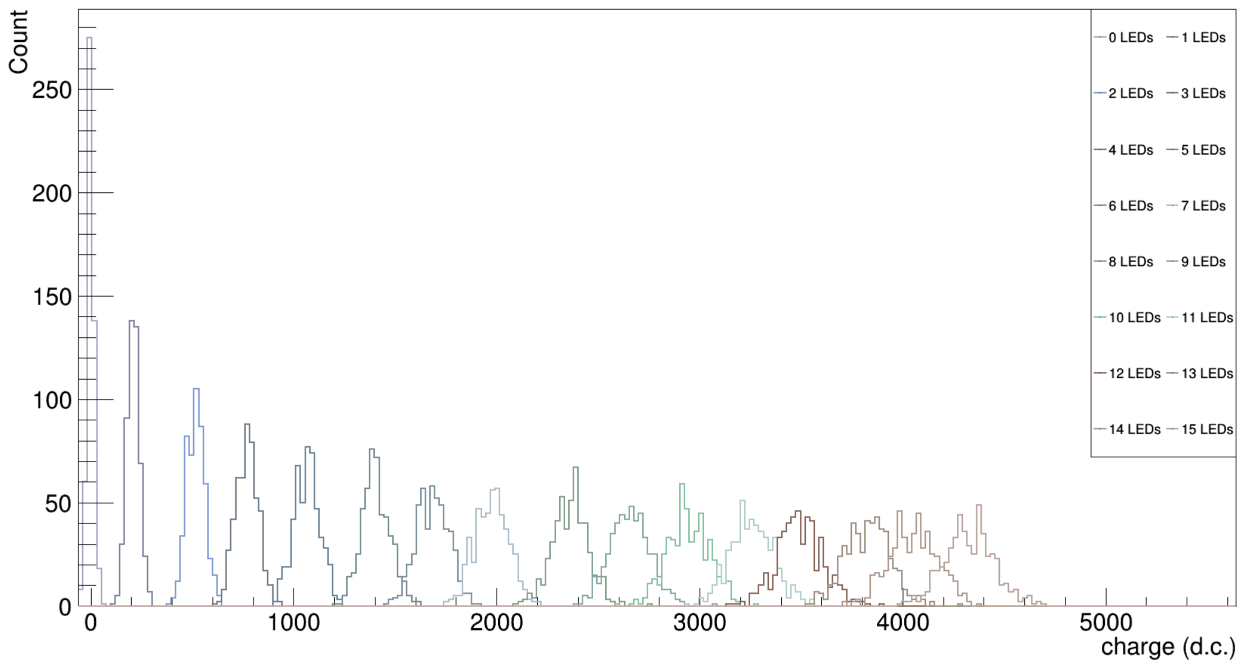

Figure 5.14: Superimposed charge histogram of the final calibration run on the finished flasher instrument. The more noisy appearance of the histograms compared to 5.5 is merely due to the R580 photomultiplier being positioned further away from the flasher than in run 0117. In fact, figure 5.15 show that the flasher behaves as expected.

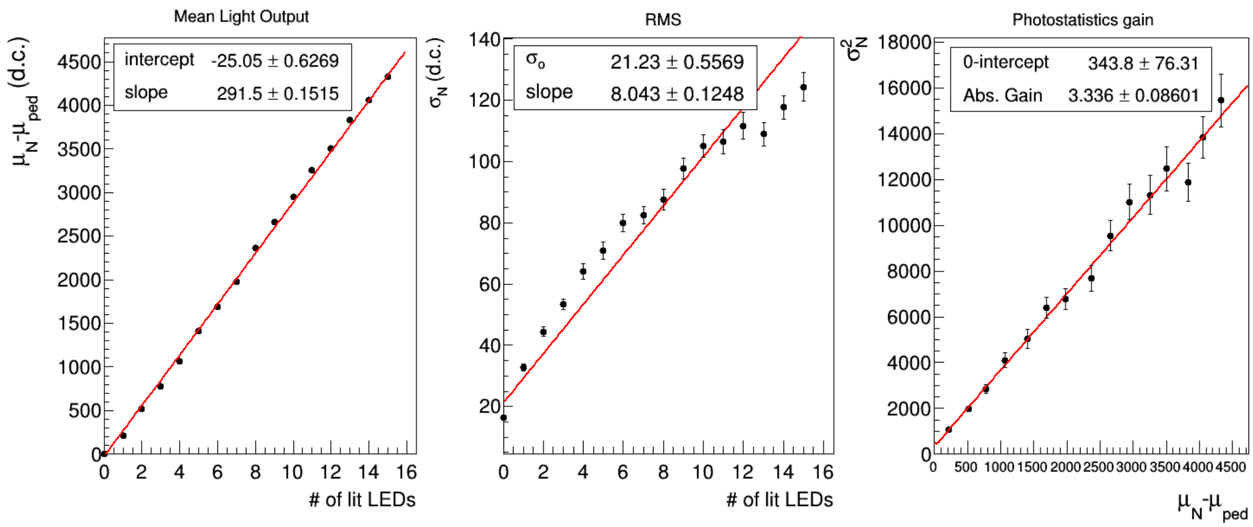

Figure 5.15: Photostatistics of the final flasher configuration, showing the linearity of the LED pulse intensities, and an RMS that behaves like a normal Poissonian process.

5.2 Performances of the new flashers on the VERITAS cameras

To evaluate the performances of the new flashers on the telescopes, data from two runs were compared: one using the old flashers as the calibration instrument (run 81414), and another with the new instruments installed (run 83093). Figures 5.16, 5.17 and 5.18 display the results from a single channel of telescope 4, in a manner that is similar to the one used for laboratory results: a typical sequence of PMT traces, a group of integrated charge histograms corresponding to particular numbers of LED being lit, and a photostatistics plot produced out of these charge histograms.

All the plots described here pertain to a single channel of a single VERITAS telescope (channel 4 of telescope 4); while this section does not present a comprehensive analysis of the new flashers' performances on all the camera (such an analysis being outside the scope of this thesis), it does provide a useful quick look analysis, to verify that the new instruments installed perform at least as well as the previous ones.

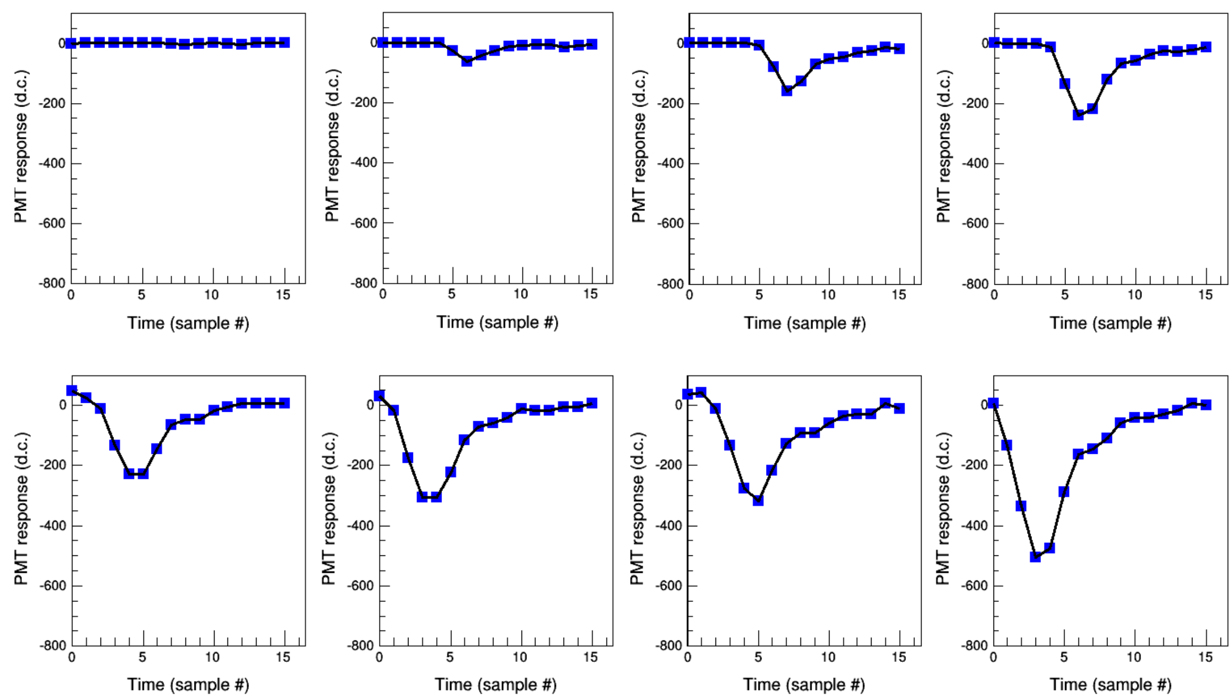

Figure 5.16: Typical sequence of pulses obtained during VERITAS flasher 81414, on channel 4 of telescope 4. Note that the line plotted in each trace links discrete data points together, and does not constitute a fit or smoothing of the pulse shape. The bottom plots correspond to pulses detected in low-gain mode, and have been multiplied by the approximate theoretical high-low gain ratio of 6.

5.3 Run 81414: old flashers

In order to better compare the low-gain and high-gain traces in figure 5.16, the former were multiplied by the theoretical high-low gain ratio of 6[11], to illustrate that they represent brighter events than the high-gain traces. That multiplication factor was not used in the subsequent integrated charge plots, as it was necessary in this case to verify that the experimental value of that ratio was well measured. A way to do this is to compare the absolute gain values obtained in the high and low-gain modes, on the right-hand plots of figure 5.18. These plots were created using the integrated charge histograms which did not correspond to an overlap between the high and low-gain modes, such as the 4-LEDs histogram of figure

[11]Recall that in section 3.2, it was explained that the high-gain amplifier multiplied the PMT pulse amplitude by 3, while the low-gain multiplied it by 0.5, hence the theoretical high-low gain ratio value of 6.0.

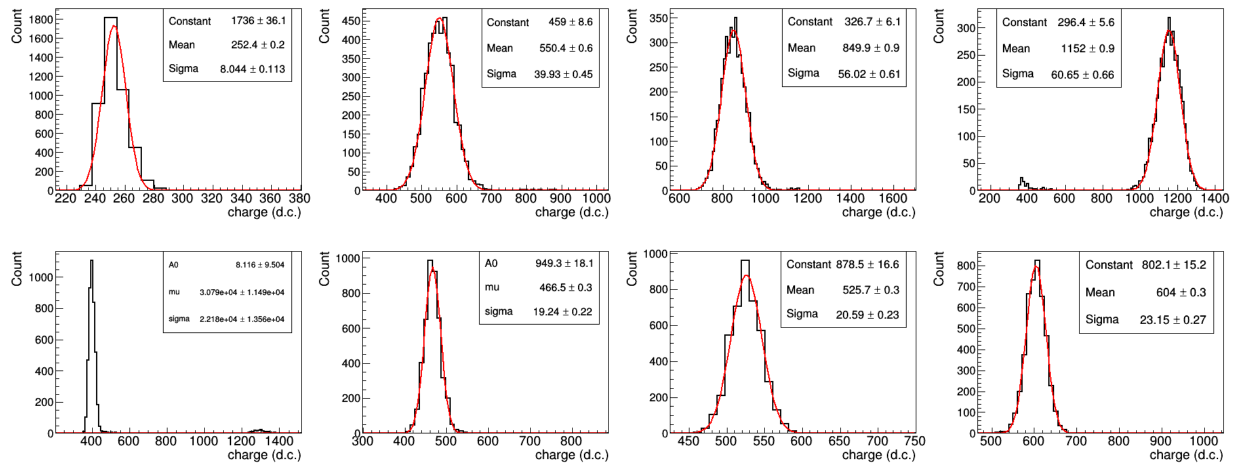

Figure 5.17: Integrated charge histograms for channel 4 of telescope T4, during calibration run 81414. As the intensity of the pulses increase, some flasher events start to be recorded in low-gain mode; the double-peak histogram of the 4-LEDs and 5-LEDs events show this transition from high to low-gain. Because these particular histograms are located at the boundary of the PMT's response switch into low-gain mode, they were not included in the photostatistics calculations.

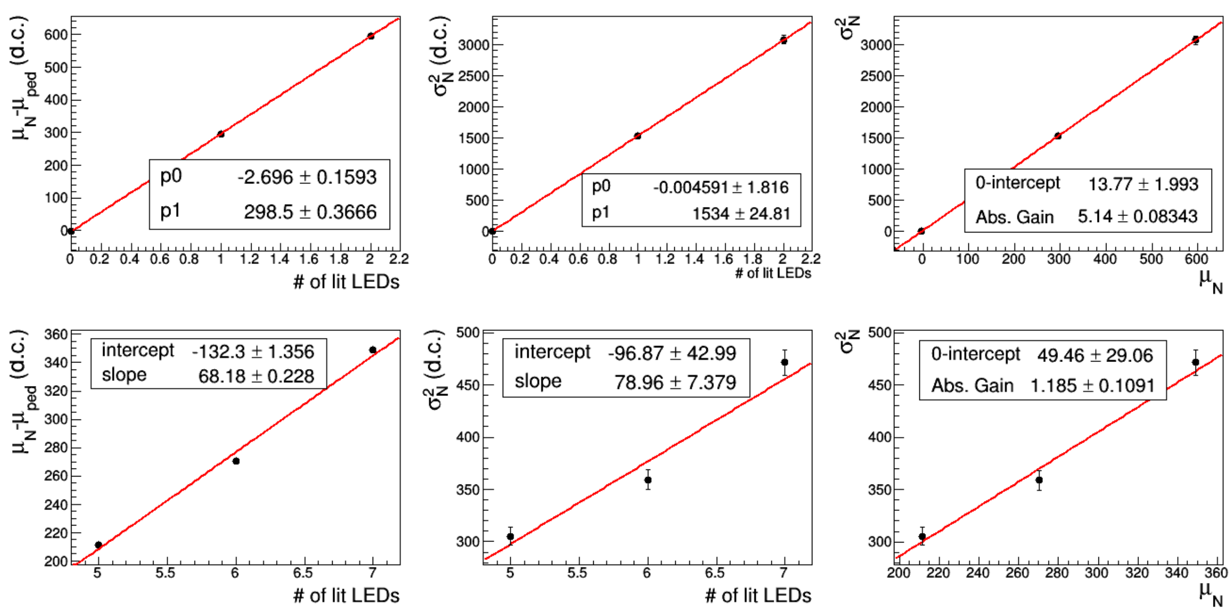

Figure 5.18: Photostatistics of the high-gain (top) and low-gain (bottom) modes of channel 4, telescope 4, during run 81414. The plots shown from left to right present the mean of the integrated charge histograms, the variance of the latter and the σ^2 vs. $\mu_N - \mu_{ped}$ gain curve.

5.17. The reason for this is that the RMS of the low-gain and high-gain histograms might not follow a perfect Poissonian behaviour, since the events recorded occurred in a boundary region of the PMT response range.

From the value of the gains fitted to the σ_N^2 vs. $\mu_N - \mu_{ped}$ plots, the experimental high-low gain ratio is measured to be 4.3, which is smaller than the expected theoretical value of 6.0. A reason for this discrepancy might be that for low-gain traces, the pedestal value calculated does not seem to bring the linear fit of the mean charge histograms exactly to zero. Since it is impossible to measure a "real" pedestal value in low-gain mode, the photostatistics in this response range may not behave exactly as predicted by the derivations made in Chapter 3: this is why, during normal high-low gain calibration procedures, the calculation of the high-low gain ratio is done using only data from the means of the charge histograms [37]. Therefore, the high-low gain values reported in this section should not be considered as an exact portrayal of the PMT's response: for the purpose of this thesis, they will serve as a comparison metric for the performance of the new flashers with respect to the old ones.

An interesting point to note, on the left-hand plots of figure 5.18, is that the ratio of the slopes of the mean integrated charge for both amplification mode closely mirrors the ratio of the photostatistics gain slopes (4.4 instead of 4.3). While these mean charge plots are still not the same ones used in the true calibration analysis (where the number of LEDs is replaced by the charge value of the monitor), they are more closely related to the latters then to the σ_N^2 vs. $\mu_N - \mu_{ped}$ plots, hinting that our analysis might not be that far off from the true experimental value of this channel's high-low gain ratio. A systematic analysis of the high-low gain ratio on all channels and all telescopes should be made to determine the validity of the hypotheses discussed above.

5.4 Run 83093 - New flashers

Figures 5.19, 5.20 and 5.21 present the plots generated using data from a recent calibration run taken with the new flashers. This run was taken on October 9th, 2016, following the

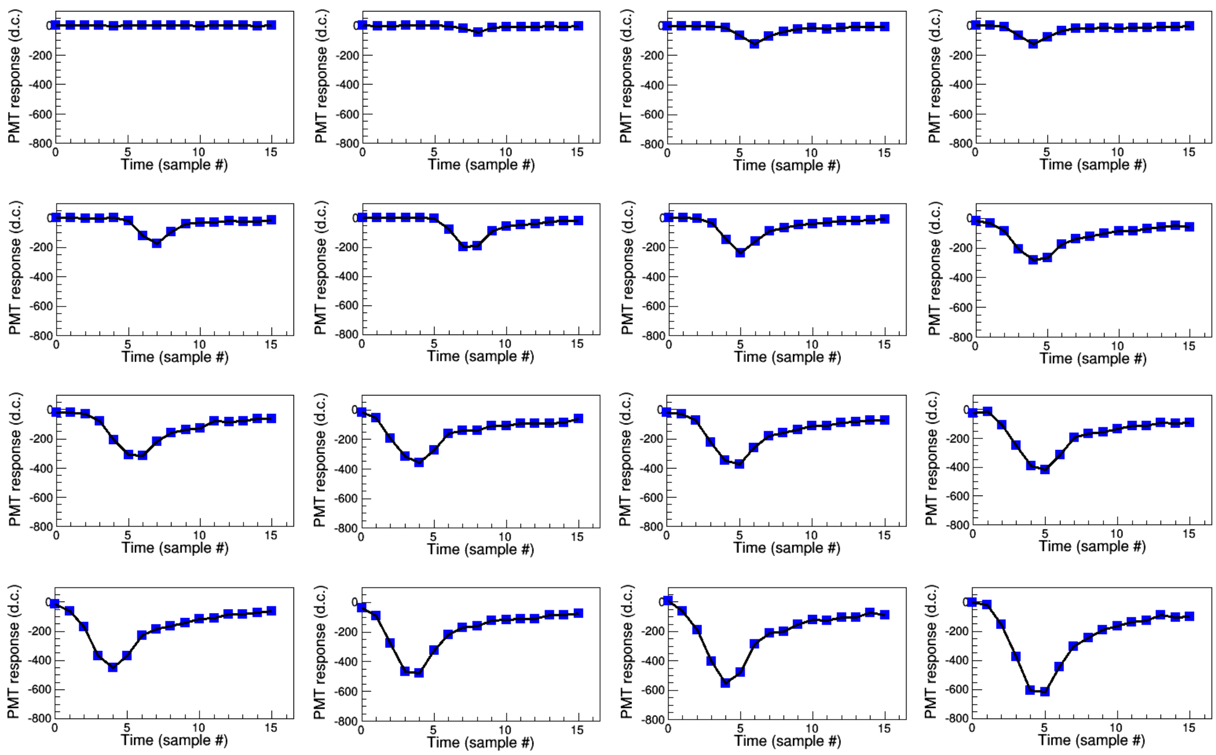

Figure 5.19: Pulse sequence from channel 4 of telescope 4, acquired during calibration run 83093. The new flashers were used as the calibration instrument for that run.

start of operations after the seasonal shutdown of the experiment in the summer. Because of the time gap between the two runs, the comparison of the two types of flashers might not be entirely straightfoward, since calibration procedures like flat-fielding might have modified the absolute gain of the analyzed channel in that period of time.

From the absolute gains calculated in the right-hand plots of figure 5.21, one finds that the high-low gain ratio obtained with the new flasher data is 4.2, which is consistent with the measurement obtain with the old flashers in run 81414. It is also possible to see on the same figure that the high-gain photostatistics plots of run 83093 behave as expected: even if certain values of mean integrated charge deviate from the linear fit (which is probably caused by the fact that LEDs have a certain tolerance in their manufacturing quality, and therefore may not all emit exactly the same amount of light), that deviation is mirrored in the variance of the charge distribution, and cancels out in the absolute photostatistics plot. Given these

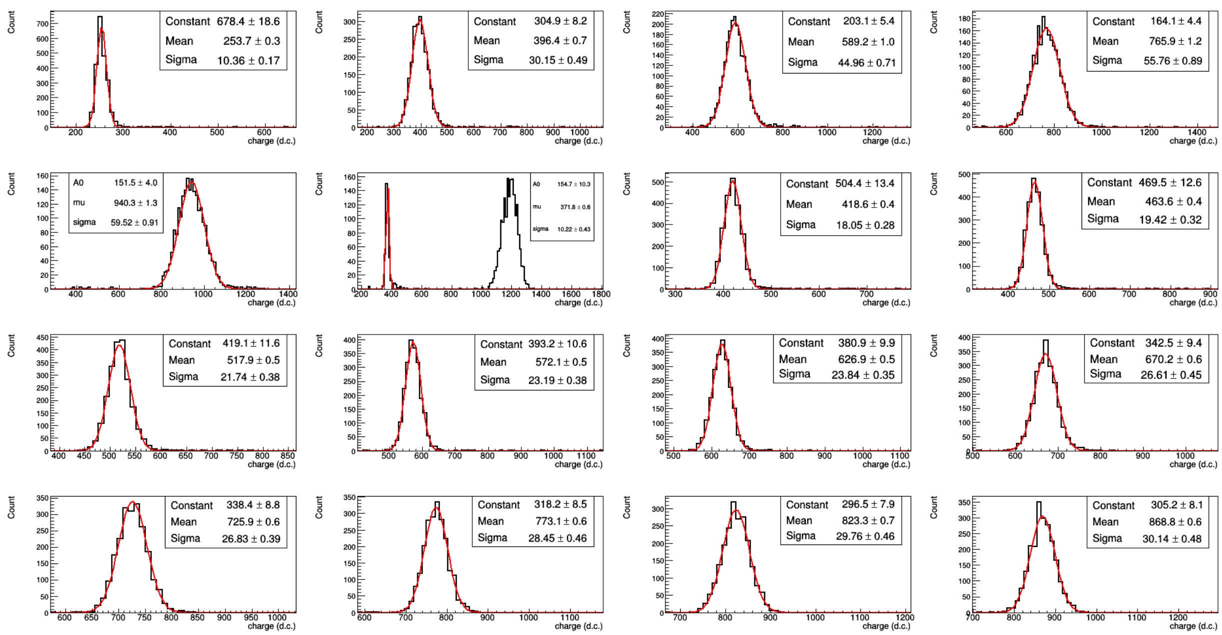

Figure 5.20: Integrated charge histograms for channel 4 of telescope T4, during calibration run 83093. In this channel, the 5-LEDs flasher pulse produced a double histogram, at the edge of the high-gain, low-gain switch region. For this reason, it was excluded from the photostatistics plots.

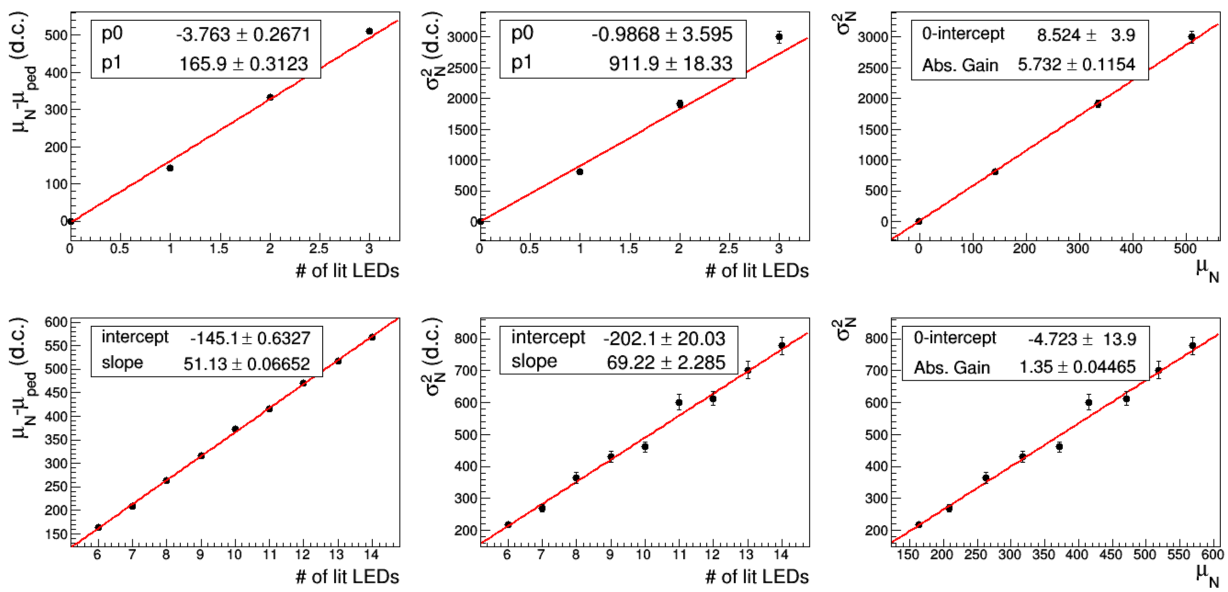

Figure 5.21: Photostatistics of the high and low-gain modes of channel 4, telescope 4, during run 83093. While the values of absolute gains measured are slightly different from the ones measure in figure 5.18, the high-low gain ratio calculated in the two plots is consistent with the uncertainties.

results, it is clear that the new flashers are performing as well as the old instruments.

5.5 High and low-gain mode coverage

A final point of comparison between the old and new flashers is their coverage of the PMT response range on every camera. Figure 5.22 shows the number of channels that switch into low-gain for every LED light level, on all four telescopes during run 81414. This plot underlines the problem of the lack of d.o.f. described in section 4.1: if we only use the V1 flasher LED pulses that are outside the high-to-low gain switch region, we are left with only 3-4 data points in our photostatistics plot, and even less (2-3) points in the low-gain mode: while this is fine to fit a line to the data, it is insufficient to investigate possible non-linearities in the PMT response.

Figure 5.23 shows how the new flashers address this problem: with twice as many LEDs, it is now possible to get 6-7 data points per gain mode, which will allow for a more refined analysis of the absolute photostatistics gain of the PMTs. Morover, given that the value of the LED driver circuit resistor can be changed, it might be possible to increase the probing range of the instrument further into the low-gain mode, while still retaining the necessary number of data points in the high-gain mode.

To conclude, the initial assessment of the new flashers' performances show that they are able to produce Cherenkov-like pulses similar to those of the current instrument. It also shows that the addition of new LEDs has increased the number of d.o.f. available to test non-linear functions that might better represent the PMT gain, both in high-gain and low-gain mode. In their current tuning state, the new flashers can probe a marginally larger range of the PMTs' response range; given the high number of data points obtained in the high-gain mode, there is still room to increase the light output of each LED to probe even deeper into the low-gain mode. To reach saturation however, one would have to significantly increase the flasher's brightness, which might not be possible without changing the width of the pulses, using the R17 potentiometer.

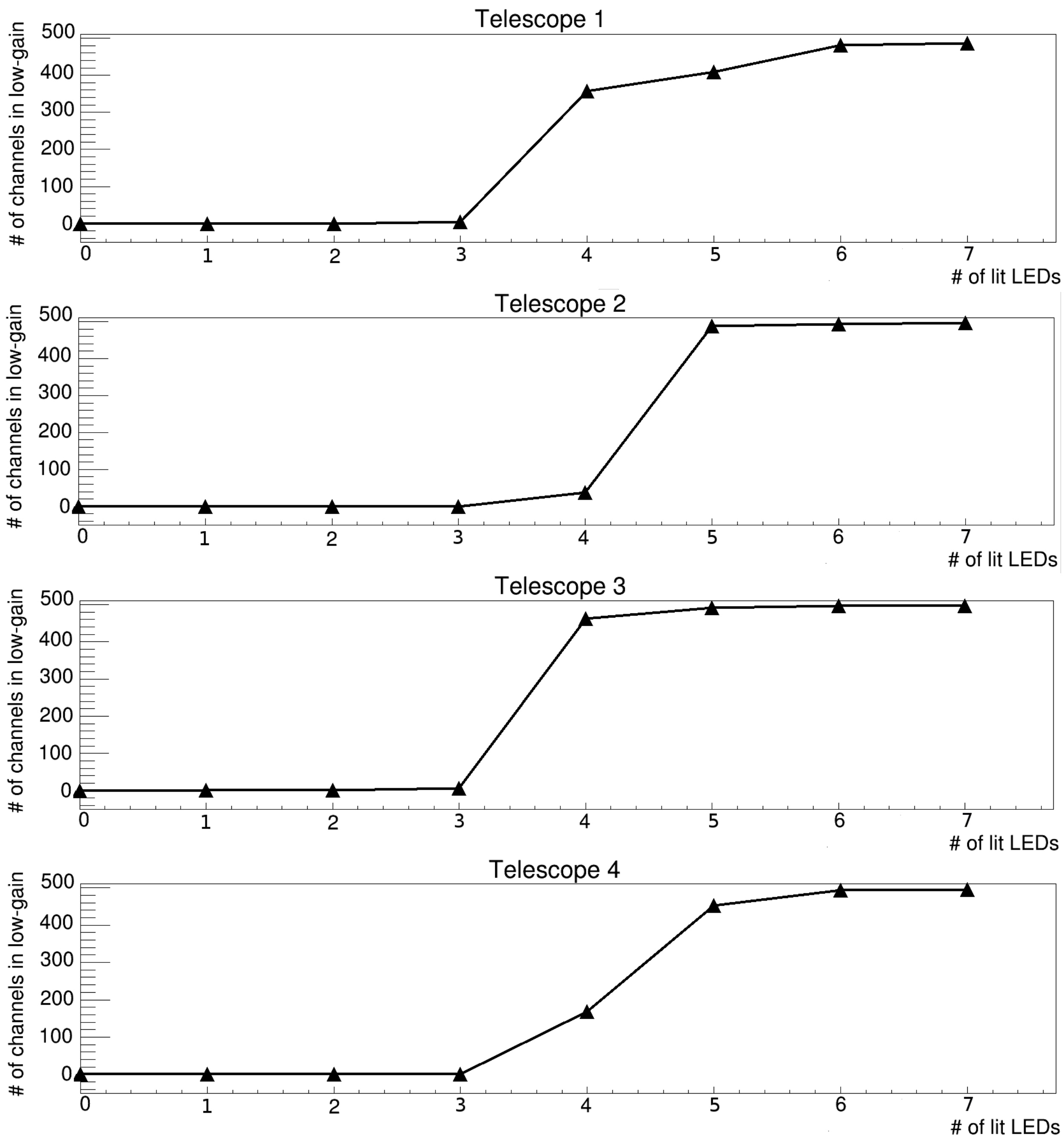

Figure 5.22: Proportion of channels that have switched into low-gain mode, for all telescopes, in run 81414.

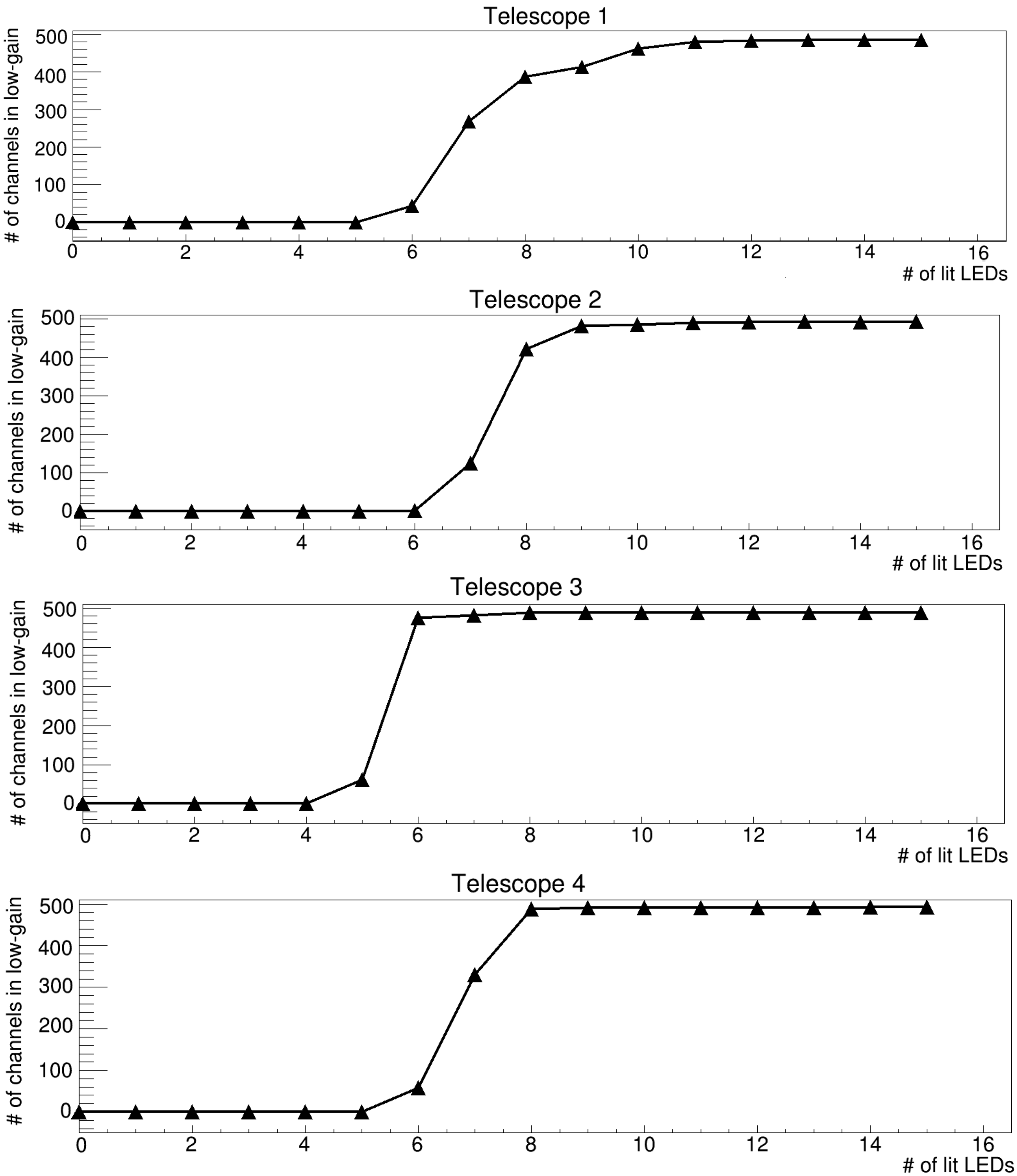

Figure 5.23: Proportion of channels that have switched into low-gain mode, for all telescopes, in run 83093. These plot show that the installation of the new flashers have improved the coverage of both high and low-gain on every telescopes.

6 The Flasher light monitor concept

6.1 Motivations

As was explained in chapter 3, the photostatistics approach to measuring the gain of the VERITAS pixels assumes that the intensity of the light pulses sent to the camera is constant for a given light level: in other words, we assume that the resolution parameter of the flasher B_f is negligible compared to the Poissonian fluctuations of the photon-photoelectron conversion process at the pixel photocathode. Fluctuations in the flasher light output can be corrected for with the use of an independent *monitor* that measures the absolute output of the flasher (and its variation over time). Currently, the monitor used on VERITAS is a statistical contruct made from the response of most of the 499 camera channels, which was described earlier in section 3.5.1. While this technique currently works well, the addition of a light sensor integrated into the flasher's design would be a simpler way to evaluate the absolute light output of the device.

Additionally, a problem that arises in flasher calibration measurements is the occurence of random pedestal triggers within the FADCs' data acquisition program. As part of the normal observing technique, the telescope array is instructed by the L3 server to forcefully acquire a trace at a rate of 3 Hz, independently of its air-shower trigger architecture. The acquisition of these special traces is necessary to monitor the NSB and its fluctuations over the course of an observing run, but it becomes a nuisance when the telescopes are operating in calibration mode: sporadically during a flasher run, pedestal triggers will keep the FADC electronics busy, rendering them momentarily unable to record the light pulses coming from a flasher event. The introduction of an onboard light monitor capable of clearly distinguishing between different flasher light levels would therefore allow one to tag every recorded FADC trace as a 0,1,2..N LED event, thereby keeping track of the pulses sent to and acquired by the cameras.

Motivated by the two previous observations, the design of an onboard light monitor was developed and tested in a laboratory set-up illustrated in figure 6.1: a UV-transmitting, quartz glass plate is positioned in front of the flasher LEDs, at an angle θ_i of 45° with respect to the direction of light emission. Because of the difference in the value of refractive indices at the air-glass interface, a small but constant fraction of the incident light will be reflected: that amount can be calculated using the Fresnel coefficients of reflection for parallel and perpendicular polarization, $r_{\parallel}$ and $r_{\perp}$, the angle of the transmitted light θ_t, and their relationship with the coefficient of transmission t. [50]

$$r_{\parallel} = \frac{\tan(\theta_i - \theta_t)}{\tan(\theta_i + \theta_t)} \tag{17}$$

$$r_{\perp} = -\frac{\sin(\theta_i - \theta_t)}{\sin(\theta_i + \theta_t)} \tag{18}$$

$$r^2 + t^2 \frac{n_2 \cos(\theta_t)}{n_1 \cos(\theta_i)} = 1 \tag{19}$$

In the case of fused silica glass, which has a refractive index of 1.48 around the peak emission wavelength of the LEDs (380 nm), $r_{\parallel}^2 = 0.76\%$ of parallel-polarization light is reflected, whereas $r_{\perp}^2 = 8.00\%$ of the perpendicular-polarization light is reflected. Since an LED does not emit polarized light, the total reflection coefficient $R^2 = |r^2|$ will therefore be half the quadratic sum of the Fresnel coefficients: $\frac{1}{2}(r_{\parallel}^2 + r_{\perp}^2) = 4.7$ %.

In the light monitor set-up, the reflected light from the glass plate is diverted into a scintillator block located on the side of the flasher, and a light sensor is optically coupled to it. Two types of sensors have been tested in the described configuration: a Hamamatsu R3998-02 photomultiplier tube, and a SensL Array-SB4 *Silicon Photomultiplier* (SiPM). The following sections present the results of the tests conducted in the laboratory on both sensors.

6.2 First Design: R3998-02 PMT

Figure 6.2 shows a photograph of the PMT tested in the light monitor configuration described above, while table 2 lists the main technical specifications of this hardware element.

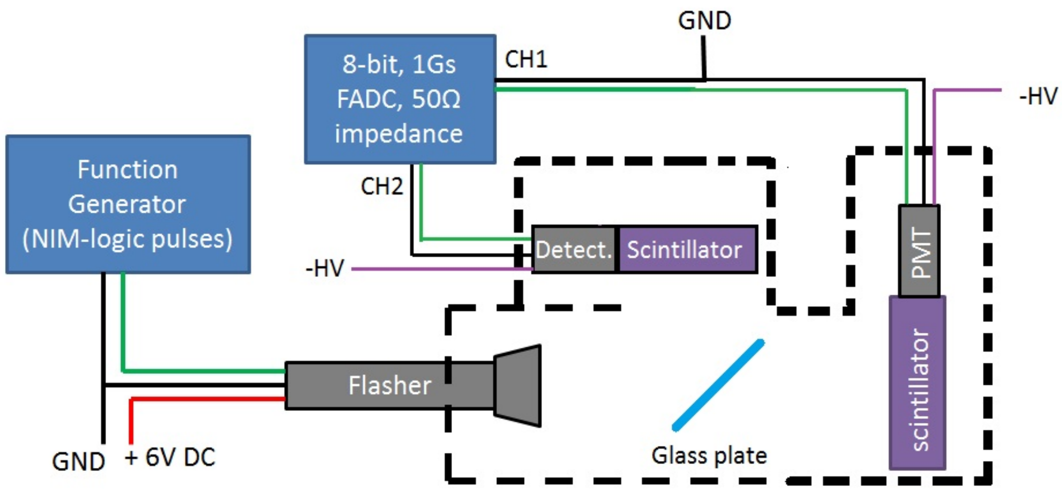

Figure 6.1: Schematic of the flasher light monitor concept: a quartz glass plate reflects a small percentage of the flasher's light output to a scintillator/light detector assembly (CH2 on the diagram). The opal diffuser is removed from the flasher aperture. A secondary PMT/scintillator detector (CH1) is kept in front of the flasher to ensure that the latter is working normally. Measurements from this PMT are equivalent to the ones measured in laboratory configuration 4.6.

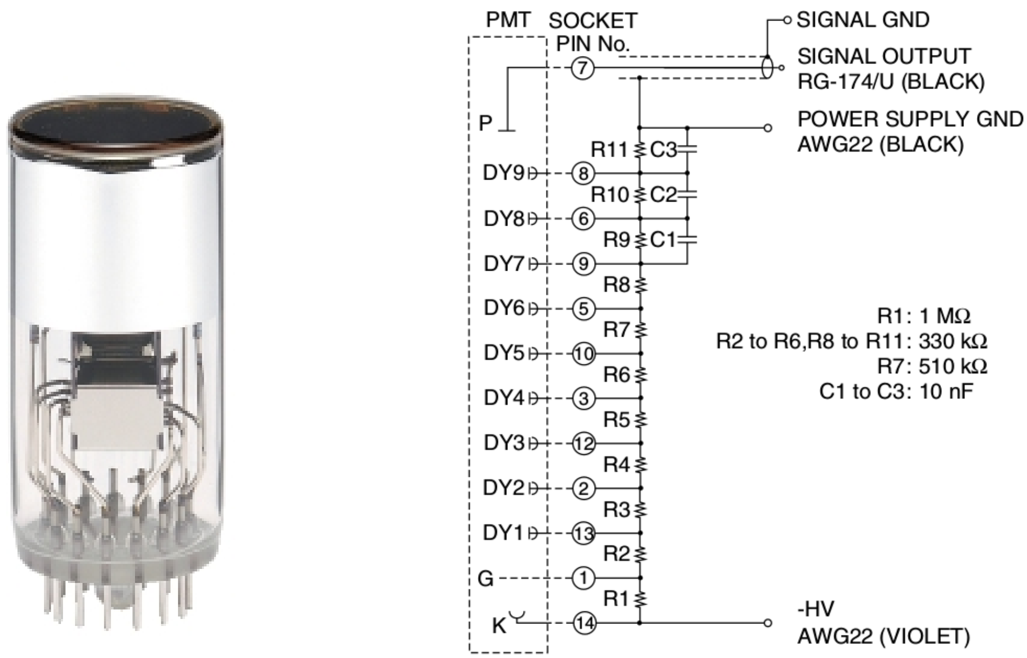

Figure 6.2: *Left:* Photograph of a R3998-02 PMT tube, which was used in the first light monitor design. *Right:* The schematic of the R3998-02 dynode chain. Individual dynodes cn be kept at different voltage to optimize the signal coming out of the anode; in the case of the R3998-02, the elements of the dynode chain are kept at a 3:1:1:1:1:1:1.5:1:1:1:1 voltage ratio.

6.2.1 Proof-of-concept: R580 PMT

In order to function properly as a light monitor, the R3998-02 PMT had to be illuminated with enough photons such as to be able to produce clearly separated charge distributions for all of the flasher's light levels. Additionally, the PMT's reponse needed to be linear over the entire range of pulse intensities, to faithfully measure the output of the calibration instrument.

A first test run of the experimental set-up was made using the R580 PMT used in the measurements of section 5. This was done in order to demonstrate the feasibility of the monitor concept: given a detector which we knew maintained a linear response in the laboratory set-up 4.6, we wanted to make sure that the number of photons reaching the PMT in the monitor configuration would be sufficient to produce clearly separated charge histograms, like the ones in figure 5.5. Figures 6.3 and 6.4 show the result of this test: as can be seen in these plots, the PMT receives less photons in configuration 6.1 than in configuration 4.6. This lack of photostatistics leads to charge distributions that are more closely packed (ie the standard deviation is of the same order as the mean of the distributions) than in the case of figure 5.5.

6.2.2 Modeling the light monitor photostatistics

At this point, it became worthwhile to estimate the total number of photons that can be theoretically detected by a PMT in this configuration, to see if the design suffered from a fundamental lack of photostatistics to work properly, or if there were still ways to improve the experimental set-up to get better-separated histograms than those of figure 6.3. Equation 20 was used as an approximation of the ideal scenario, where the number of photons reaching the monitor is only limited by the performances of the LEDs (quoted in table 4 of appendix A), the reflectivity of the 45° glass plate, the surface area ratio of the scintillator and the quantum efficiency of the photocathode. Under this approximation, the mean number of photons μ_{pe} that will be converted into photoelectrons will be:

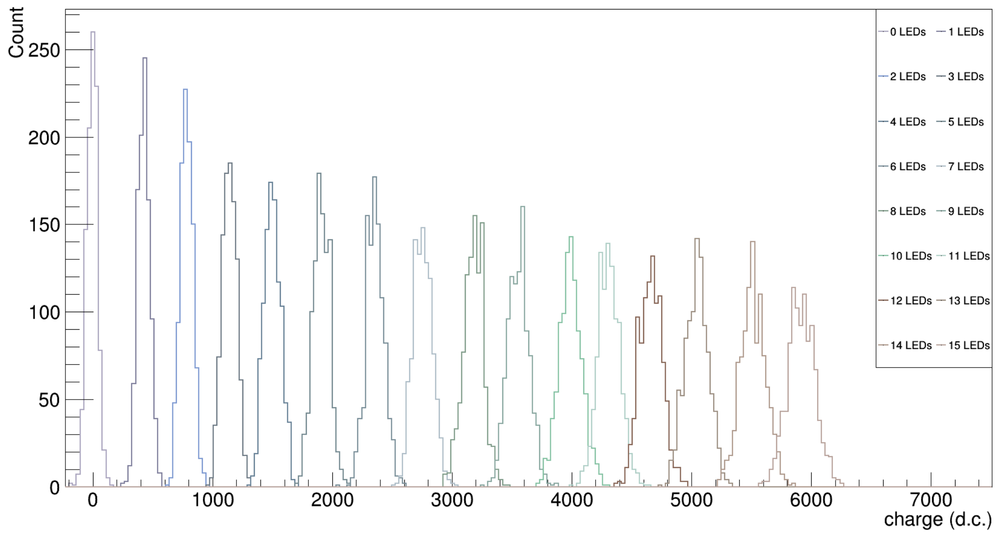

Figure 6.3: Superimposed charge histograms of the proof-of-concept monitor run. The values shown here pertain to the R580 PMT used at the monitor position: it only detects the light reflected by the quartz plate. This result exposed a problem: the current experimental set-up restricted the photostatistics of the light monitor.

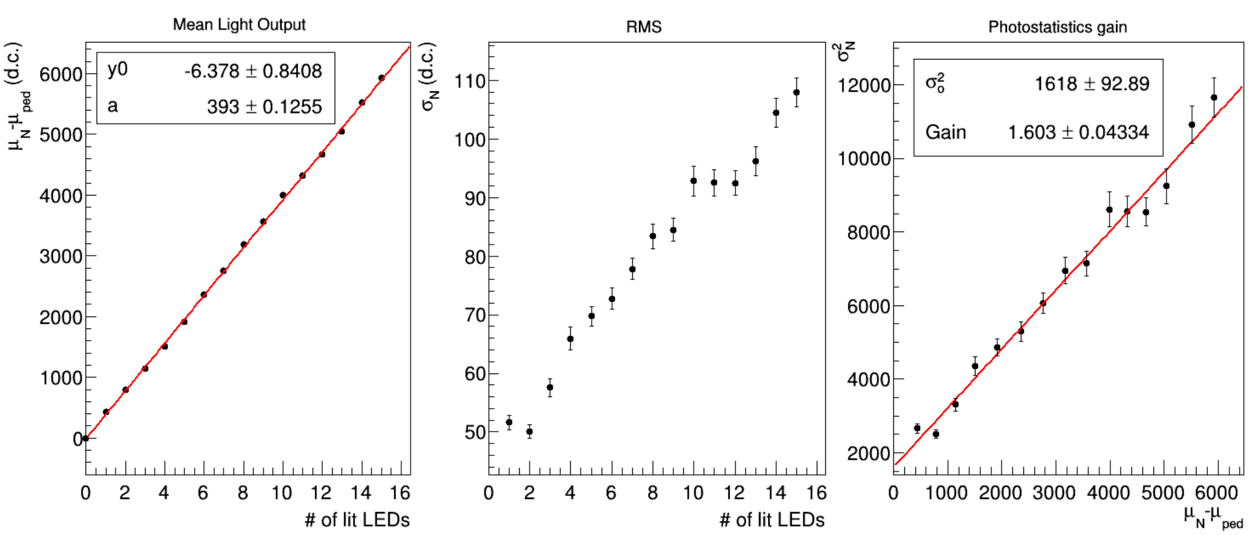

Figure 6.4: Photostatistics associated with the charge distributions presented in figure 6.3.

Table 1: Main physical properties of the light monitor simulations

ID	Parameter Name (Units)	Optimistic Scenario	Pessimistic Scenario
P_{max}	maximum radiant flux of an LED (mW)[1]	27.2	9.6
Δt	Duration of the pulse (ns)	10	
λ_{max}	Peak wavelength of UV LEDs (nm)	380	370
R^2	Reflection coefficient of the glass plate[2]	0.047	0.037
$\frac{A_{detector}}{A_{tot}}$	ratio of PMT/scintillator block surface areas[3]	0.028	
Q	Quantum efficiency of the photocathode (%)	25	20

[1] These values depend on the quality tier to which the supplied LED batch comes from.

[2] The range of values reflects a potential misorientation of the glass plate by 10°.

[3] Recall from section 4.4 that a wavelength-shifter emits the "shifted" light uniformly out of every surface of the block. The amount of photons collected by the PMT will therefore depend on the area proportion it covers, relative to the total surface area of the block.

$$\mu_{pe} \approx P_{max} \cdot \Delta t \cdot \frac{\lambda_{max}}{hc} \cdot R^2 \cdot \frac{A_{detector}}{A_{tot}} \cdot Q \tag{20}$$

Table 1 lists values for these parameters in a best and worst case scenario, based on the technical specifications of the hardware used. Given those parameters and equation 20, it is possible to estimate the mean number of photoelectrons produced in the optimistic and pessimistic case scenarios; with this particular hardware configuration, one gets $\mu_{pe,opt} = 1.7\text{x}10^4$ for the optimistic scenario, and $\mu_{pe,pes} = 3.3\text{x}10^4$ in the pessimistic scenario. In both cases, the standard deviation of the distributions will be neglible compared to the mean of the latter (since $\sigma = \sqrt{\mu}$ in Poisson statistics), which means that it should be in theory possible to produce very narrow charge distributions with the proposed monitor configuration.

Given the abundant photostatistics available for the light monitor, what experimental effects can explain the much broader distributions measured experimentally? A major issue

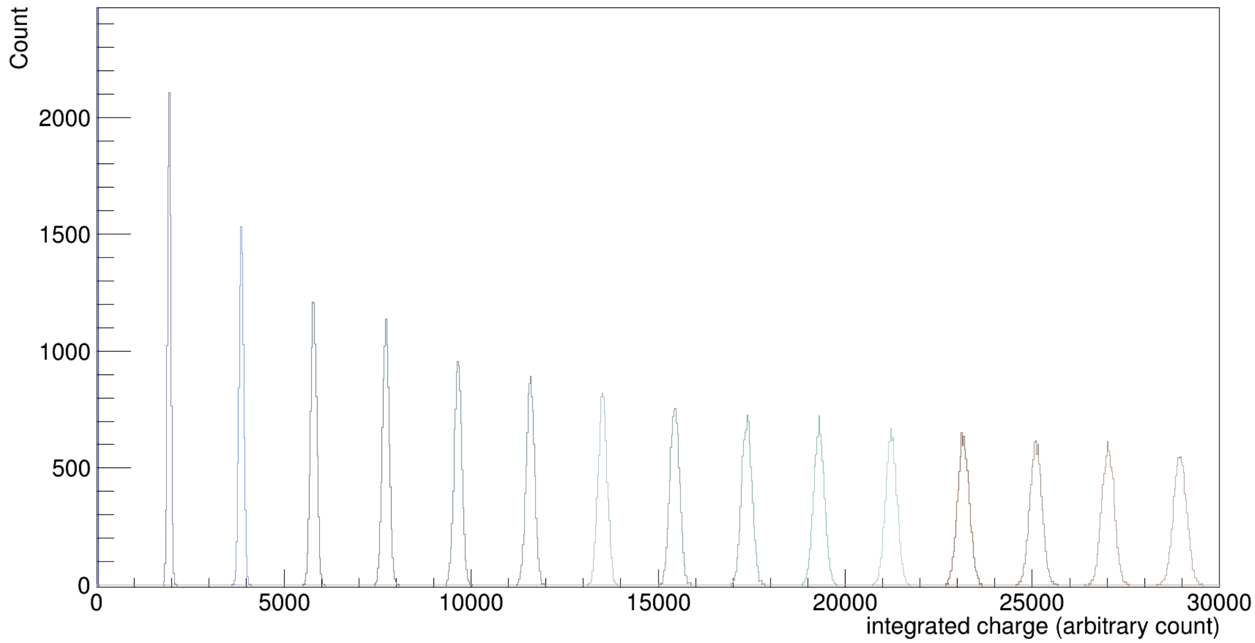

Figure 6.5: Simulation of an optimistic light monitor scenario (including the geometry factor), where a flasher runs its 15-LEDs cycle 8000 times. While the addition of a geometric factor reduces the available photostatistics of the light monitor, the width of the histograms are still small enough to clearly distinguish between the histograms.

that may explain this discrepancy between predictions and experimental data is the fact that the emission geometry of the LEDs has not been taken into account. As can be seen in figure A.1, the LEDs have an approximate emission angle of 40°, which means that the light coming out of the flasher's LEDs is not collimated. This leads to an inverse-square law loss of light intensity at the glass plate, located 100 mm from the flasher aperture, and at the scintillator block, which is further away from the glass plate by a distance of 300 mm. By adding this geometry factor into equation 20, the number of expected photoelectrons diminishes significantly: it becomes 1930 for the optmistic scenario, and 376 for the pessimistic one.

Figures 6.5 and 6.6 show the charge distributions of a simulated flasher run, with these values of μ_{pe} as inputs. As can be seen, the distributions are broader, and ressemble the ones seen in figure 6.3. Hence it is quite possible that the restricted photostatistics are caused by losses in the experimental set-up.

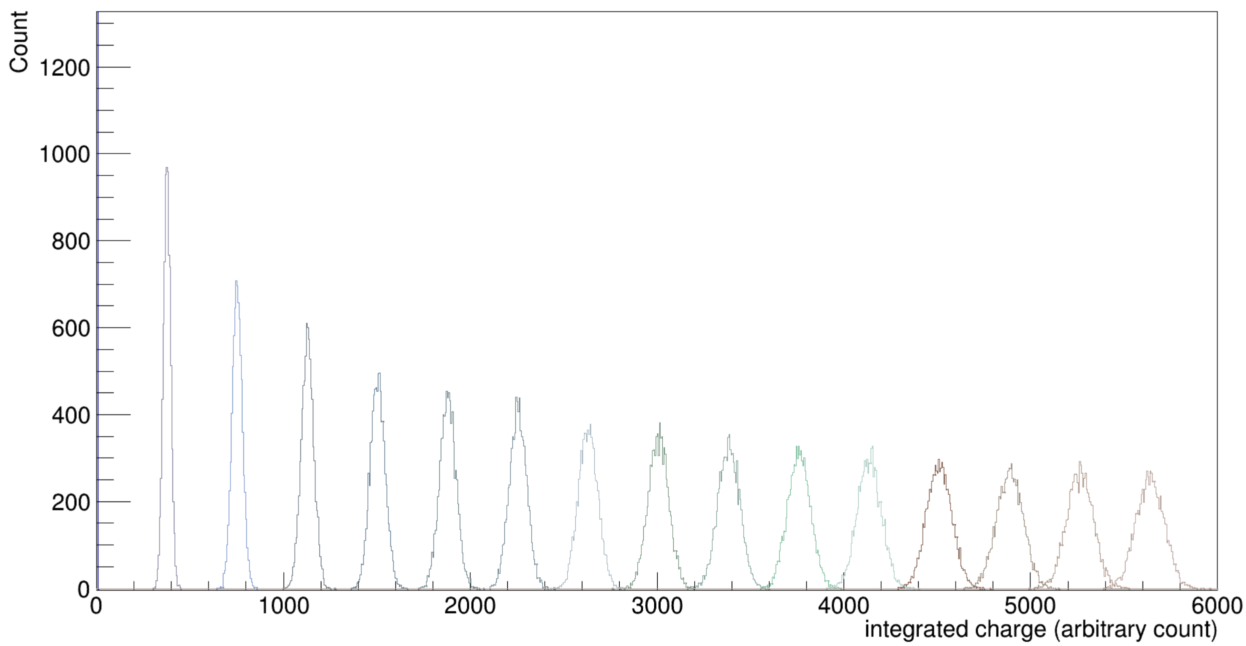

Figure 6.6: Simulation of the pessimistic scenario (including the geometry factor), with n=8000 LED cycles. In this case, where it is assumed that the LEDs and the PMT are performing according to their worst manufacturer's specifications, the addition of a geometry factor to the light loss process starts to produce charge histograms that overlap, similarly to those obtained experimentally in figure 6.3.

While this problem could be fixed in theory, by making sure that all the flasher's light output is perfectly reflected off the glass plate, this result underlines a major practical difficulty in the construction of the light monitor. In order for the latter to measure the absolute output of the flasher, we have to know with certainty the fraction of the total light output that is detected by it. This means that the monitor should only be able to detect the portion of light that is reflected by the glass plate, implying that effective light shields must be placed around the detector to allow only photons with a 90° angle to get to the scintillator block. This type of shielding usually takes a lot of space, which increases the distance of the light monitor from the LED and therefore reduces the statistics at its photocathode. Additionally, it will be difficult to accurately quantify the light losses due to the propagation of photons inside the manufactured casing; thus, an absolute measurement of the flux coming out of every flasher pulse will not be possible without detailed simulations of the light emission and propagation inside the instrument.

6.2.3 Experimental Results

Setting aside for a moment the difficulty in designing a proper light shield for the light monitor, the laboratory tests made using the R3998-02 PMT have identified another problem faced by the monitor concept. Figure 6.8 presents the first and second moments of the charge distributions for each flasher light level, as registered by the R3998-02 PMT in a monitor configuration. The plot on the left shows that at its recommended operating voltage, the PMT quickly leaves the linear regime to reach saturation, for the same number of photons as in the R580 case.

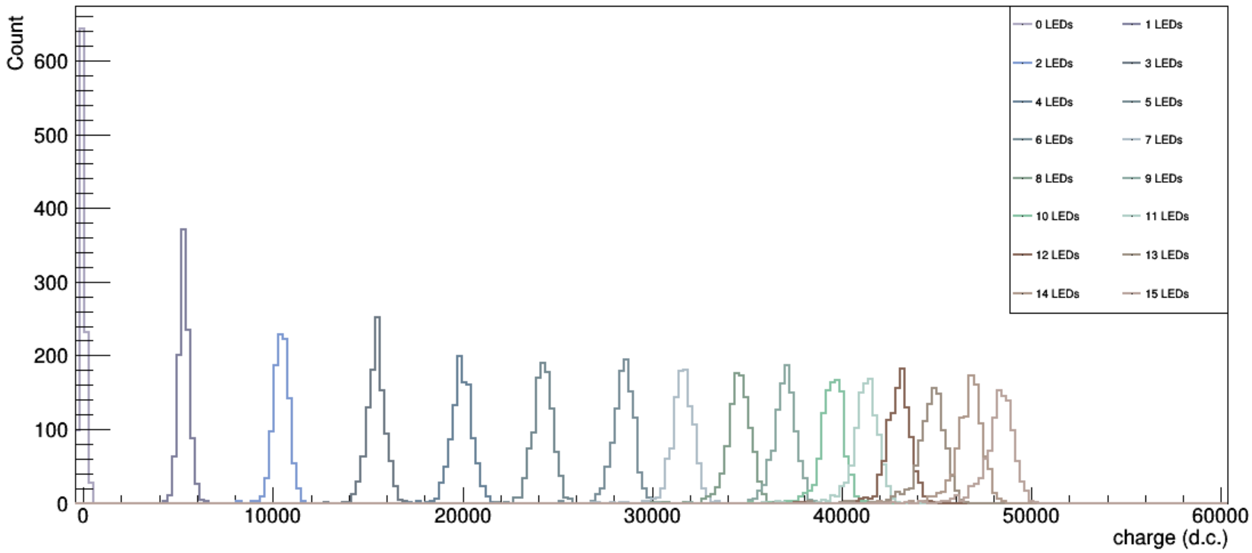

Figure 6.7: Charge distribution histogram of the light monitor using the R3998-02 at nominal bias, showing saturation effects for the brightess flasher pulses.

The R3998-02 has a higher quantum efficiency than the R580: this is identifiable by the fact that the ratio σ/μ of the histograms in figure 6.7 is narrower than in figure 6.3. This quality of the PMT allows the photodetector to collect more photostatistics for the same experimental set-up, which helps creating clearly separated histograms. However, the R3998-02's linear response range is too small to accomodate the large gain by which bright pulses are amplified. In order to adapt the sensor to this situation, one can either reduce the amount of photons reaching the photocathode, or reduce the gain of the PMT until the electron charge distribution fits inside the detector's linear range.

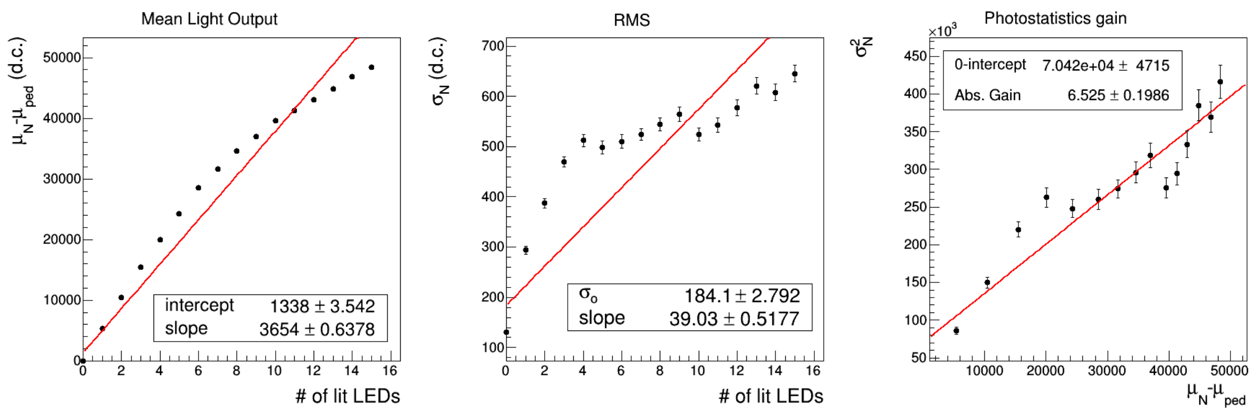

Figure 6.8: Photostatistics of the light monitor using the R3998-02 at nominal bias. The non-linear behaviour of the light sensor is clearly visible on the left figure, where the measured light output approaches saturation toward the last few LED light levels.

The first option implies covering part the PMT's photocathode to reduce its photoelectron production efficiency. This is not desirable, since we have already shown in the earlier R580 tests that in the current experimental set-up, light losses due to geometry effect were already producing integrated charge histograms that were starting to overlap. This leaves the second option, which was tested by gradually diminishing the voltage bias of the PMT tube. Linearity was achieved at a voltage of 500V, which is half of the recommended operating voltage for this type of PMT.

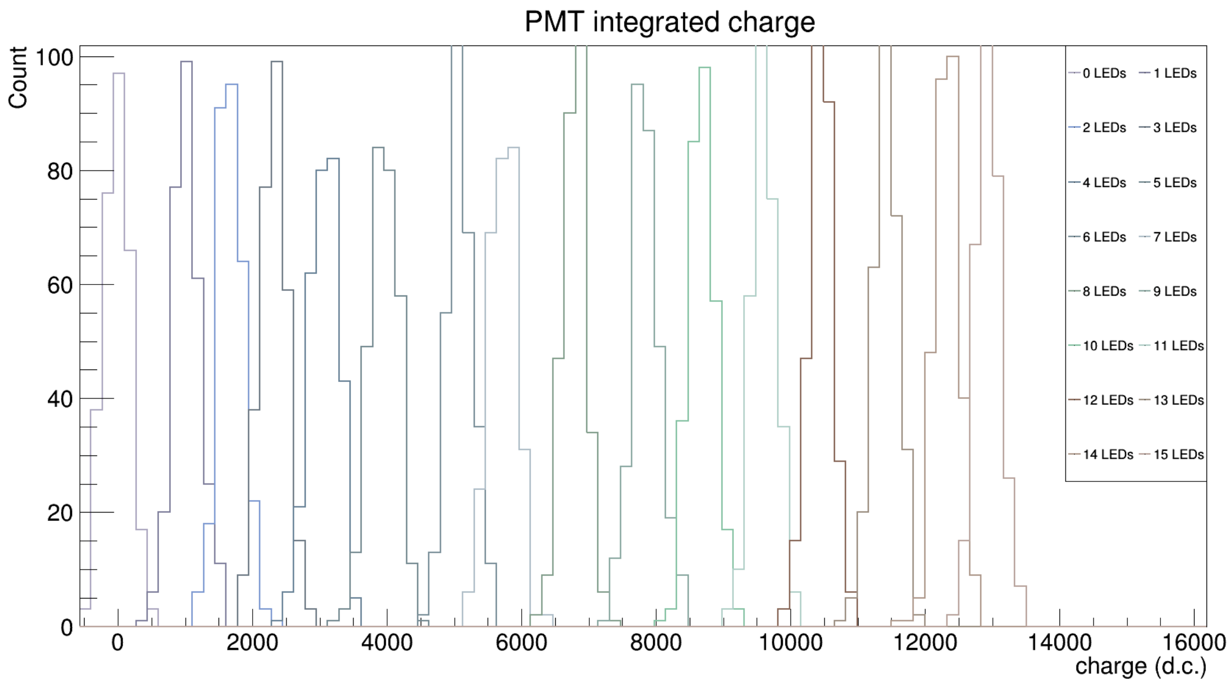

Figure 6.9: Superimposed charge distribution of a R3998-02 laboratory run, where its bias voltage was tuned down to maintain a linear response.

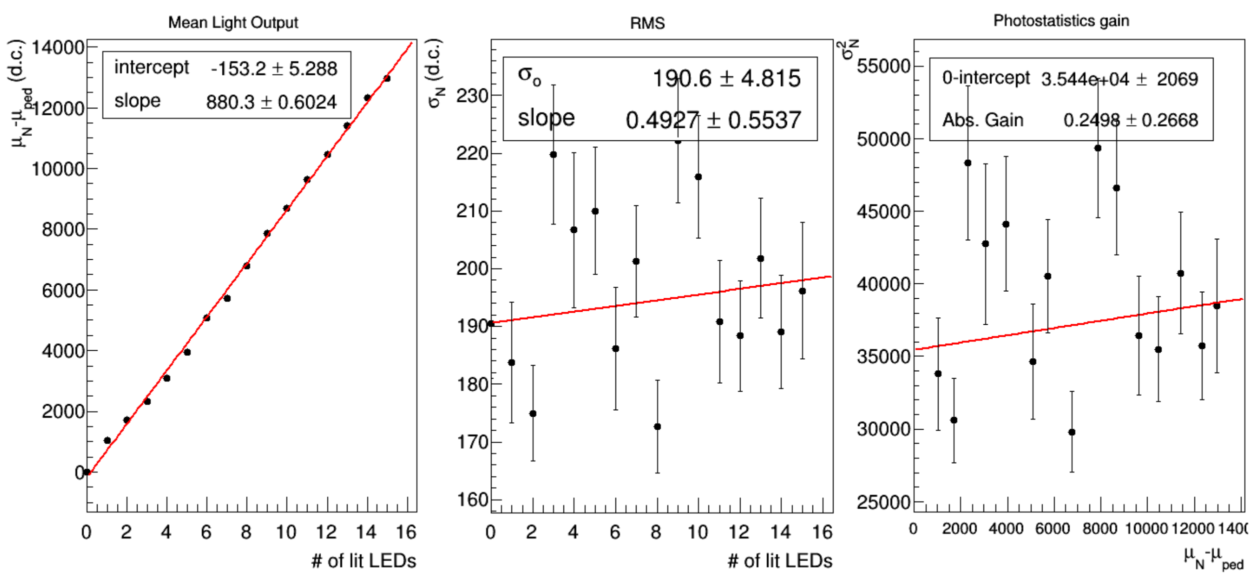

Figure 6.10: Photostatistics of the same laboratory run. Using a bias voltage of 500 V instead of the recommanded 1100 V, the statistical scatter of the charge distribution's variance measurement increases, leading to a less precise fit of the gain slope.

The preliminary results presented in figures 6.9 and 6.10 are encouraging: it appears to be possible to get the R3998-02 to stay in its linear response range by operating the PMT at a significantly reduced bias voltage. The downside of this method however is that the scatter in the data starts to influence the quality of the photostatistics gain fit.

6.3 Second Design: Silicon Photomultipliers

A second type of light sensor that was tested for the purpose of the light monitor was the sixteen-cell, Array-SB *silicon photomultiplier (SiPM)* from SensL [51]. Silicon photomultipliers constitute a relatively new type of low-light photosensors, and their working principle is quite different from that of a PMT. An SiPM is a semiconductor-based device which consists of thousands of *microcells*, which are simple circuits joining together an avalanche photodiode (APD) and a resistor. When hit by a photon, the APD will produce an avalanche of signal electrons, and the sum of the electrons collected by the array of microcells will constitute the output of the SiPM, when it is illuminated by a light pulse. Once a microcell has triggered on a photon, it becomes unavailable until its APD has recharged: this process can take several micro-seconds, which means that for the purpose of detecting 10 ns light pulses, the maximum number of photons that can be detected by an SiPM is roughly proportional to the number of microcells present in the device [52].

SiPMs offer several advantages over PMT tubes when it comes to the detection of low-intensity light, which is why they are currently tested as potential new-generation cameras for IACTs [53]. First, they consist of semiconductor-based devices, which allows for the production of detectors with advantageous form factors, at potentially lower cost than PMTs. Second, avalanche photodiodes do not need vacuum tubes or sensitive photocathodes to detect photons, which means they are impervious to damages made by really bright illumination conditions such as full-moon observations. Third, SiPMs operate with relatively low bias voltages ($\approx$25-30 V), which eliminates operational hazards related to the high-voltage supplies of PMT-based Cherenkov telescopes. All these advantages also make this sensor technology interesting for the flasher's light monitor. To test its performance, the SensL Array-SB4 SiPM was connected to a customized dual-channel amplifier board, and placed

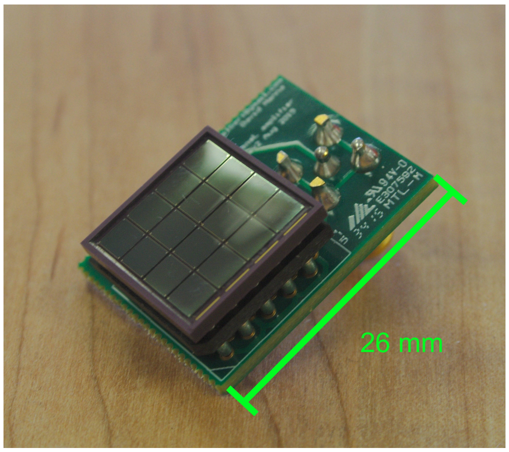

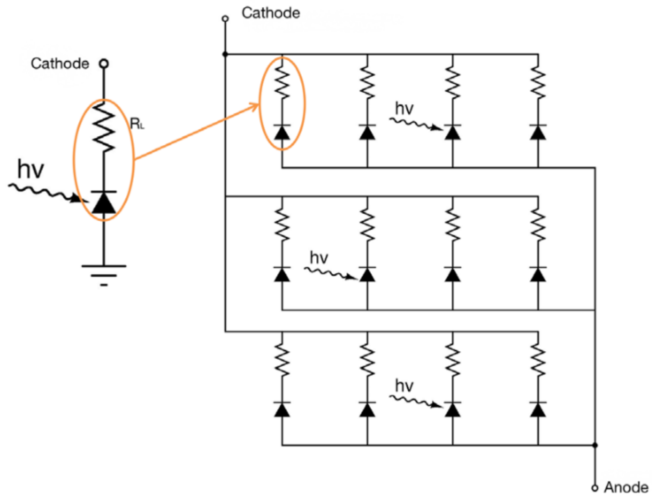

Figure 6.11: *Left:* Photograph of a SensL Array-SB4 silicon photomultiplier. *Right:* Electronic circuit of a typical SiPM cell: an SiPM consists of thousands of microcells (a simple circuit made of an avalanche photodiodes (APD) and a resistor). When hit by a photon, the APD will produce an avalanche of signal electrons, and the sum of the electrons collected by the array of microcells will constitute the output of the SiPM.

in the same laboratory set-up as the R3998-02 PMT. The results of the initial tests made with the SiPM are presented in figures 6.12 (for the pulse sequence), 6.13 (for the charge distribution), and 6.14 (for the photostatistics).

A significant difference in the results of the SiPM monitor compared to the PMT one is the shape of the detected pulses, plotted in figure 6.12. In order to make a valid comparison with the PMT monitor results, the integration window was set to the same length of 20 ns, even though the pulses were significantly longer than that value; this is due to the fact that the integration window on the VERITAS FADCs has already been fixed and optimized for observing conditions, and cannot be changed solely for the purpose of calibration measurements. The long trailing end of a typical SiPM pulse is a direct consequence of the time required to recharge the microcells once they have been hit by a photon. To circumvent this microsecond-long delay in the SiPM response, certain sensor models offer a special "fast-output", which consists of a capacitor wired in parallel with the APD-resistor

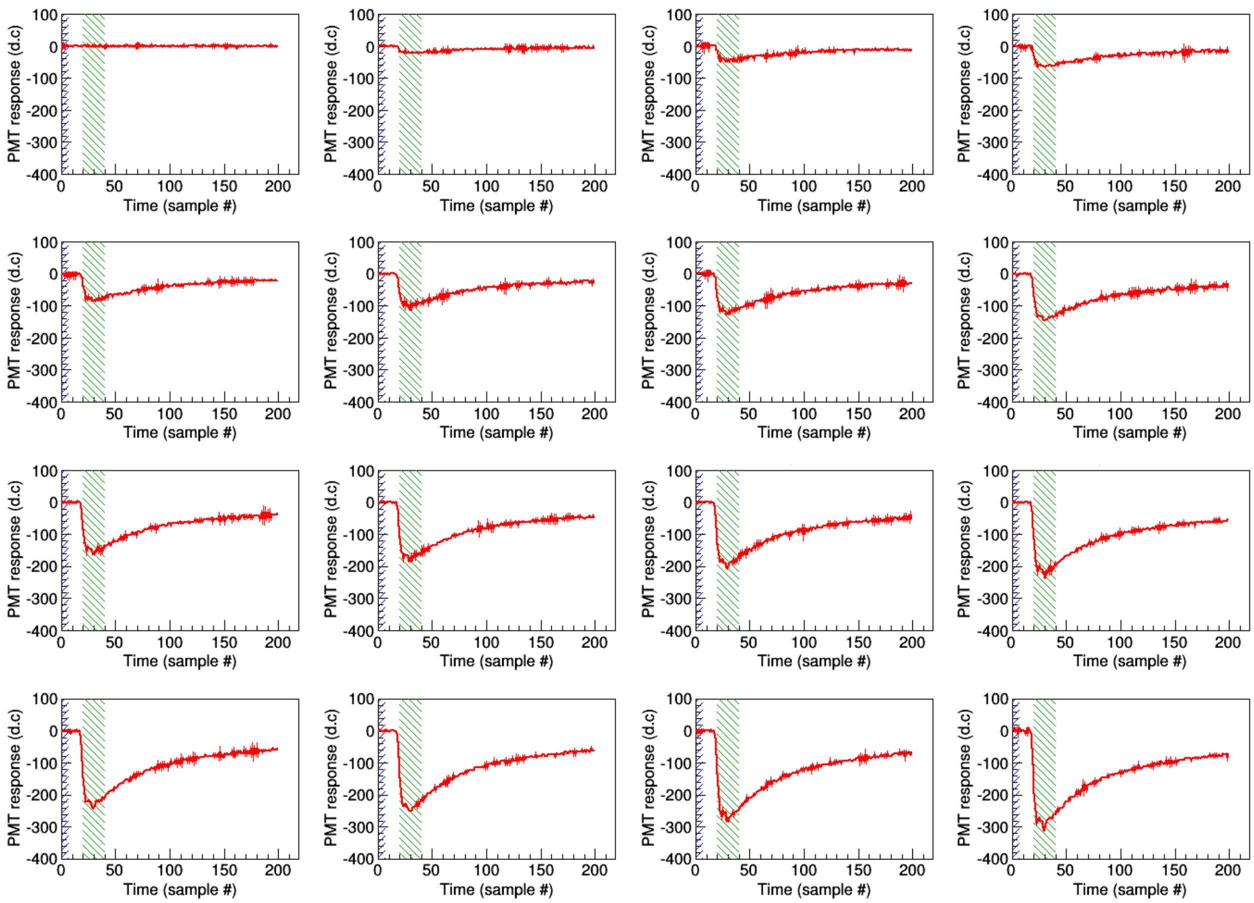

Figure 6.12: Example of a sequence of pulses measured by a SensL Array-SB4 SiPM sensor. Regular SiPM outputs are characterized by a microsecond long tail to their pulse, which is caused by the slow recovery time of the avalanche photodiode. The green region corresponds to the same integration window size as in figure 5.1.

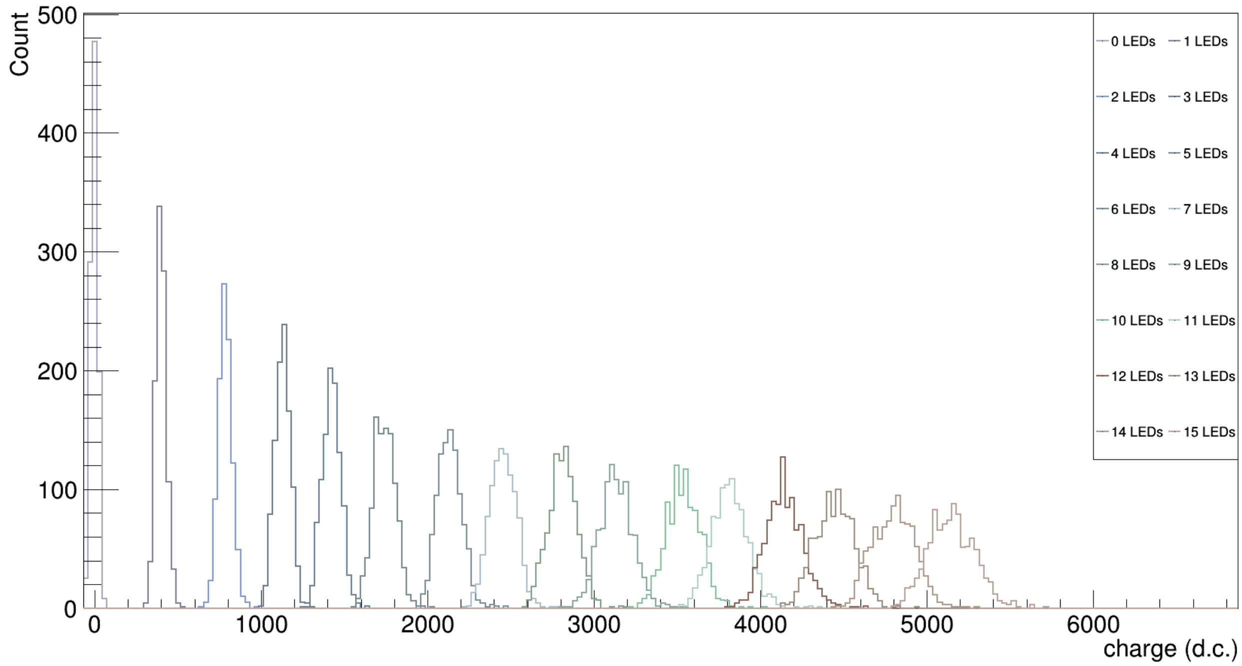

Figure 6.13: Superimposed charge histograms of one of the light monitor test with the SiPM. While the response of the sensor appears to be linear, the width of the last few histograms appear to be diverting from a typical Poissonian growth.

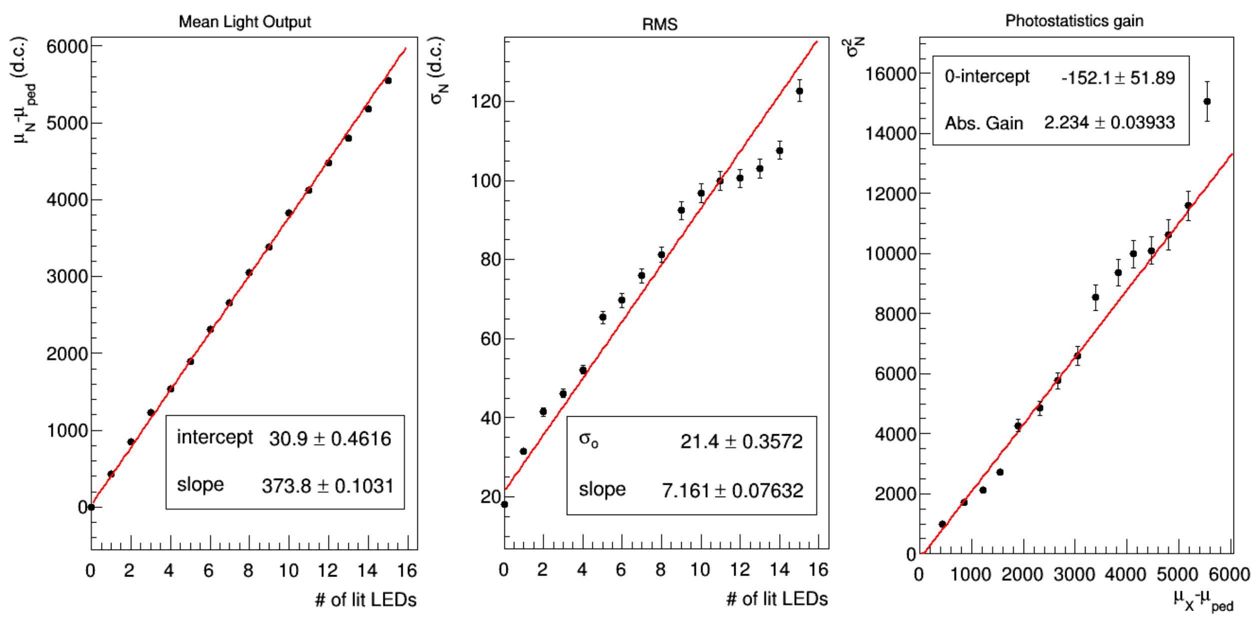

Figure 6.14: Photostatistics of the histograms of figure 6.13. While the response of the sensor appears to be linear, the width of the last few histograms appears larger than expected for a purely Poissonian process.

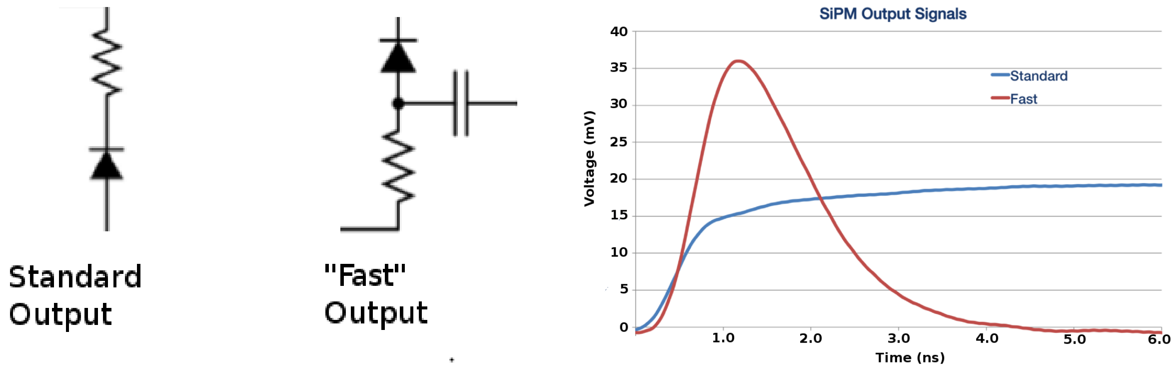

Figure 6.15: *Left:* Circuit diagrams of the standard and "fast" SiPM output. The latter is produced by adding a capacitor in parallel to the standard circuit, to obtain the differential signal of the former. *Right:* Comparison of the pulse shape of a standard and "fast" SiPM output. Source: [54].

circuit. This type of output, which is not available on the Array-SB4 SiPMs, uses the fast recharge time of the capacitor to differentiate the blue pulse shape seen on the right plot of figure 6.15, leading to a pulsed signal that is significantly shorter (the red curve on the same plot). Knowing this, the use of an SiPM with fast-output would produce pulses that would fit inside the traditional integration window, and this might have helped reducing the charge measurements uncertainties arising from not catching the entire pulse within the integration window.

A major feature of the histograms and photostatistics shown in figures 6.13 and 6.14 is the notable deviation from Poissonian statistics in the brighter flasher pulses: event though the mean charge detected remains perfectly linear, the photostatistics plot shows a significant deviation from linearity, meaning that the RMS of the higher charge distributions probably include non-Poissonian noise processes that significantly influence the statistics of the SiPM response.

A possible source for this type of noise might pertain to the highly sensitive nature of the SiPM gain. The electronic gain of an SiPM is proportional to the *overvoltage* ΔV: the voltage difference between the sensor's bias voltage and a quantity called the *breakdown voltage*

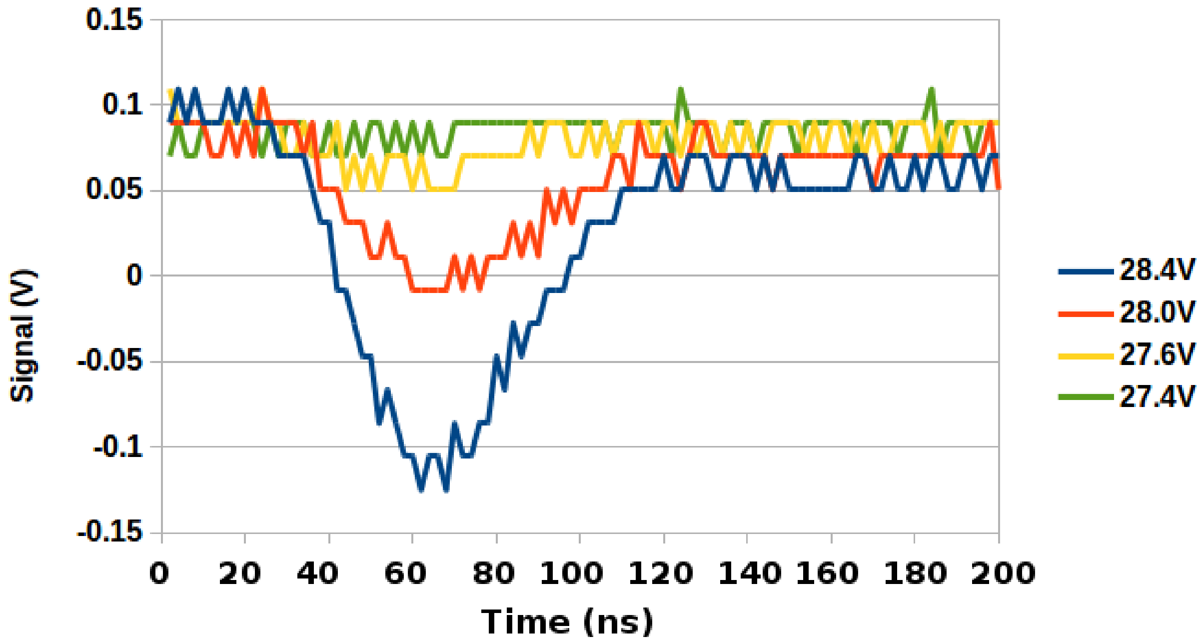

Figure 6.16: Shape of a 1-LED flasher pulse as detected by the array-SB4 SiPM, operated at various bias voltages. A pulse starts to form at the breakdown voltage (which is here approximately equal to 27.4 V), and its amplitude can vary greatly with a 1.0 V increase in bias.

$V_{breakdown}$. The latter defines the reverse bias one needs to apply to the APDs of the sensor for them to be able to work in avalanche mode.

Typical overvoltage values do not surpass 2.0 V, and have a significant effect on the gain at the millivolt scale: Figure 6.16 shows the significant change in pulse size when the operational voltage of the Array-SB4 is changed by up to 1.0 V. This characteristic of SiPMs implies that the bias supplied to the light monitor must be stable to within less than 0.1 V, which is not necessarily the case with the power supply used in the laboratory. Figure 6.17 plots the integrated charge distribution of the 1-LED events as a function of their acquisition time. It was noticed during this particular run that the power supply bias dropped slightly during the run, which translated into a drift in the charge distribution over time. This drift is a significant source of scatter in the charge distribution, and it can be minimized by letting the power supply and SiPM stabilize after turning the power on (see figure 6.18).

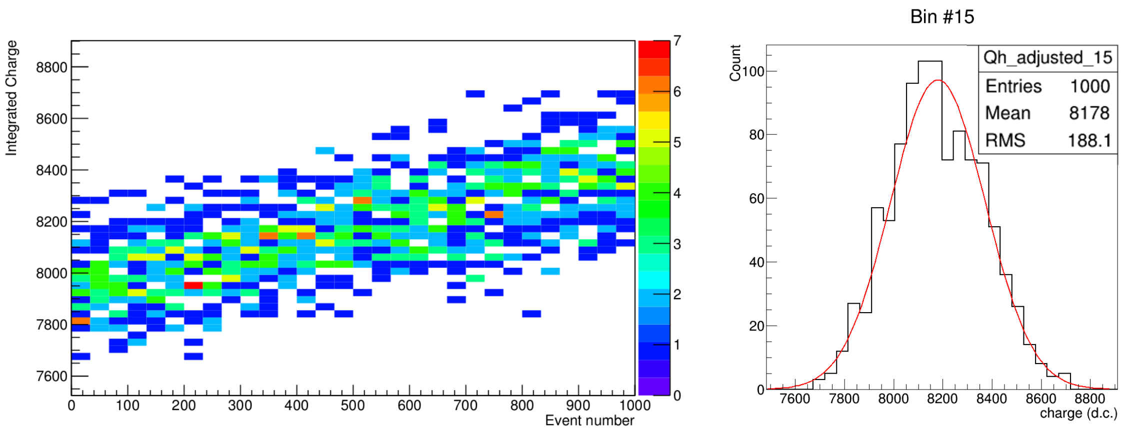

Figure 6.17: *Left:* Charge distribution of the 15-LED light level as a function of time, where we see that an unstable power supply leads to a drift in the SiPM's gain. *Right:* Close-up of the 15-LED light level charge distribution histogram, showing a relatively large width (188).

Temperature effects also come into play when working with SiPMs. Because temperature affects the conductivity of the semiconductor material, it also affects the breakdown voltage at which the electrons become free to pour out from the anode: lower temperatures mean higher conductivity, which itself means a lower $V_{breakdown}$. Given a fixed operational voltage bias, the lowering of the breakdown voltage will lead to an increase of ΔV, which will increase the gain of the sensor. Morover, operating an SiPM at lower temperatures will have the advantage of reducing, for a fixed gain, the electronic noise within the device, namely the *dark count rate*, which is the rate at which microcells are spuriously triggered by thermally-generated charge carriers [55] [56]. Section 6.4 will report on attempts to capitalize from this characteristic of SiPMs.

Finally, the array of microcells of an SiPM is also subject to *cross-talk noise*, a phenomenon by which an avalanche of electrons in one microcell, may trigger an avalanche on the neighbouring cell. This type of noise is a strong function of the geometry of the micro-fabricated array, since it depends on the amount of current leakage between adjacent strips of semiconductor. [57]

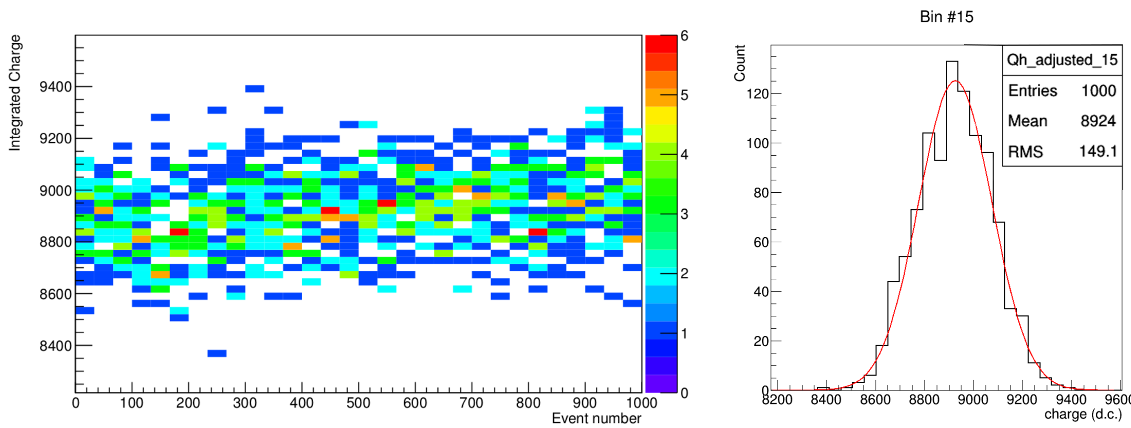

Figure 6.18: *Left:* Charge distribution of the 15-LED light level as a function of time, where this time the run was acquired after the power supply had time to stabilize. *Right:* Close-up of the corresponding 15-LED charge distribution histogram, where it can be seen that the RMS is now smaller (149) than in figure 6.17.

6.4 Active thermal cooling experiment

Given that reducing the electronic noise of the SiPM could potentially narrow the integrated charge distributions of a light monitor, an experimental set-up was built to assess the feasability of including an active cooling module, based on *Peltier coolers*, within the light monitor design. Peltier cooling is a thermoelectric effect whereby a DC current flowing through two different semiconductor materials will create a temperature gradient at their junctions. This effect arises because the movement of charge carriers (associated with an electric current $\vec{j}$) within a semiconductor will generate an accompanying thermal current $\frac{d\vec{Q}}{dt} = \Pi\vec{j}$. Because the Peltier coefficients Π of the two materials are not the same, one side of the device will be accumulating heat faster than the other, leading to the generation of a heat pump between the two sides of the device [58]. Figures 6.19 illustrates this concept.

The first test conducted with a Peltier cooler was made to determine the maximum temperature gradient achievable on an SiPM chip, when the latter was placed in contact with a Peltier cooler module. Figure 6.20a shows the configuration of the experiment: in this case,

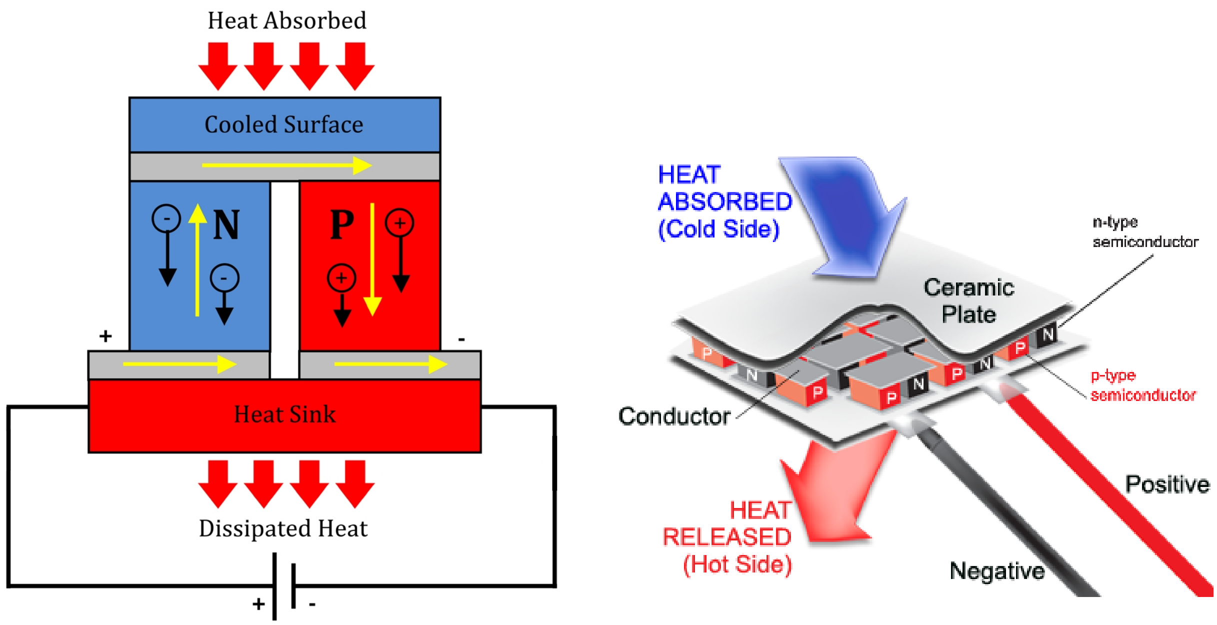

(a) (b)

Figure 6.19: a) Diagram showing the physical principle behind the Peltier effect: as an electrical current is sent across two different semiconductor materials, a thermal current forms as well, in the direction of motion of the main charge carriers (electrons in the n-type material, holes in the p-type). However, because the Peltier coefficients of the two materials are not the same (in this case $\Pi_{n-type} < \Pi_{p-type}$) the carriers in both materials end up transporting more heat to the bottom electrode than to the top one. b) In a Peltier cooler like the one pictured here, the set-up described in 6.19a is repeated into an array of smaller cells, to maximize the temperature gradient it is possible to obtain.

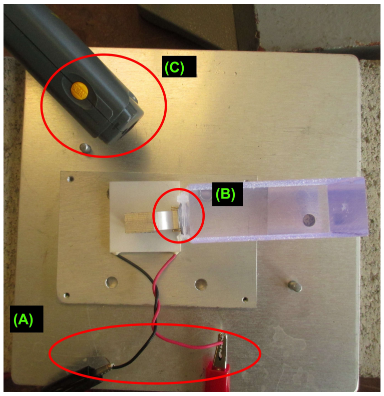

(a)

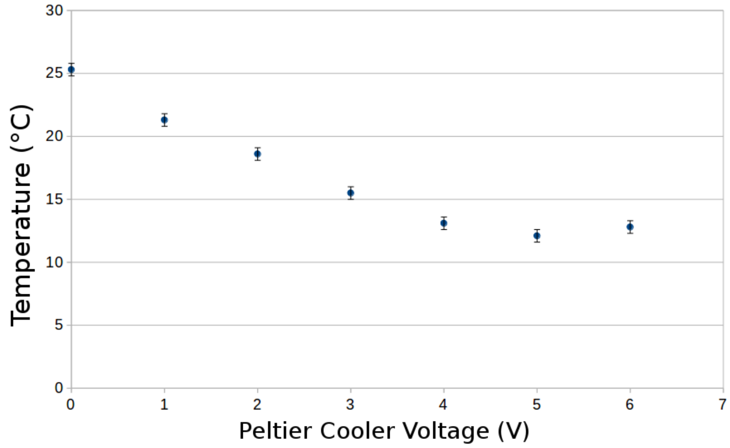

(b)

Figure 6.20: a) Photograph of the experimental set-up used to evaluate the performance of the Peltier cooler: as the bias voltage of the device is changed (A), the temperature at the surface of the SiPM (B) is monitored using a remote laser thermometer (C). b) Temperature of the cooled SiPM as a function of the voltage applied to the Peltier cooler.

the SiPM was not under a voltage bias, but coupled with a thermally conductive piece of aluminum, which was itself standing on the cold side of the Peltier module. Figure 6.20b shows how the measured temperature varied as a function of the voltage applied to the module.

The initial test has shown that a Peltier cooler can rapidly (ie. in a matter of seconds) cool down the sensor by more than 10 °C, which could mean a reduction of the dark count rate by a factor of one-half [52]. Following this result, a flasher run was recorded using a cooled SiPM as the monitor light sensor. Using the same thermometer as in the previous set-up, the temperature of the SiPM prior to turning on the cooler was measured to be 23-25°C: figure 6.21 shows the distributed charge histogram, and figure 6.22 the photostatistics of this run. Then the cooler was turned on, and an acquisition run was started once the temperature stabilized around 12-13°C: figures 6.23 and 6.24 show the effect of this temperature drop in the measurements made by the sensor.

The preliminary results obtained with the thermoelectric cooler show that a drop in 10-

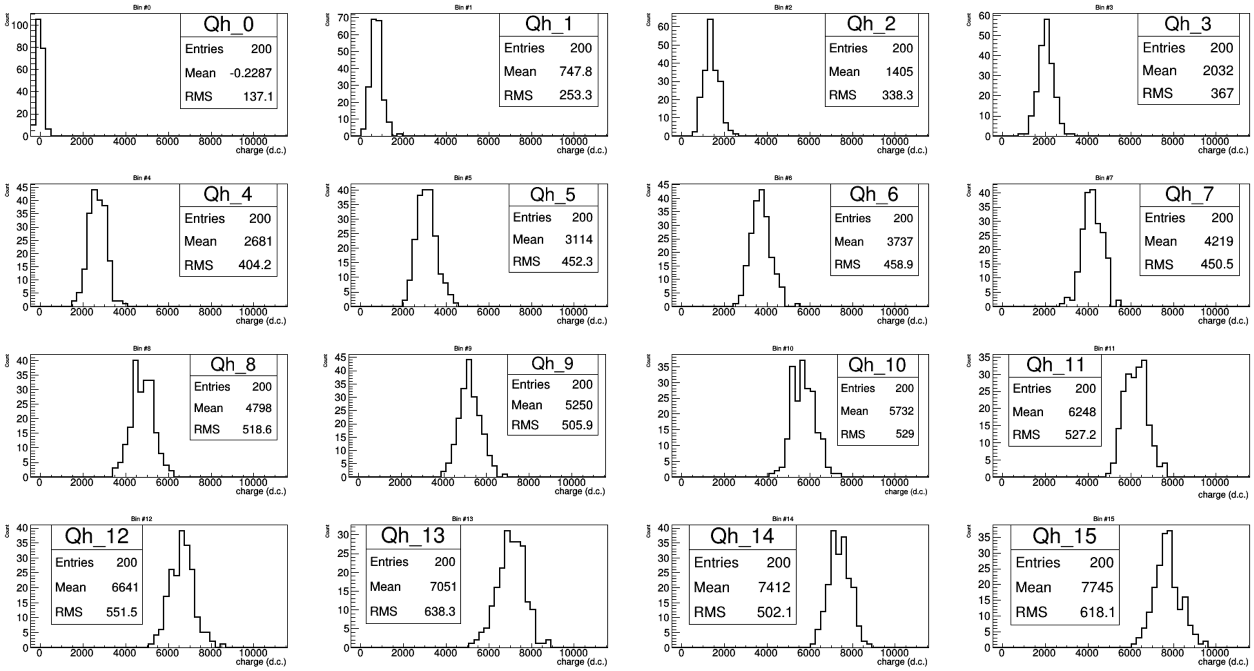

Figure 6.21: Integrated charge histograms from a laboratory test of a Hamamatsu MPPC S10985 SiPM sensor, at room temperature (23-25°C). A flasher run was recorded using the SiPM as the monitor light sensor, in the laboratory set-up illustrated in figure 6.1.

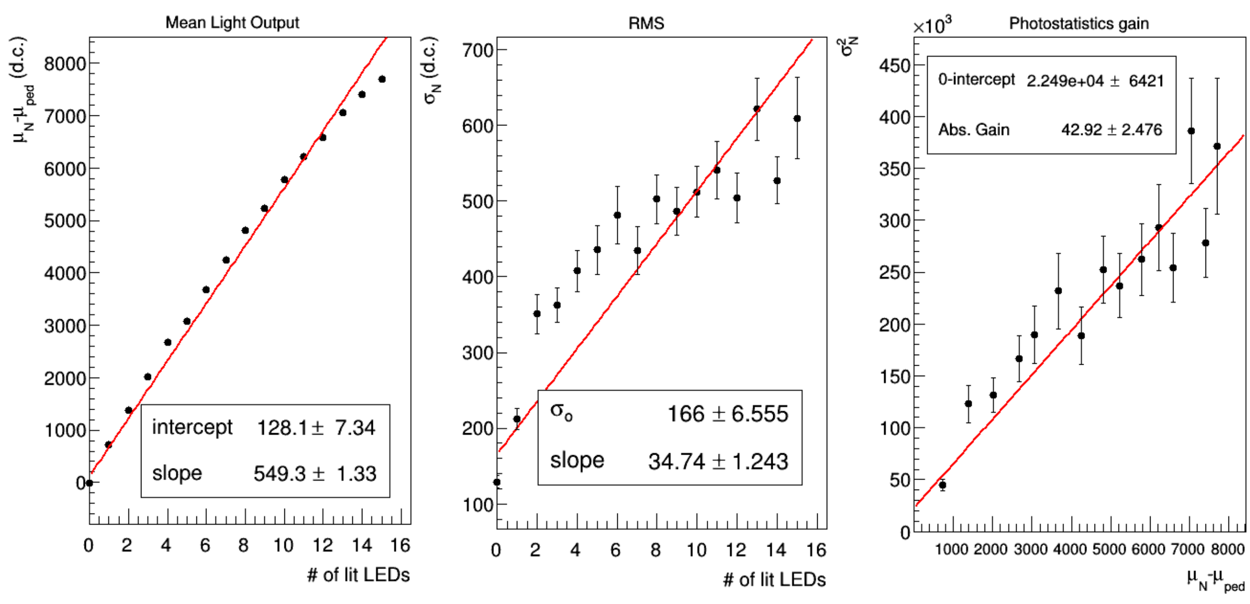

Figure 6.22: Photostatistics of the charged histograms presented in figure 6.21. While the last two or three LED light levels show the beginning of a non-linear behaviour, the obtained linear fit on the photostatistics gain plot matches the data well ($\chi^2 = 23.08$ (13 d.o.f)).

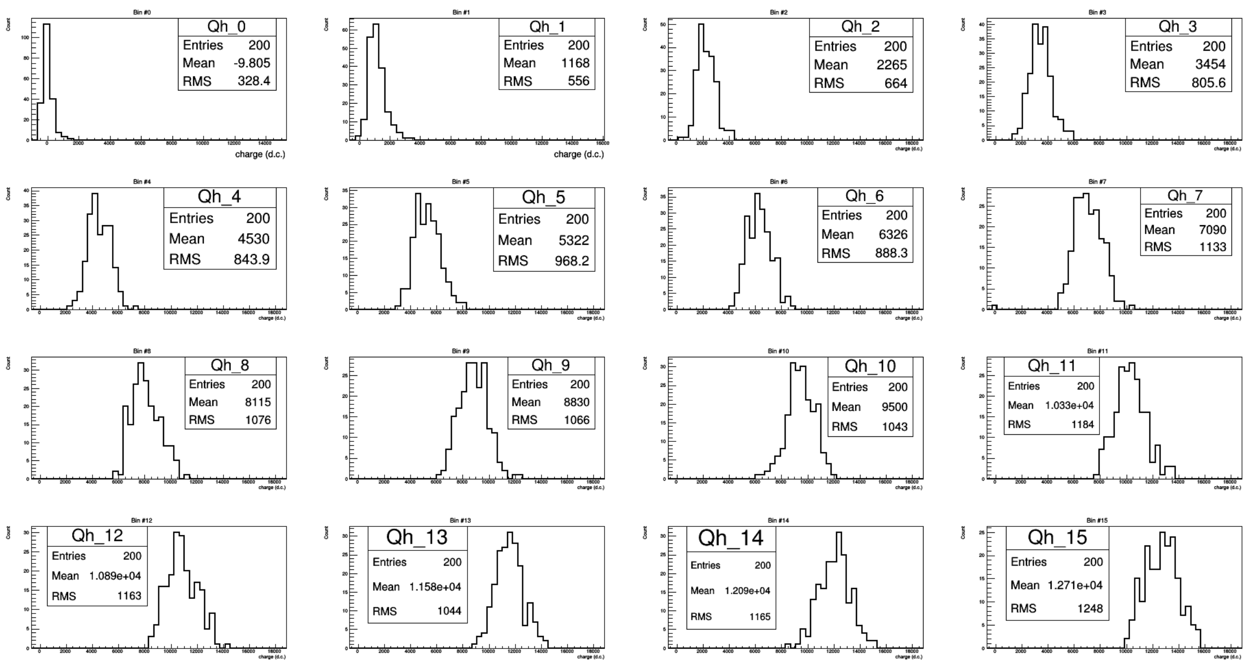

Figure 6.23: Integrated charge histograms from a laboratory test of a Hamamatsu MPPC S10985 SiPM sensor, this time cooled with the help of a Peltier cooler. The temperature of the sensor a minute after activating the cooler was measured to be in the 22-13°C range.

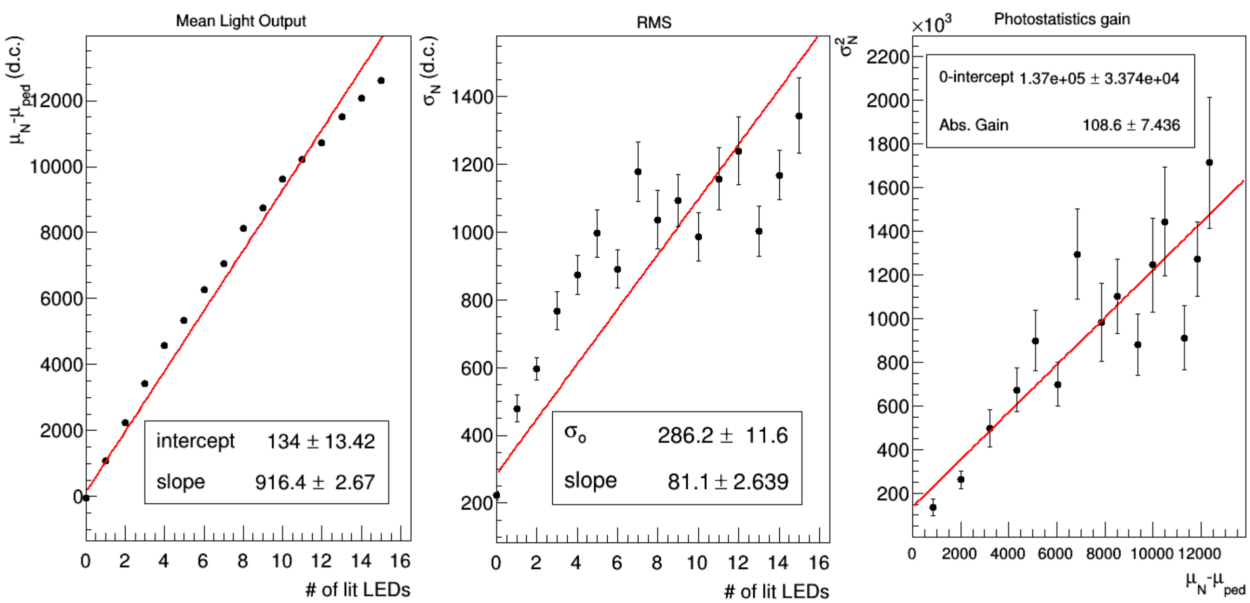

Figure 6.24: Photostatistics of the charge histograms presented in figure 6.23. These results show how the overvoltage of the SiPM, which dictates the gain of the device for a constant supply voltage, can be extremely sensitive to the temperature: a drop in temperature of approximately 10°C has led to an increase of the measured absolute gain by a factor of 150% ($\chi^2 = 24.57$ (13 d.o.f)).

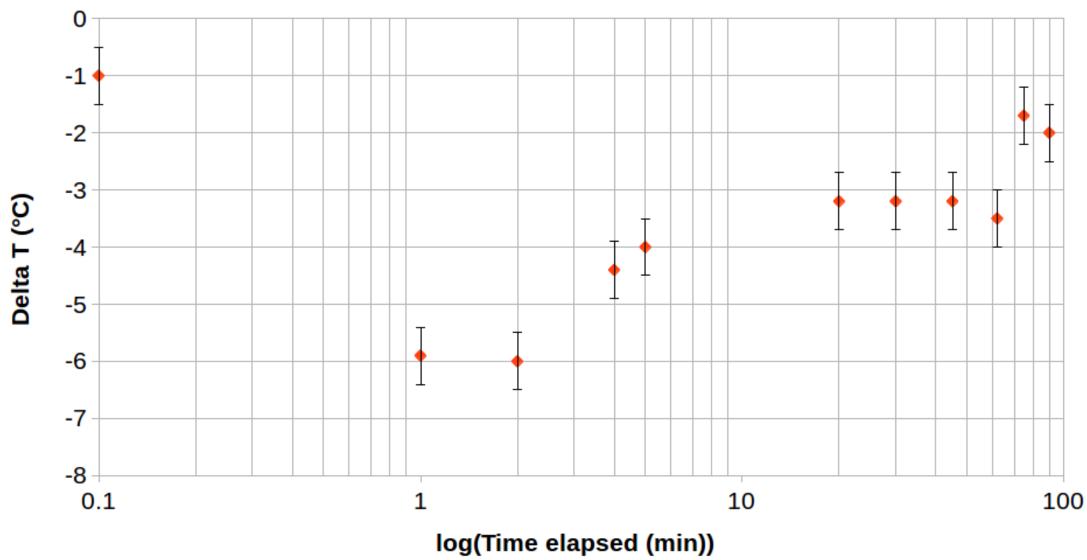

Figure 6.25: Results of a cooling test where the temperature of the SiPM was monitored over a period of 90 minutes.

13°C yields a 150% increase in gain: in order to maintain the latter constant in this cooling experiment, one would have had to reduce the SiPM's bias voltage by approximately the same amount, and measure how the RMS of the charge histogram changes at lower operating temperature. Unfortunately, this last test was never performed, mainly because it was realized that the thermocooling device was unable to maintain a stable temperature over the course of a long period. Figure 6.25 shows how the temperature of the experimental set-up evolved over a period of 90 minutes: while the Peltier cooler is able to significantly lower the temperature after one minute, the inability of the heat sink to quickly evacuate the heat building up on the hot side of the cooler leads to a slow increase in the temperature of the cooled device. This results therefore underlines a conceptual difficulty that arises with the introduction of active cooling: given the hot temperatures of Arizona, an actively cooled light monitor might not be able to do better than a one or two degree temperature drop.

At this point, the inconvenience of an active cooling system seemed to overcome its advantages. In the harsh environmental conditions of Arizona (where the temperature can vary by 20 degrees between night and day), it might be difficult to even simply stabilize the temperature of the sensor with a cooling system. Additionaly, given the current lack of a high-precision voltage control system on the telescopes, and the difficulty in modeling the non-Poissonian sources of noise (like cross-talk noise) inherent to this type of detector, it was concluded that a lot more work, beyond the scope of this project, needed to be made before using SiPMs as a flasher light monitor. Despite this fact, the results obtained with this new technology look encouraging, and the next section will try to lay down the ground work for a successful use of SiPMs with the flasher.

6.5 Future Work

The goal of the light monitor was first to provide a stable and trustworthy estimate of the light output given by each flasher pulse fired at the VERITAS camera and second, serve as a convenient pulse tracking method.

The laboratory tests made on the proposed on-board flasher light monitor have shown that both the R3998-02 PMT and the Array-SB4 SiPM were not suitable detectors for that purpose. The R3998-02 PMT did not have the response range required to properly measure with suffient statistics (to produce clearly separated charge distributions) the light of all 15-LED light levels of the new flasher. Its photocathode would have also been damaged by a constant exposure to daylight, unless a shutter would have been added to the intrument. Meanwhile, while the SiPM did allow us to better distinguish between charge distributions, the characterization of its noise was rendered more complex due to the sensor's extreme sensitivity to temperature and bias voltage flucutations.

Morover, the very design of the light monitor, where a 45-degree angle glass plate redirects a constant fraction of the flasher's light, turned out to be very difficult to implement: bulky light shields had to be placed around the set-up to ensure that only the correctly reflected light went through the detector's aperture, which meant that it would be very difficult to properly integrate the monitor in a compact enclosure like the one designed. Moreover, further modeling of the light propagation through a potential flasher would definitly need to be made in order to compute the actual light fraction that was being monitored, given the wide emission angle of the LEDs and the many metallic and reflective surfaces present inside the flasher casing.

Given these results, the final version of the new flasher did not include a light monitor; the absolute throughput of the flasher can still be estimated using the current camera channel average method, and alternative methods can be used to ensure a better tracking of the flasher's pulses. The easiest approach on this matter would be to make a copy of the external flasher trigger signal, and send it to a counter which would then label each flasher run event with a number ranging from 0 to 15. This sort of system could be implemented directly in the L3 room, without the need for telescope-based systems.

Finally, in light of new IACT projects such as CTA, the design of a flasher with a light monitor is something that might be worth pursuing further, as it could eventually lead to the development of instruments capable of accurately measuring the absolute intensity of the light sent to the camera pixels. An interesting concept that was marginally tested in the course of this project was that of figure 6.26, where the glass plate is eliminated from the design, and instead an SiPM coupled to a scintillator block is directly placed on top of the emitting LEDs. While this design did not ensure an equal sensitivity to every LED, the prototype monitor did show a strong, quasi-linear correlation to the output of the flasher measured by a tradiational R580 PMT (see figures 6.27 and 6.28). To eventually use this concept as a true light monitor, further investigations must be done to model the light propagation process inside the flasher (using Monte Carlo simulations such as GEANT4), better characterize the different noise sources on an SiPM, and include electronic subsystems which would regulate the sensor's temperature and overvoltage.

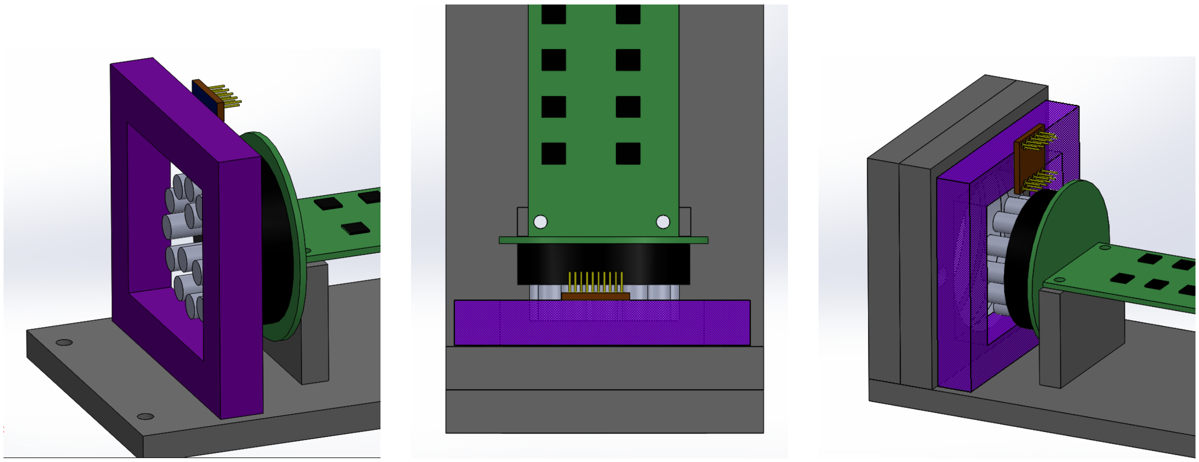

Figure 6.26: Illustrations of the proposed, correlation-based light monitor. The idea of this design is simply to measure the bulk amount of light bouncing off the inside of the flasher casing with a scintillator coupled with an SiPM, and verify if the measurement made inside the flasher are correlated with its output outside the casing. GEANT4 simulations of the flasher's interior could further help in understanding what fraction of the LED light would be measured by this light monitor.

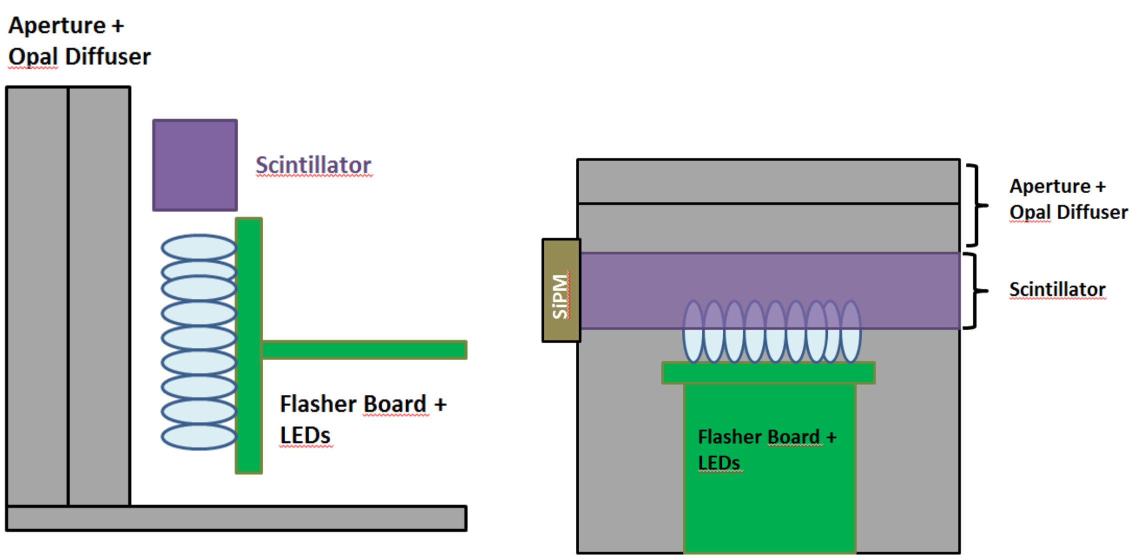

Figure 6.27: Diagram of the experimental set-up used to test the idea of a correlation-based light monitor.

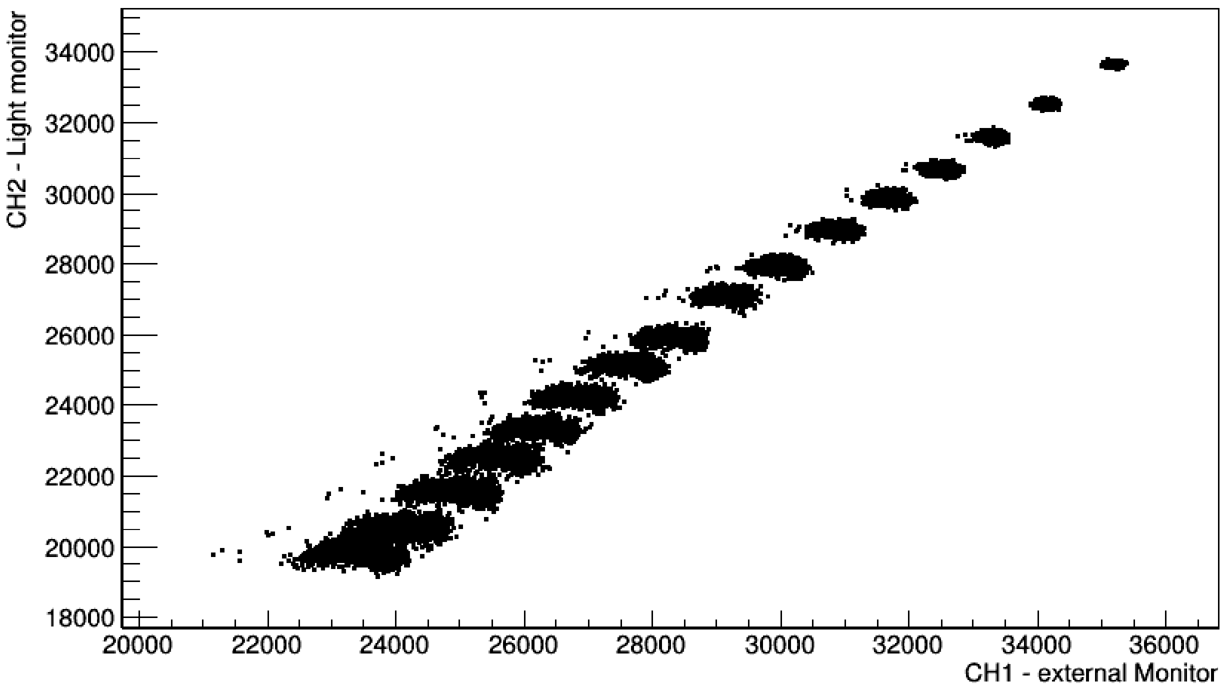

Figure 6.28: Results of the test performed to assess the viability of the correlation-based light monitor. For every event recorded, the integrated charge measured by the control PMT (CH1) and the correlation-based light monitor (CH2) is plotted on this figure. This plot shows that this type of light monitor can produce separated charge histograms, as is possible to see by the horizontal gaps visible along the Y-axis. Additionally, the linearity of this plot shows that the light monitor is well correlated with the external control PMT, which means it could be used to measure a constant fraction of the flasher's light output.

7 Conclusion

This thesis described work made on a new generation of LED flashers which have been installed on the VERITAS telescopes. These flashers play a crucial role in the characterization of the experiment's IRF by sending calibrated light pulses to the cameras of every telescope of the array; these pulses, which linearly increase in intensity according to the number of LEDs that light up during a flasher event, are detected by every pixel of a camera, and digitized in their corresponding FADC channel. The summation of the digitized trace, and the characterization of the moments of their statistical distributions in a given calibration run allows for the measurement of the pixels' absolute gain. By accurately measuring the gains of the IACT's camera pixels, it is possible to correctly estimate the energy of a gamma-ray event by relating the latter to the brightness of its Cherenkov light ellipse on the camera plane.

The objective of the new flasher was two fold. First, it needed to produce a number of light pulses of low intensity that was similar to that of the old flasher, to maintain an accurate characterization of the high-gain mode of the PMT-amplifier chain. Second, the additional number of LEDs included in the new equipment was meant to add brighter pulses to the calibration runs, which would allow the instrument to probe deeper into the low-gain response mode of the VERITAS PMTs.

The initial characterization of the newly manufactured flashers has shown that adjustments needed to be made to reduce the intensity of the pulses produced, as well as their width. A first modification was made to the flashers, by introducing a "two-ramp" concept in which the first four LEDs of the flashers would produce dimmer pulses than the other eleven. While this configuration would have helped the flasher in keeping a few LED pulses in the high-gain mode while probing deeper into the low-gain mode, a difference in the pulse shape produced by the different "ramps" meant that this configuration was unsatisfactory. Instead, a single intensity ramp, with the tuning potentiometers carefully adjusted to calibrate the intensity of the individual LEDs, was preferred.

After tuning the flashers' brightness in the laboratory, they were installed on the VERITAS telescopes, and a preliminary analysis of their performances was made. These results showed that the new instruments produce pulses that are similar in shape as the ones produced by the previous flashers. The current brightness setting of the flashers' LEDs allows for more data points to be included in the photostatistics gain measurements of both the low-gain and high-gain modes of the amplification chain; this additional number of degrees of freedom means that any non-linear behaviour of the PMTs can be tested, by fitting to the data more elaborate gain relationships than equation 15. Finally, while the current brightness configuration does slightly increase the response range probed by the new flasher, it could be improved even further by increasing the light output of the LEDs, at the expense of losing only one or two light levels in the high-gain mode.

In addition to the characterization of a new LED flasher, an experimental set-up was built to test the viability of an independent light monitor concept. This monitor, which would have been integrated inside the new flasher casing, needed to be able to measure a constant albeit small fraction of the flasher's light output, in order to track the LED pulses that get skipped when the FADC is busy reading out a pedestal event. Two light sensor technologies were assessed for this task: PMTs and SiPMs. While the gain of the PMT is more stable than that of an SiPM, the sensitivity of its photocathode (which degrades whenever exposed to bright light), and its cumbersome shape made it difficult to integrate the sensor inside the designed casing, and probably would have required the addition of a shutter to protect the device during daytime. On the other end, the extreme sensitivity of the gain of the SiPM (which has been measure to change by 150% when being cooled down by 10°C) to environmental and operational conditions (namely the operating voltage), will make it difficult to accurately measure the intensity of the light emitted by the flasher. Alternatives should therefore be seeked to track the flasher pulses.

References

[1] Malcom S. Longair. *High Energy Astrophysics.* Cambridge University Press, third edition, 2011.

[2] W.L. Kraushaar, G.W. Clark, G.P. Garmire, R. Borken, P. Higbie, C. Leong, and T. Thorsos. High-energy cosmic gamma-ray observations from the oso-3 satellite. *The Astrophysical Journal*, 177, 1972.

[3] B.N. Swanenburg, K. Bennett, G.F. Bignami, R.Buccheri, P. Caraveo, W. Hermsen, G. Kanbach, G.G. Litchi, J.L Masnou, H.A. Mayer-Hasselwander, J.A. Paul, B. Sacco, L. Scarsi, and R.D. Wills. Second cos b catalog of high-energy gamma-ray sources. *The Astrophysical Journal*, 243, 1981.

[4] D.A. Kniffen. The gamma-ray observatory. *Annals of the New York Academy of Sciences*, 571(1):482–496, 1989.

[5] The Fermi-LAT Collaboration. The large area telescope on the fermi gamma-ray space telescope mission. *Instrumentation and Methods for Astrophysics*, 697, 2009.

[6] The Fermi-GBM Collaboration. The fermi gamma-ray burst monitor. *Instrumentation and Methods for Astrophysics*, 702, 2009.

[7] FERMI-LAT Collaboration. The fermi large area telescope third source catalog. *ApJS*, 2015.

[8] The Whipple 10m collaboration. The whipple observatory 10 m gamma-ray telescope, 1997–2006. *Astroparticle Physics*, 28(2):182 – 195, 2007.

[9] T.C Weekes, M.F Cawley, D.J. Fegan, K.G Gibbs, A.M. Hillas, P.W Kwok, R.C. Lamb, D.A. Lewis, D. Macomb, N.A. Porter, P.T Reynolds, and G. Vacanti. Observation of tev gamma-rays from the crab using the atmospheric cerenkov imaging technique. *The astrophysical Journal*, 342, 1989.

[10] G. Vasileiadis for the H.E.S.S. Collaboration. The h.e.s.s experimental project. *Nuclear Instruments and Methods in Physics Research Section A: Accelerators, Spectrometers, Detectors and Associated Equipment*, 553(1-2):268–273, 2005.

[11] C. Baixeras and the MAGIC collaboration. Commissioning and first tests of the {MAGIC} telescope. *Nuclear Instruments and Methods in Physics Research Section A: Accelerators, Spectrometers, Detectors and Associated Equipment*, 518(1–2):188 – 192, 2004.

[12] T.C. Weekes and the VERITAS collaboration. Veritas: The very energetic radiation imaging telescope array system. *Astroparticle Physics*, 17, 2002.

[13] A.J. Smith for the HAWC Collaboration. Hawc: Design, operation, reconstruction and analysis. *Proceedings of the 34th International Cosmic Ray conference*, 2015.

[14] P. Cogan. *Nanosecond Sampling of Atmospheric Cherenkov Radiation Applied to TeV Gamma-Ray Observations of Blazars with VERITAS*. PhD thesis, UCD Dublin, 2006. PhD thesis.

[15] I.E.Tamm. *Selected Papers*. Springer-Verlag, 1991.

[16] R.A. Bird. *Probing Cosmic Rays with VERITAS: Observations of M31 and the Positron Fraction*. PhD thesis, UCD Dublin, 2015. PhD thesis.

[17] K.Bernlöhr. Air shower cherenkov light simulations.

[18] M. C. Weisskopf. The chandra x-ray optics. *Optical Engineering*, 51(1):011013–011013–8, 2012.

[19] B. Zitzer for the VERITAS collaboration. The veritas upgraded telescope-level trigger systems: Technical details and performance characterization. In *Proceedings of the 33nd International Cosmic Ray Conference*, 2013.

[20] A. McCann. *Discovery of Emission above 100 GeV from The Crab Pulsar With VERITAS*. PhD thesis, McGill University, 2011. PhD thesis.

[21] R. Guenette. *VERITAS observations of galactic compact objects*. PhD thesis, McGill University, 2010. PhD thesis.

[22] A.M. Hillas. Cerenkov light images of eas produced by primary gamma rays and by nuclei. In *Proceedings of the 19th International Cosmic Ray Conference*, 1985.

[23] A. McCann for the VERITAS Collaboration. Detection of the crab pulsar with veritas above 100gev. *Proceedings of the 32nd International Cosmic Ray conference*, 2011.

[24] A. W. Smith for the VERITAS collaboration. Veritas observations of tev binaries. *Proceedings of the 33rd International Cosmic Ray Conference*, 2013.

[25] The HESS Collaboration. Acceleration of petaelectronvolt protons in the galactic center. *Nature*, 531, 2016.

[26] The Fermi-LAT Collaboration. The spectrum and morphology of the fermi bubbles. *The Astrophysical Journal*, 793(1), 2014.

[27] S. Wakely and D. Horan. The tevcat online catalog for tev astronomy, 2016.

[28] R.W. Klebesadel, I.B Strong, and R.A. Olson. Observations of gamma-ray bursts of cosmic origin. *The Astrophysical Journal*, 182, 1973.

[29] F. Halzen and S. R. Klein. Icecube: An instrument for neutrino astronomy. *Review of Scientific Instruments*, 81, 2010.

[30] The LIGO Scientific Collaboration. Advanced ligo. *Classical and Quantum Gravity*, 32(7):074001, 2015.

[31] The VERITAS Collaboration. Veritas search for vhe gamma-ry emission from dwarf spheroidal galaxies. *The Astrophysical Journal*, 720(2), 2010.

[32] S. Archambault. *Search for Very-High-Energy Gamma-Ray Emission from Primordial Black Holes with VERITAS*. PhD thesis, McGill University, 2016. PhD thesis.

[33] S.T. Griffiths. *Exploring the Limits of Lorentz Invariance with VERITAS gamma-ray observations of Markarian 421*. PhD thesis, University of Iowa, 2015. PhD thesis.

[34] HAMATSU PHOTONICS K. K. *Photomultiplier Tubes: Basics and Application*. Hamamatsu, photonics K.K., 3rd edition, 2007.

[35] R. Winston. Light collection within the framework of geometrical optics. *Journal of the Optical Society of America*, 60(2), 1970.

[36] D. Petry. The veritas dc current monitor system, 2002. VERITAS internal document.

[37] D.Hanna. Measuring high-gain and low-gain parameters with the led-based flasher system. Internal VERITAS note, 2013.

[38] F. J. Lombard and F. Martin. Statistics of electron multiplication. *The Review of Scientific Instruments*, 32(2), 1961.

[39] R. F. Tusting, Q. A. Kerns, and H. K. Knudsen. Photomultiplier single-electron statistics. *IRE Transactions on Nuclear Science*, 9, 1962.

[40] W.-Q. Cheng, M. E. Rudd, and Y.-Y. Hsu. Angular energy distributions of electrons from 7.5-150 kev proton collisions with oxygen and carbon dioxide. *Physical Review A*, 40(7), 1989.

[41] S.Fegan. Gain estimation with a light pulser, 2015. CTA internal note.

[42] J.R Prescott. A statistical model for photomultiplier single-electron statistics. *Nuclear Instruments and Methods*, 39, 1966.

[43] B. Bencheikh, R. DeSalvo, W. Hao, C. Xu, and K. You. A simple light detector gain measurement technique. *Nuclear Instruments and Methods*, 315, 1992.

[44] D. Hanna, A. McCann, M. McCutcheon, and L. Nikkinen. An led-based flasher system for veritas. *Nuclear Instrumentation Methods*, A612, 2010.

[45] D.Hanna and A. Gilbert. The optical link to trigger the led-flashers in veritas, 2012. VERITAS internal note.

[46] D. Hanna. The suitability of the led flashers for daily gain monitoring, 2010.

[47] D. Hanna for the VERITAS Collaboration. Calibration techniques for veritas. *Proceedings of the 30th International Cosmic Ray Conference*, 2007.

[48] D. Kieda for the VERITAS Collaboration. Status of the veritas upgrade. *Proceedings of the 32nd International Cosmic Ray Conference*, 2011.

[49] Acqiris Corporation. User manual: Agilent acqiris 8-bit digitizers, 2012.

[50] E. Hecht. *Optics*. Addison-Wesley, 2002.

[51] sensL Corporation. 4-side scalable silicon photomultiplier array, 2013. User Manual.

[52] sensL Corporation. An introduction to the silicon photomultiplier, 2011. Technical note.

[53] A. N. Otte for the CTA Consortium. Development of a sipm camera for a schwarshild-couder cherenkov telescope for the cherenkov telescope array. *Proceedings of the 34th International Cosmic Ray conference*, 2015.

[54] sensL Corporation. B-series: Fast, blue-sensitive silicon photomultiplier sensors, 2013. User Manual.

[55] P K Lightfoot, G J Barker, K Mavrokoridis, Y A Ramachers, and N J C Spooner. Characterisation of a silicon photomultiplier device for applications in liquid argon based neutrino physics and dark matter searches. *Journal of Instrumentation*, 3(10):P10001, 2008.

[56] M. Ramili. Characterization of sipm: temperature dependencies. *IEEE Nuclear Science Symposium Proceedings*, 2008.

[57] L Gallego, J Rosado, F Blanco, and F Arqueros. Modeling crosstalk in silicon photomultipliers. *Journal of Instrumentation*, 8(05):P05010, 2013.

[58] N.W. Ashcroft and N.D. Mermin. *Solid state physics*. Saunders College Publishing, 1976.

A Appendix A: Technical specifications - flasher hardware parts

Table 2: Technical specifications of the Hamamatsu R3998-02 PMT

Parameter Name	**Value (Units)**
Spectral Response	300-650 (nm)
Maximum response wavelength	420 (nm)
Photocathode diameter	25 (mm)
Quantum Efficiency at 370 nm	≈ 0.25
Nominal gain at 1000V	$1.3 \cdot 10^6$
High voltage bias operational range	500-1500 (V)
Number of dynodes	9
Dynode voltage distribution	3:1:1:1:1:1.5:1:1:1:1

[1] The maximum bias is an absolute rating, while the minimum bias quoted defines the range of voltage below which the dynode voltage configuration is not optimized for.

Table 3: Technical specifications of the Hamamatsu R580 PMT

Parameter Name	**Value (Units)**
Spectral Response	300-650 (nm)
Maximum response wavelength	420 (nm)
Photocathode diameter	34 (mm)
Quantum Efficiency at 370 nm	≈ 0.25
Nominal gain at 1000V	$1.1 \cdot 10^6$
High voltage bias operational range	625-1750 (V)
Number of dynodes	10
Dynode voltage distribution	2:1:1:1:1:1:1:1:1:1:1

Table 4: Technical specifications: nichia corporation NSPU510CS UV-LEDs

Parameter Name	**Value (Units)**
Spectral Range	350-400 (nm)
Peak emission wavelength	370-380 (nm)
Emission angle	$40°$
Foward Voltage	3.3 (V)
Nominal radiant flux	15.1 (mW)
radiant flux range	9.6-27.2 (mW)

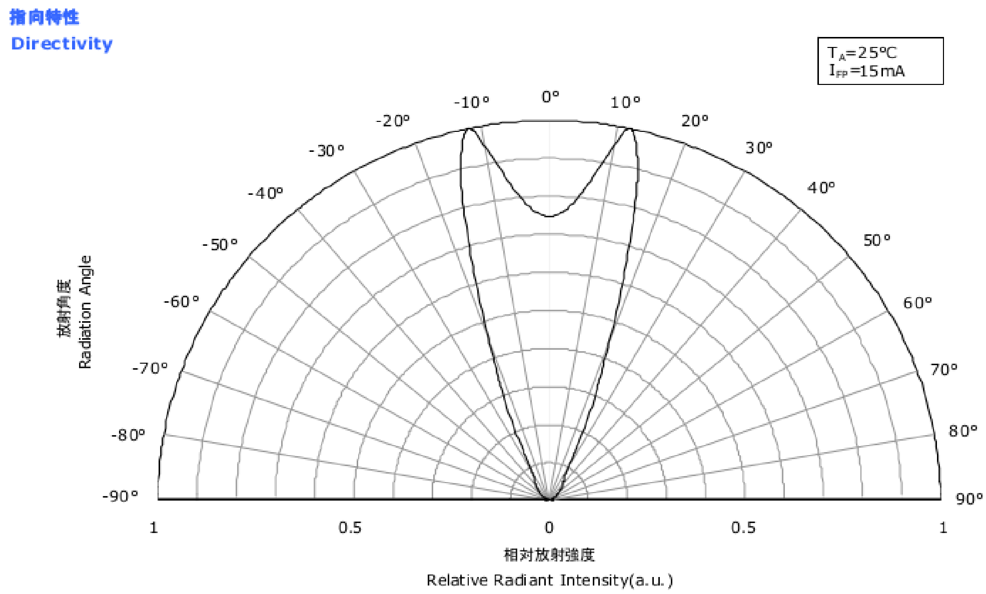

Figure A.1: Emission directivity of the Nichia NSPU510CS UV-LEDs

B Appendix B: Flasher Circuit Diagram

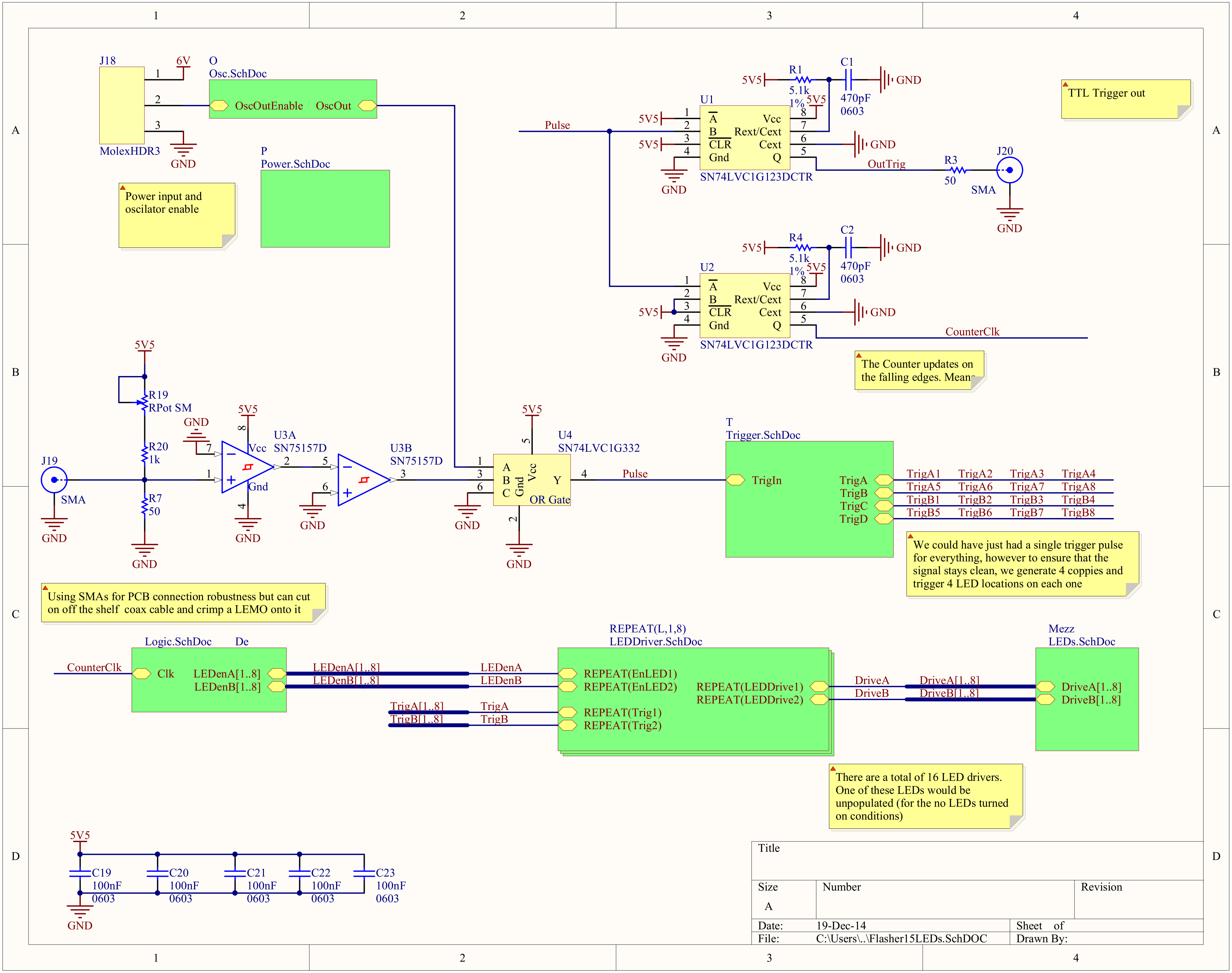
J18
MolexHDR3
6V
GND
O
Osc.SchDoc
OscOutEnable
OscOut
P
Power.SchDoc
Power input and oscilator enable
Pulse
U1
SN74LVC1G123DCTR
A
B
CLR
Gnd
Vcc
Rext/Cext
Cext
Q
5V5
R1
5.1k
1%
C1
470pF
0603
GND
OutTrig
R3
50
J20
SMA
TTL Trigger out
U2
SN74LVC1G123DCTR
R4
5.1k
1%
C2
470pF
0603
CounterClk
The Counter updates on the falling edges. Mean
R19
RPot SM
R20
1k
R7
50
J19
SMA
U3A
SN75157D
U3B
SN75157D
U4
SN74LVC1G332
OR Gate
T
Trigger.SchDoc
TrigIn
TrigA
TrigB
TrigC
TrigD
TrigA1 TrigA2 TrigA3 TrigA4
TrigA5 TrigA6 TrigA7 TrigA8
TrigB1 TrigB2 TrigB3 TrigB4
TrigB5 TrigB6 TrigB7 TrigB8
We could have just had a single trigger pulse for everything, however to ensure that the signal stays clean, we generate 4 coppies and trigger 4 LED locations on each one
Using SMAs for PCB connection robustness but can cut on off the shelf coax cable and crimp a LEMO onto it
Logic.SchDoc
De
Clk
LEDenA[1..8]
LEDenB[1..8]
LEDenA
LEDenB
TrigA[1..8]
TrigB[1..8]
REPEAT(L,1,8)
LEDDriver.SchDoc
REPEAT(EnLED1)
REPEAT(EnLED2)
REPEAT(Trig1)
REPEAT(Trig2)
REPEAT(LEDDrive1)
REPEAT(LEDDrive2)
DriveA
DriveB
DriveA[1..8]
DriveB[1..8]
Mezz
LEDs.SchDoc
There are a total of 16 LED drivers. One of these LEDs would be unpopulated (for the no LEDs turned on conditions)
C19 100nF 0603
C20 100nF 0603
C21 100nF 0603
C22 100nF 0603
C23 100nF 0603
Title
Size
A
Number
Revision
Date: 19-Dec-14
File: C:\Users\..\Flasher15LEDs.SchDOC
Sheet of
Drawn By:

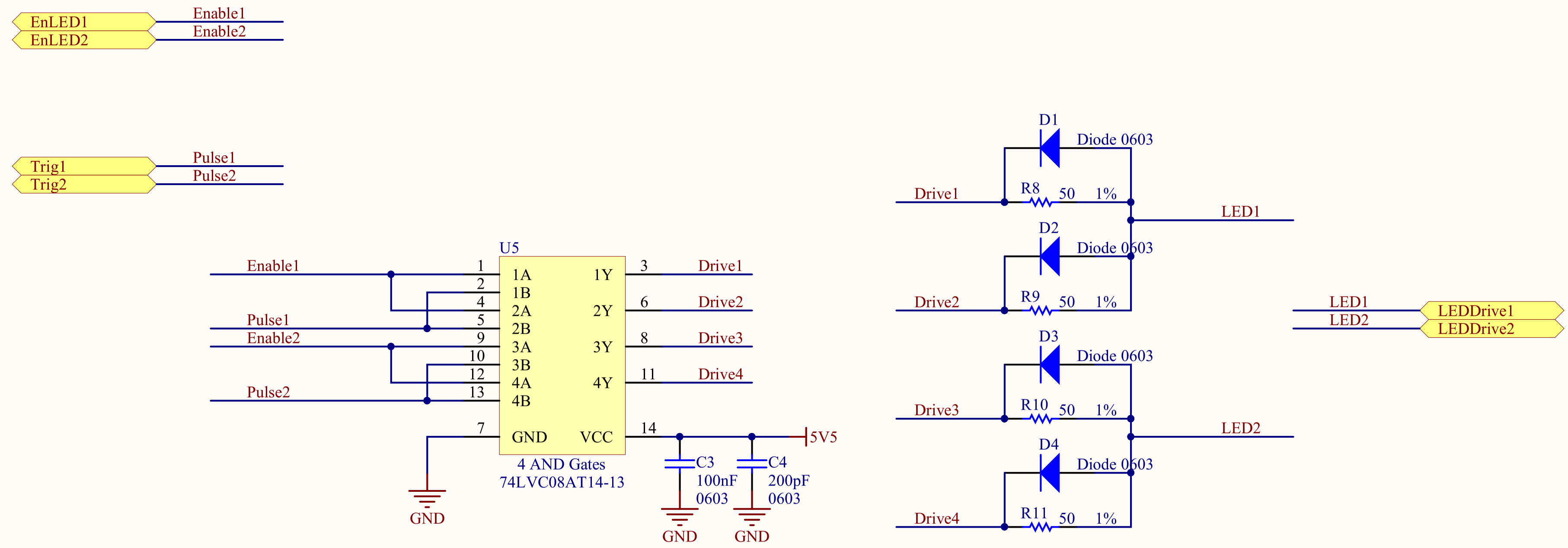

Title		
Size A	Number	Revision
Date: 19-Dec-14		Sheet of
File: C:\Users\..\LEDDriver.SchDoc		Drawn By:

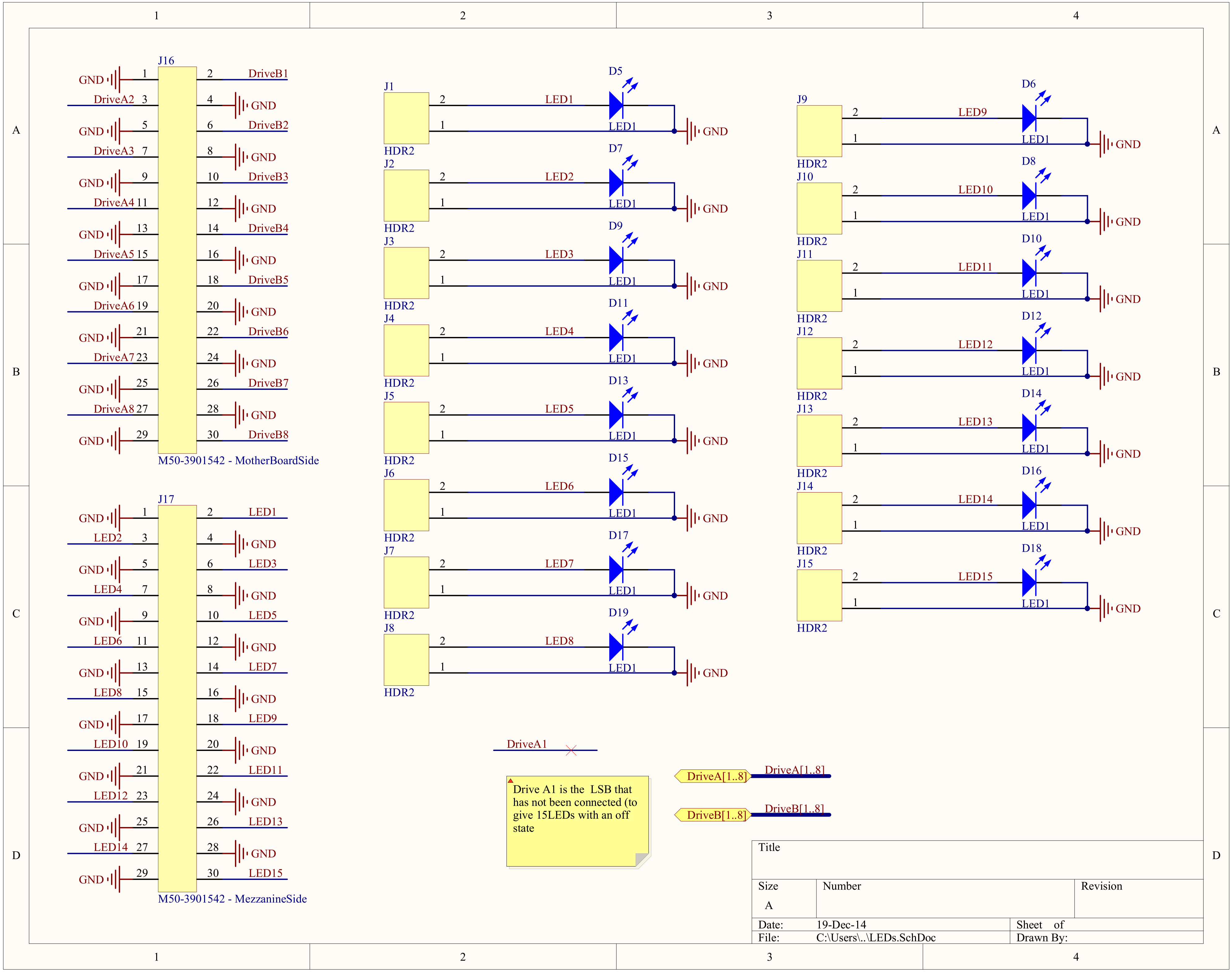
J16
M50-3901542 - MotherBoardSide
GND
DriveA2
DriveA3
DriveA4
DriveA5
DriveA6
DriveA7
DriveA8
DriveB1
DriveB2
DriveB3
DriveB4
DriveB5
DriveB6
DriveB7
DriveB8
J17
M50-3901542 - MezzanineSide
LED1
LED2
LED3
LED4
LED5
LED6
LED7
LED8
LED9
LED10
LED11
LED12
LED13
LED14
LED15
J1 J2 J3 J4 J5 J6 J7 J8 J9 J10 J11 J12 J13 J14 J15
HDR2
D5 D6 D7 D8 D9 D10 D11 D12 D13 D14 D15 D16 D17 D18 D19
LED1
DriveA1
Drive A1 is the LSB that has not been connected (to give 15LEDs with an off state
DriveA[1..8]
DriveB[1..8]
Title
Size
A
Number
Revision
Date: 19-Dec-14
Sheet of
File: C:\Users\..\LEDs.SchDoc
Drawn By:

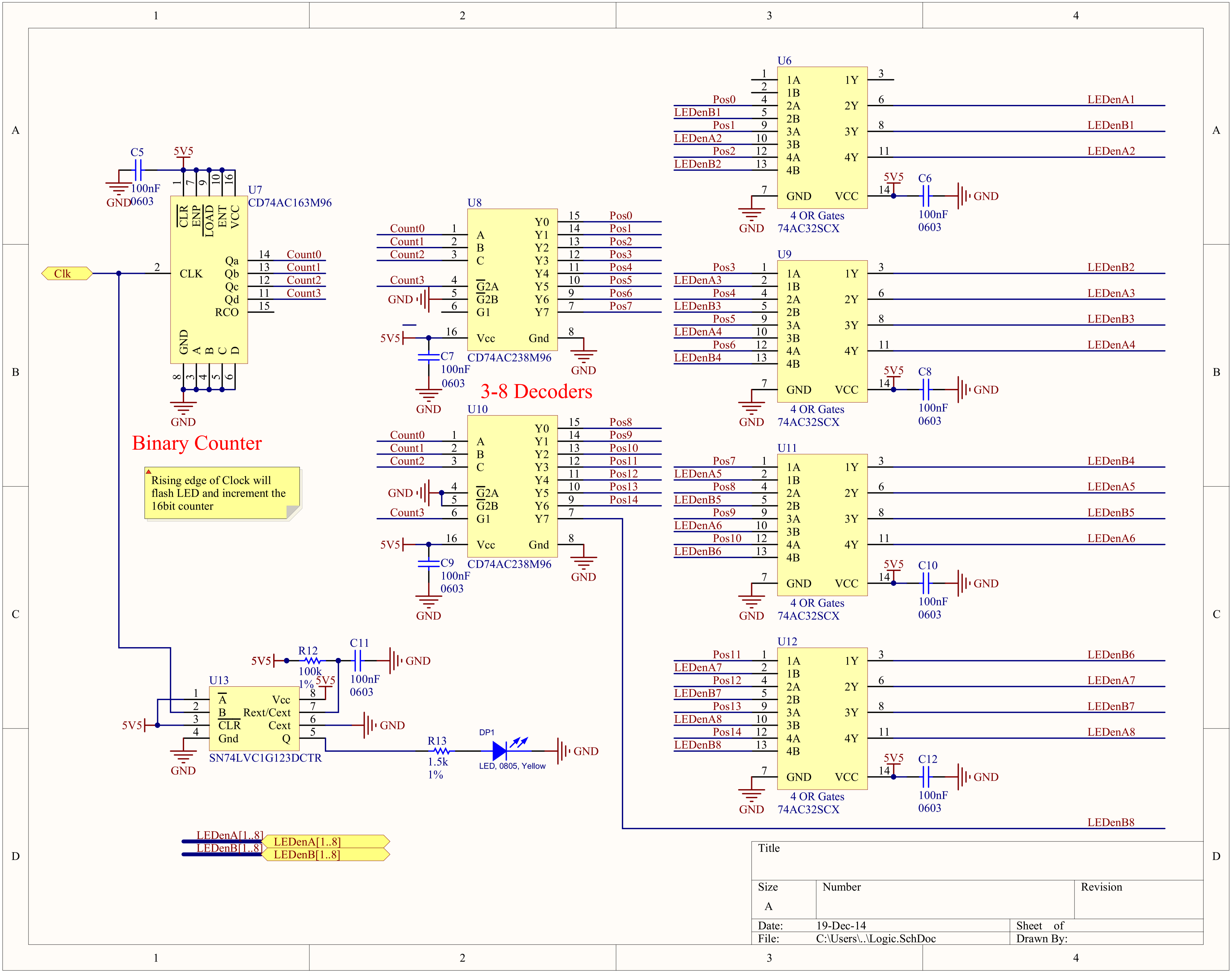
Binary Counter
Rising edge of Clock will flash LED and increment the 16bit counter
3-8 Decoders
Clk
U7
CD74AC163M96
U8
CD74AC238M96
U10
CD74AC238M96
U13
SN74LVC1G123DCTR
U6
U9
U11
U12
4 OR Gates
74AC32SCX
R12
100k
1%
R13
1.5k
1%
DP1
LED, 0805, Yellow
C5
C6
C7
C8
C9
C10
C11
C12
100nF
0603
5V5
GND
LEDenA[1..8]
LEDenB[1..8]
Title
Size
A
Number
Revision
Date: 19-Dec-14
File: C:\Users\..\Logic.SchDoc
Sheet of
Drawn By:

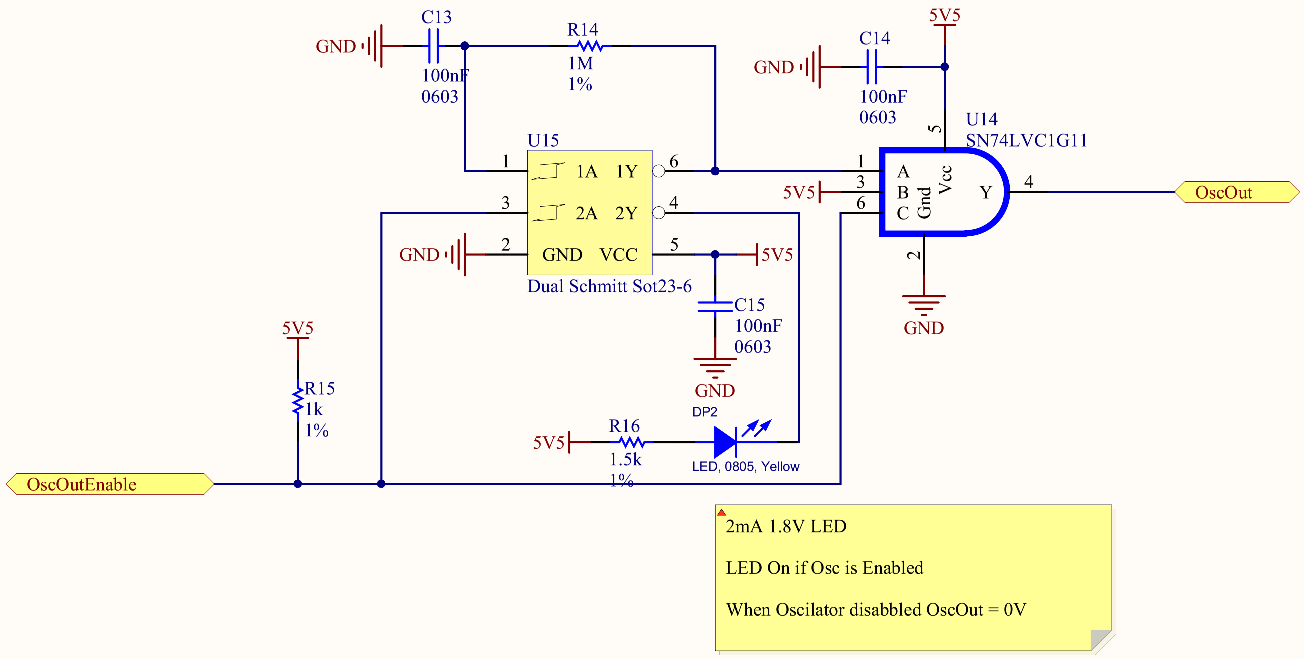

Title		
Size: A	Number	Revision
Date: 19-Dec-14		Sheet of
File: C:\Users\..\Osc.SchDoc		Drawn By:

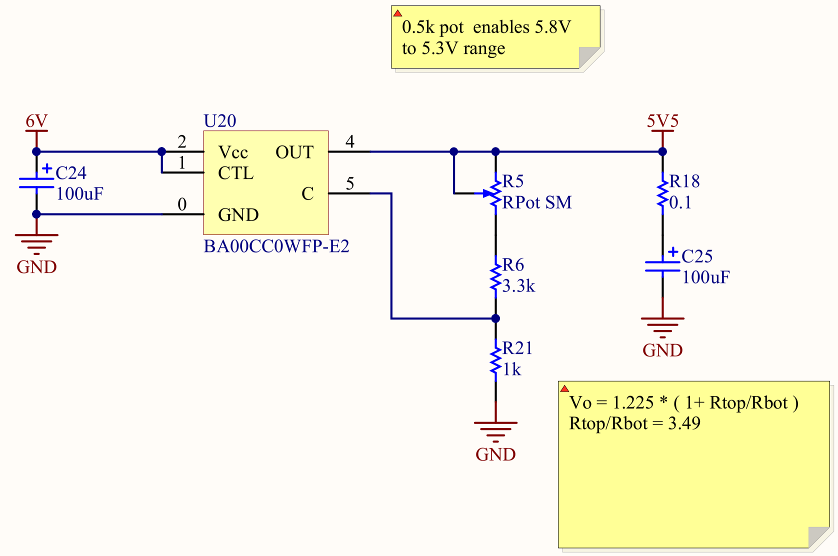

Title			
Size A	Number		Revision
Date:	19-Dec-14	Sheet of	
File:	C:\Users\..\Power.SchDoc	Drawn By:	

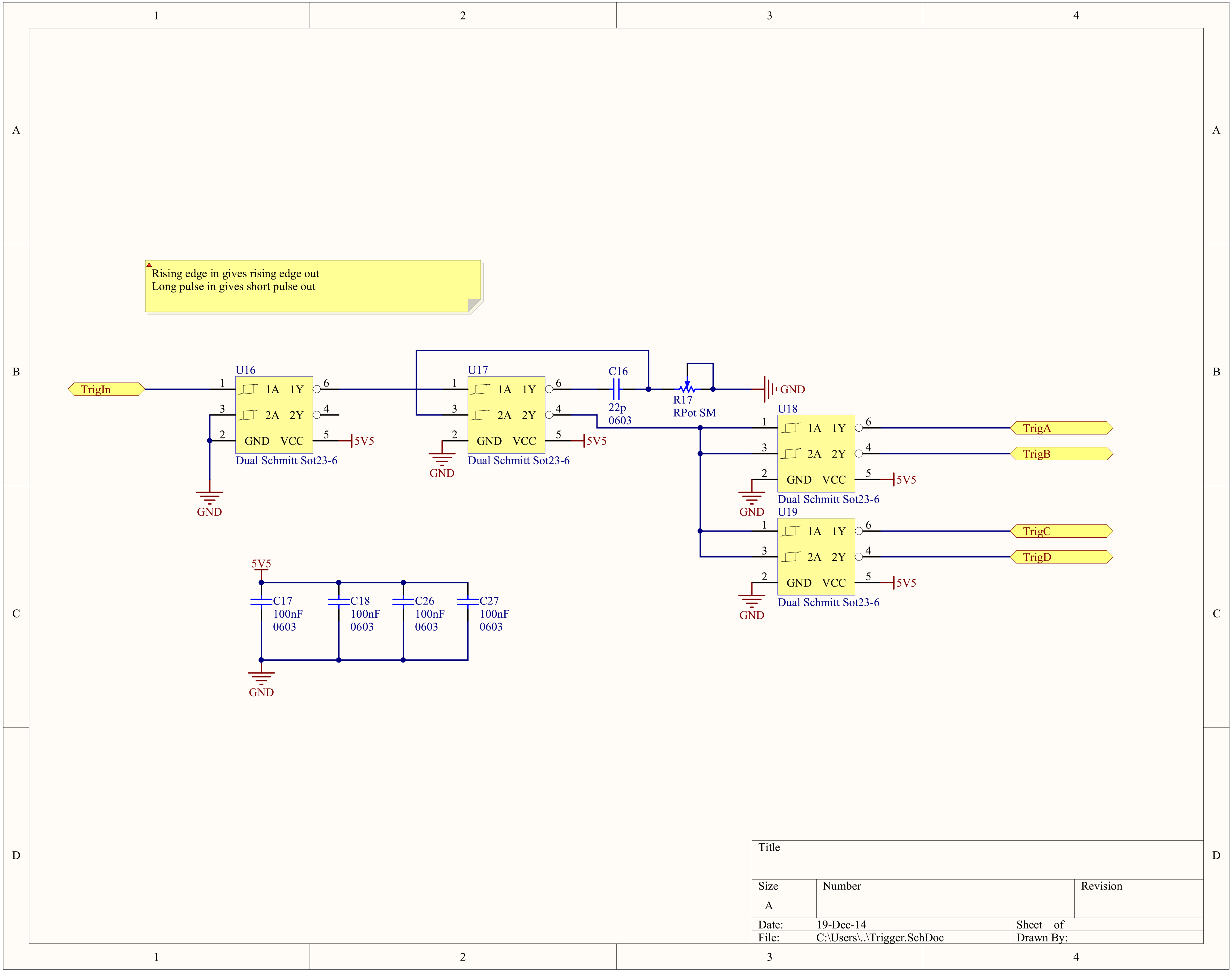

Rising edge in gives rising edge out
Long pulse in gives short pulse out
TrigIn
U16
1A 1Y
2A 2Y
GND VCC
Dual Schmitt Sot23-6
U17
Dual Schmitt Sot23-6
C16
22p
0603
R17
RPot SM
GND
5V5
U18
Dual Schmitt Sot23-6
U19
Dual Schmitt Sot23-6
TrigA
TrigB
TrigC
TrigD
C17
100nF
0603
C18
100nF
0603
C26
100nF
0603
C27
100nF
0603
Title
Size
A
Number
Revision
Date: 19-Dec-14
Sheet of
File: C:\Users\..\Trigger.SchDoc
Drawn By:

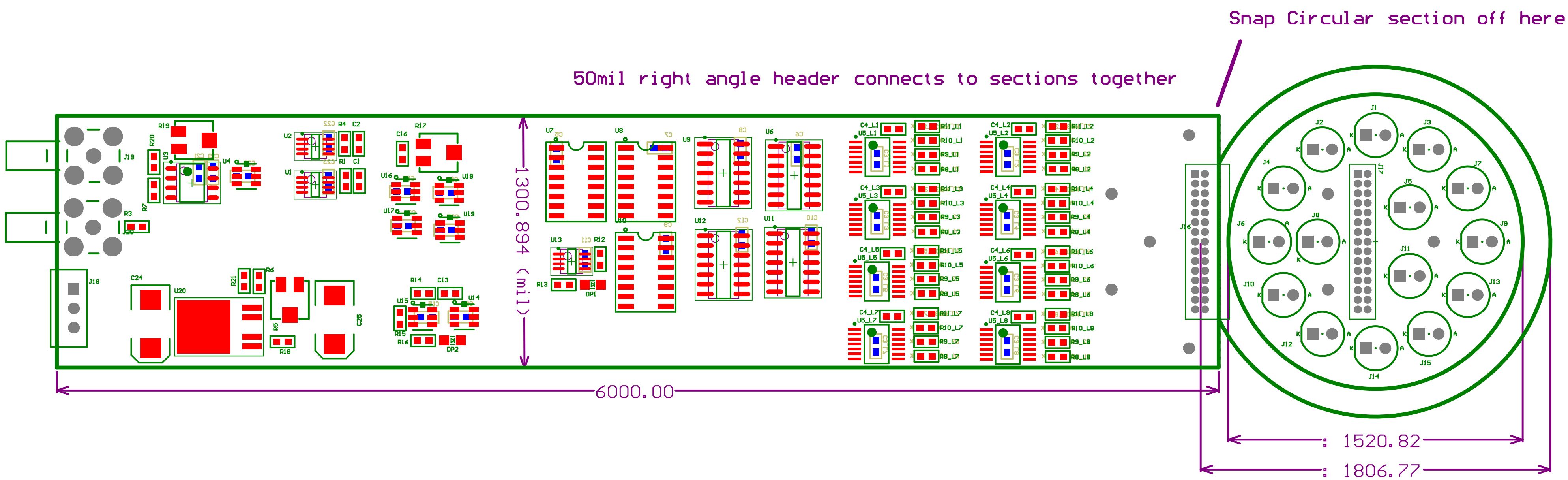
Snap Circular section off here
50mil right angle header connects to sections together
1300.894 (mil)
6000.00
1520.82
1806.77